U.S.NRC
United States Nuclear Regulatory Commission
Protecting People and the Environment

NUREG/CR-7026

Application of Model Abstraction Techniques to Simulate Transport in Soils

Office of Nuclear Regulatory Research

AVAILABILITY OF REFERENCE MATERIALS IN NRC PUBLICATIONS

NRC Reference Material

As of November 1999, you may electronically access NUREG-series publications and other NRC records at NRC's Public Electronic Reading Room at http://www.nrc.gov/reading-rm.html. Publicly released records include, to name a few, NUREG-series publications; *Federal Register* notices; applicant, licensee, and vendor documents and correspondence; NRC correspondence and internal memoranda; bulletins and information notices; inspection and investigative reports; licensee event reports; and Commission papers and their attachments.

NRC publications in the NUREG series, NRC regulations, and *Title 10, Energy*, in the Code of *Federal Regulations* may also be purchased from one of these two sources.

1. The Superintendent of Documents
   U.S. Government Printing Office
   Mail Stop SSOP
   Washington, DC 20402–0001
   Internet: bookstore.gpo.gov
   Telephone: 202-512-1800
   Fax: 202-512-2250
2. The National Technical Information Service
   Springfield, VA 22161–0002
   www.ntis.gov
   1–800–553–6847 or, locally, 703–605–6000

A single copy of each NRC draft report for comment is available free, to the extent of supply, upon written request as follows:

Address: U.S. Nuclear Regulatory Commission
Office of Administration
Publications Branch
Washington, DC 20555-0001
E-mail: DISTRIBUTION.RESOURCE@NRC.GOV
Facsimile: 301–415–2289

Some publications in the NUREG series that are posted at NRC's Web site address http://www.nrc.gov/reading-rm/doc-collections/nuregs are updated periodically and may differ from the last printed version. Although references to material found on a Web site bear the date the material was accessed, the material available on the date cited may subsequently be removed from the site.

Non-NRC Reference Material

Documents available from public and special technical libraries include all open literature items, such as books, journal articles, and transactions, *Federal Register* notices, Federal and State legislation, and congressional reports. Such documents as theses, dissertations, foreign reports and translations, and non-NRC conference proceedings may be purchased from their sponsoring organization.

Copies of industry codes and standards used in a substantive manner in the NRC regulatory process are maintained at—

The NRC Technical Library
Two White Flint North
11545 Rockville Pike
Rockville, MD 20852–2738

These standards are available in the library for reference use by the public. Codes and standards are usually copyrighted and may be purchased from the originating organization or, if they are American National Standards, from—

American National Standards Institute
11 West 42nd Street
New York, NY 10036–8002
www.ansi.org
212–642–4900

Legally binding regulatory requirements are stated only in laws; NRC regulations; licenses, including technical specifications; or orders, not in NUREG-series publications. The views expressed in contractor-prepared publications in this series are not necessarily those of the NRC.

The NUREG series comprises (1) technical and administrative reports and books prepared by the staff (NUREG–XXXX) or agency contractors (NUREG/CR–XXXX), (2) proceedings of conferences (NUREG/CP–XXXX), (3) reports resulting from international agreements (NUREG/IA–XXXX), (4) brochures (NUREG/BR–XXXX), and (5) compilations of legal decisions and orders of the Commission and Atomic and Safety Licensing Boards and of Directors' decisions under Section 2.206 of NRC's regulations (NUREG–0750).

U.S.NRC
United States Nuclear Regulatory Commission
Protecting People and the Environment

NUREG/CR-7026

Application of Model Abstraction Techniques to Simulate Transport in Soils

Manuscript Completed: June 2010
Date Published: March 2011

Prepared by
Y. Pachepsky[1], T. Gish[1], A. Guber[1]
A. Yakirevich[2], M. Kouznetsov[2]
M. Van Genuchten[3],
T. Nicholson[4], R. Cady[4]

[1]United States Department of Agriculture
Agricultural Research Service
Environmental Microbial and Food Safety Laboratory
Hydrology and Remote Sensing Laboratory
Beltsville, MD 20705

[2]Department of Environmental Hydrology & Microbiology
Zuckerberg Institute for Water Research
Blaustein Institutes for Desert Research
Ben-Gurion University of the Negev
Sede Boqer Campus, 84990, Israel

[3]Department of Mechanical Engineering, COPPE/LTTC
Federal University of Rio de Janeiro, UFRJ
Rio de Janeiro, RJ CEP 21945-970, Brazil

[4]U.S. Nuclear Regulatory Commission
Office of Nuclear Regulatory Research
Washington, DC 20555-0001

T.J. Nicholson, NRC Project Manager

NRC Job Code N6235

Office of Nuclear Regulatory Research

ABSTRACT

Successful understanding and modeling of contaminant transport in soils and groundwater is a precondition of risk-informed predictions of the subsurface contaminant transport. Exceedingly complex models of subsurface transport are often inefficient. Model abstraction is a methodology for reducing the complexity of a simulation model while maintaining the validity of the simulation. The objective of this work was to use model abstraction techniques to characterize and understand flow and transport in soils in the presence of shallow groundwater. We developed two case studies by carrying out two types of field tracer experiments at the USDA-ARS OPE3 Beltsville field site, and applying a sequence of model simplifications based on the HYDRUS software family and MODFLOW. Soil moisture, soil water potential, tracer concentrations in groundwater, groundwater levels, and weather data, along with ground penetration radar surveys, electric resistivity monitoring, and dilution tests complemented borehole log data and laboratory hydraulic measurements to characterize soil heterogeneity. The invoked series of model abstractions showed the important role of subsurface heterogeneity in the vadose zone and groundwater, and substantial improved the conceptualization of the subsurface. Results of this study provide techniques to aid the NRC licensing staff in their review of a licensee's abstraction of complex transport models, and to help confirm the acceptability of model abstraction assumptions used in performance assessments.

CONTENTS

ABSTRACT iii
EXECUTIVE SUMMARY xiii
ACKNOWLEDGMENTS xix
ABBREVIATIONS xxi
SYMBOLS xxiii
1 INTRODUCTION 1
2 MODEL ABSTRACTION IN SUBSURFACE HYDROLOGY 3
2.1 Background 3
2.2 Abstraction of model structure 3
2.3 Abstraction of parameter determination 9
2.4 Systematic model abstraction 11
2.4.1 Model abstraction 11
2.4.2 Model abstraction design and example 13
2.5 Model abstraction *vs.* arbitrary selection of a "simple" model. 15
3 EXPERIMENTS TO TEST AND CONFIRM MODEL ABSTRACTION FOR FLOW AND TRANSPORT IN SOILS 17
3.1 Outline of experiments to test and confirm model abstraction in soils ... 17
3.2 OPE3 experimental site at Beltsville Agricultural Research Center 21
3.2.1 General description 21
3.2.2 Existing information relevant to flow and transport in soils 25
3.2.2.1 Small scale structural units and heterogeneities 25
3.2.2.1.1 Soil basic properties 25
3.2.2.1.2 Soil hydraulic properties 25
3.2.2.2 Field scale heterogeneities 28
3.2.2.2.1 Hydrologically active zones and subsurface flow pathways 28
3.2.2.2.2 Soil cover structural units 36
3.2.3 Survey, monitoring and preliminary modeling to design site-specific flow and transport experiments 41
3.2.3.1 Fine-scale ground penetration radar survey 41
3.2.3.2 Location selection and site instrumentation 41
3.2.3.3 Soil basic properties at the lateral flow experimental site 47
3.2.3.4 Soil electrical resistivity survey 52
3.2.3.5 Soil moisture and groundwater monitoring 61
3.2.3.6 Dilution test 67
3.2.3.7 Preliminary coupled surface-subsurface flow modeling 68
3.2.3.8 3D subsurface flow and transport modeling 72
3.2.4 Experimental setups, schedule and results 82
3.2.4.1 Flux measurement experiment 82
3.2.4.2 Lateral flow experiment 89
4 BASE FLOW AND TRANSPORT MODELS 101
4.1 Base model for the flux measurement experiment. 101
4.1.1 Model description 101
4.1.2 Model calibration and simulations 103
4.2 Base model for the lateral flow experiment 114

4.2.1 Model description 114
4.2.1.1 Geometry of the simulation domain and soil material distribution 114
4.2.1.2 Finite element mesh and observation nodes..... 114
4.2.1.3 Initial and boundary conditions..... 118
4.2.2 Model calibration 118
5 MODEL ABSTRACTION APPLICATIONS 135
5.1 Flux measurement experiment. 135
5.1.1 Abstraction by reducing the dimension of the flow domain 135
5.1.2 Abstraction by using an approximate analytical flow model 135
5.2 Lateral flow experiment. 139
5.2.1 Abstraction by ignoring vadose zone 139
5.2.1.1 2D transport in groundwater..... 139
5.2.1.2 1D transport in groundwater..... 146
5.2.2 Abstraction with a change in scale: profile aggregation 151
5.2.3 Abstraction of required parameters: using pedotransfer functions..... 151
5.3 Summary and conclusion. 156
6 REFERENCES 161

APPENDICES
A. REVIEWING THE MODELING PROBLEM CONTEXT. A-1
A1.1 Reviewing the key output A-1
A1.1.1 Key output use A-1
A1.1.2 Key output type and scale A-1
A1.1.3 Accuracy of the key output A-2
A1.1.4 Evaluating model performance A-2
A1.2 Reviewing assumptions made in the base model development and grounds for those assumptions..... A-3
A1.2.1 Subsurface structural units A-3
A1.2.2 Dimension of the problem A-4
A1.2.3 Simulation domain, initial and boundary conditions A-4
A1.2.4 Estimated model parameters A-5
A1.2.5 Data available for calibration A-6
A1.2.6 Calibration procedure and results A-7
A1.2.7 Software properties A-8
A1.2.8 Model documentation A-8
B. FIELD CALIBRATION OF MULTISENSOR CAPACITANCE PROBES. B-1
C. FIELD-SCALE COUPLED SURFACE-SUBSURFACE FLOW MODELING. C-1
C1.1 Equations of the model..... C-1
C1.1.1 Flow model C-1
C1.1.2 Transport model C-2
C1.2 Coupling surface and subsurface flow and transport in the numerical Solution C-2

List of Figures

2-1 Categories of model abstraction techniques relevant to flow and transport modeling in subsurface hydrology 4
2-2 Hierarchy of models to simulate water flow and solute transport in structured soils or in unsaturated fractured rock (Pachepsky et al., 2006)..... 5
2-3 Spatial and temporal operational scales in hydrology (Pachepsky et al., 2006).... 7
2-4 Design of model abstraction via model structure and parameter determination..... 14
3-1 The flux experiment schematic..... 19
3-2 The lateral flow experiment schematic..... 20
3-3 The USDA-ARS OPE3 research watershed; a – aerial view, b – instrumentation. A, B, C, D – research fields..... 22
3-4 Location of groundwater wells soil moisture sensors, and the runoff flume at the Field B..... 23
3-5 Soil basic properties at the field B of the OPE3 watershed. Different colors and symbols refer to different sampling points. Hollow symbols show data for depths larger than 60 cm..... 26
3-6 Figure 3-6. Soil water retention of samples at locations 1 and 2 near well w52 at field B; a) 2-5 cm depth, b) 20-23 cm depth, and c) 47-50 cm depth (●,○ – location 1,▲,▼ - location 2)..... 27
3-7 Probability distributions of the saturated hydraulic conductivity for 20 cm^2 support areas; a – field falling head measurements; ——— - location 1, depth 25 cm , — — —- location 1, depth 45 cm, —·—·— - location 2, depth 25 cm, —··—··— - location 2, depth 40 cm; b – constant head measurements of vertical (●) and horizontal (○) conductivities of undisturbed samples with 20 cm^2 support area in the laboratory (error bars show standard deviations)..... 29
3-8 Water seepage from the wall above the restrictive soil layer enriched with clay.... 30
3-9 Layout of the 7. 5-ha watershed overlaid with the 25- by 25-m sample grid. Blocks with alphanumeric designations and infiltration capacity designations make up the stratified random sample of grid cells selected for soil moisture monitoring probes. The shaded rectangle in the southeast corner of the field site shows the 0.5-ha subsection that was used for soil moisture observation and flow verification (after Gish et al, 2002. Permission to use this copyrighted material is granted by Soil Science Society of America Journal)..... 31
3-10 Ground-penetrating radar image with a digital trace of the first restricting layer shown as the dotted line (after Gish et al, 2002. Permission to use this copyrighted material is granted by Soil Science Society of America Journal)..... 33
3-11 Interpolated depth to the first continuous restricting layer for Block C03. (after Gish et al, 2002. Permission to use this copyrighted material is granted by Soil Science Society of America Journal)..... 34
3-12 Potential subsurface flow pathways (blue lines) identified with Arc/Info hydrologic tools (after Gish et al, 2002. Permission to use this copyrighted material is granted by Soil Science Society of America Journal)..... 35
3-13 Changes in soil water storage in 0-80 cm soil layer during the period of observations..... 37
3-14 Spatial distribution of corn yields in field B in 2001. The red to yellow colors represent low corn yield areas and the dark blue colors represent high corn yield

areas..... 38
3-15 Corn yields and color infrared image of corn biomass taken in August 1999 (in a relatively dry growing season). Green stars designate moisture probe locations, while the red, pink and light blue lines designate subsurface flow pathway locations. The red color indicates regions with high biomass and the white regions low biomass, each reflecting extremes in the vegetative cycle of the corn plant. Corn grain yields greater than the mean are inside the black polygons, whereas areas outside the black polygons denote regions with yields below the mean..... 39
3-16 Spatial corn yield variation from 1998 to 2002. Note that 1998 and 1999 were drought, 2000 was wetter than normal, 2001 was normal, and 2002 was dry..... 40
3-17 Depth to the restrictive layer, subsurface flow pathways (brown polylines), locations of existing multi-sensor capacitance probes (●), groundwater observation wells (●), and runoff flume (⊘) in the vicinity of the lateral flow experimental site at the Field B..... 43
3-18 Lateral flow experimental setup 44
3-19 Schematic of the data acquisition and collection system..... 45
3-20 Multi-sensor capacitance probes and groundwater wells locations at the experimental plot..... 46
3-21 Soil texture measured at 10 depths in 12 locations..... 48
3-22 Measured clay, silt, sand and organic carbon distributions in the soil profiles 49
3-23 Soil bulk density distribution with the depth at locations 1-4..... 50
3-24 Laboratory-measured saturated hydraulic conductivity..... 51
3-25 Laboratory-measured soil water retention..... 53
3-26 The laboratory (left) and field (right) setup to measure soil electrical resistivity.... 54
3-27 Relationship between volumetric soil water content and electrical resistivity measured in samples from 10 depths at 12 locations..... 55
3-28 Performance of the model (602) to simulate the dependence of the soil electric resistivity on soil water content. (a) model parameters do not depend on soil properties, (b) model parameters depend on soil properties..... 57
3-29 Soil temperature distribution in soil profile measured at 7 dates on the ER measurement time. The average temperature from locations 6 and 8 is shown..... 58
3-30 Electrical resistivity measured in 2-m soil profile along 24-m transect. Locations of groundwater wells and MCO (multiple capacitance probes) are shown with arrows..... 59
3-31 Volumetric water content distributions in 2-m soil profile along 24-m transect for 7 dates..... 60
3-32 Monthly (a) and cumulative values (b) of evapotranspiration and precipitation measured at the experimental site during the monitoring period (during July 2006 – September 2007)..... 62
3-33 Soil water content and soil pressure head time series measured during July 2006 – 63
September 2007..... 64
3-34 Relationships between measured in locations 1 through 4 soil pressure head and volumetric water content..... 65
3-35 Groundwater depths measured at the experimental site during the monitoring period (November 2007 – March 2008)..... 66
3-36 Soil surface topography and the finite element mesh in coupled surface-

subsurface flow and transport simulations. The blue rectangle shows the boundaries of the irrigated area..... 69
3-37 Subsurface representation and the finite element mesh in the coupled surface-subsurface flow and transport modeling; a –restricting layer parallel to the daylight surface, b- restricting layer surface from the ground penetrating radar survey. Vertical bars show locations of the observation wells..... 70
3-38 Development of the overland flow in preliminary coupled surface-subsurface simulations..... 73
3-39 Tracer concentrations in the overland flow from the preliminary coupled surface-surface solute transport simulations..... 74
3-40 Simulation domain for solving the flow and transport problem with the HYDRUS-3D model. 76
3-41 Boundary conditions definition..... 77
3-42 Simulated distribution of (a) pressure head, and (b) concentration after 30 days (layer 1.5 m depth)..... 78
3-43 Location of (a) observation nodes and (b) the simulated breakthrough curves..... 79
3-44 Depth to GPR-identified clay lens and location of observation well and moisture capacitance probes (after Gish and Kung, 2007. Permission to use this copyrighted material is granted by Geoderma)..... 83
3-45 Schematic of observation well installation and instrumentation. Schematic is not to scale, i.e., the PVC well is only 3.8 cm in diameter, but 3 m in length (after Gish and Kung, 2007. Permission to use this copyrighted material is granted by Geoderma)..... 84
3-46 Averaged water flow rates pumped from the observation well as a function of time (after Gish and Kung, 2007. Permission to use this copyrighted material is granted by Geoderma)..... 87
3-47 Water table heights in the observation well. Error bars represent one standard deviation (after Gish and Kung, 2007. Permission to use this copyrighted material is granted by Geoderma)..... 88
3-48 Soil water content time series (after Gish and Kung, 2007. Permission to use this copyrighted material is granted by Geoderma)..... 90
3-49 Tracer breakthrough curves for chloride, bromide and PFBA (after Gish and Kung, 2007. Permission to use this copyrighted material is granted by Geoderma)..... 91
3-50 Tracer mass recovery (after Gish and Kung, 2007. Permission to use this copyrighted material is granted by Geoderma)..... 92
3-51 Cumulative water fluxes measured at the experimental site during the Lateral flow experiment..... 94
3-52 Groundwater depths measured at the experimental site during the lateral flow experiment..... 95
3-53 Soil water content measured at 12 locations during the lateral flow experiment.... 97
3-54 Chloride content in the groundwater measured at 12 locations during the lateral flow experiment..... 98
4-1 Simulation domain with the boundary conditions specified (not to scale). Different textures and numbers represent the profile layers. C_T are tracer concentrations in infiltrating water, C_{ir} is the tracer concentration in the irrigation

water..... 102
4-2 Observed (circles) and simulated (lines) soil water contents..... 106
4-3 Observed and simulated breakthrough curves of the tracers: (a) Br, (b) Cl and (c) PFBA. Circles – experimental, solid line – simulated with the seepage face boundary, dashed line - simulated without accounting for the seepage face boundary..... 108
4-4 Cumulative water fluxes to the well. 110
4-5 Cumulative solute fluxes of (a) Br, (b) Cl and (c) PFBA to the well..... 112
4-6 The simulated distribution of (a) pressure head, (b) water velocity vectors, and (c) Br concentration after 3 days the irrigation started..... 113
4-7 Simulation domain for solving the flow and transport problem with the HYDRUS-3D ode: a) whole domain; b) upper sub-layer; c) lower sub-layer..... 115
4-8 Finite element mesh; top –side view, bottom – bird view..... 116
4-9 Locations of the observation nodes..... 117
4-10 Boundary conditions for simulations (refer to text for details)..... 119
4-11 Location of observation wells (blue dots) in the vicinity of simulation domain (red rectangle) and hydraulic head distributions at different times in 2006-2007..... 121
4-12 Simulated (lines) and observed (circles) chloride breakthrough curves. Simulations for the initial set of parameters listed in Table 4-2. L1 through L9 denote observation wells 1-9, ○, ○, and ○ are color codes for L5 through L9 at the depths of 1.65, 1.35 and 1.05 m, respectively; ○ is the color code for the depth of 1.1 m in L1 through L4..... 122
4-13 Simulated (lines) and observed (circles) chloride breakthrough curves. Simulations for the K_s=1. 0, 0.6 and 0.2 m/day for SL, SCL and L, respectively; a_L=0.5 m, a_L/a_T=5. Symbols are the same as in Fig. 4-12..... 126
4-14 Simulated (lines) and observed (circles) chloride breakthrough curves. Simulations for the K_{sat}=1.0, 0.6 and 0.2 m/day for SL, SCL and L, respectively; a_L=0.15 m, a_L/a_T=5. Symbols are the same as in Fig. 4-12..... 127
4-15 Simulated (lines) and observed (circles) chloride breakthrough curves. Simulations for the K_{sat}=1.0, 0.6 and 0.2 m/day for SL, SCL and L, respectively; a) a_L=0.5 m and b) a_L=0.15 m. Symbols are the same as in Fig. 4-12..... 128
4-16 Simulated distributions of the pressure head at the lowest model depth z=0 (corresponds to the altitude of 35 above sea level); DOY is the day of the year..... 129
4-17 Simulated Darcy velocity vectors at the depth of around 1 m below surface; DOY is the day of year..... 130
4-18 Simulated distribution of Cl concentration at the depth of 0.5 m below the surface; DOY is the day of year, pink dots represent location of observation wells..... 131
4-19 Simulated distribution of Cl concentration at the depth of 1 m below the surface; DOY is the day of year, pink dots represent location of observation wells..... 132
4-20 Simulated distribution of Cl concentration at the depth of 1.4 m below the surface; DOY is the day of year, pink dots represent location of observation wells..... 133
5-1 Breakthrough curves of Br observed in the pumping well (open circles) and simulated at the groundwater level with two 1D models; solid line - equilibrium model, dashed line – non-equilibrium model..... 136
5-2 Schematics of unconfined radial flow with infiltration..... 137
5-3 Well capture radius (r^*) and pumping disc (Q_{r0}) as a function of hydraulic

conductivity (K_{sat}) for a given set of parameters (r_0=2. 5 cm, R=3000 cm, a=2000 cm, i=0.41 cm/h, h_0=90 cm, h_R=82 cm)..... 138
5-4 Conversion of the subsurface material distributions from the HYDRIS3D model grid to the MODFLOW model grid. Top left – locations of artificial boreholes with properties defined in HYDRUS3D, top right – material distribution in artificial boreholes, bottom – cross-sections of material distributions in the MODFLOW simulation domain..... 142
5-5 Measured and simulated groundwater levels for the period of soil saturation with water..... 143
5-6 Figure 5-6. Measured (▬) and simulated tracer breakthrough in observation wells with the same values of dispersivity a_L and effective porosity n_e across the simulated transport domain; ▬ a_L=1 cm, n_e=0.2 cm^3cm^{-3}; ▬ a_L =1 cm, n_e=0.3 cm^3cm^{-3}; ▬ a_L =10 cm, n_e=0.2 cm^3cm^{-3}..... 144
5-7 Tracer transport simulations with three subdomains (top) having different parameters for the dispersivity a_L (cm) and effective porosity n_e. Measured (▬) and simulated (▬) Cl breakthrough curves are shown for five different observation wells (bottom). 145
5-8 A conceptual scheme for simulating 1D transport in groundwater during tracer transport experiment..... 147
5-9 Observed (red circles) and fitted (blue lines) breakthrough curves in wells 1 through 12..... 148
5-10 The observed and simulated chloride breakthrough curves for the homogeneous sandy loam profile. Symbols are the same as in Fig. 4-12..... 152
5-11 The observed and simulated chloride breakthrough curves for the homogeneous silt loam profile. Symbols are the same as in Fig. 4-12..... 153
5-12 The observed and simulated chloride breakthrough curves for the homogeneous profiles: a) sandy loam, and b) silt loam. Symbols are the same as in Fig. 4-12..... 154
5-13 The observed and simulated chloride BTCs curves for the abstracted model in which K_{sat} values were determined using pedotransfer functions developed by Rawls et al., (1998). Symbols are the same as in Fig. 4-12..... 155
B-1 Soil water contents measured in the plots (symbols) and calculated using SENTEC (solid lines) and the laboratory measured (dotted lines) multi-sensor capacitance probes calibrations vs. multi-sensor capacitance probes scaled frequency..... B-3
B-2 Plot-averaged vs. multi-sensor capacitance probes estimated soil water contents for the mesic Typic Hapludult soil. Solid symbols and hollow symbols show estimates with SENTEC calibration and the laboratory calibrations developed by Starr and Paltineanu (1997), respectively. Solid and dash trend lines show the general relationship between plot average and MCP-estimated water contents for SENTEC and the laboratory calibrations. The 1:1 line is the dotted one..... B-4
B-3 Average differences between plot-averaged water contents and measured with multi-sensor capacitance probes water contents as a function of texture in the upper 50-cm soil layer expressed with the regression tree. ε is the average deviation for the group, N is the total number of samples in the group..... B-10

List of Tables

3-1	Soil cover of the OPE3 crop production area	24
3-2	Soil properties used in preliminary simulations of coupled surface-subsurface flow and transport	71
3-3	Unsaturated soil hydraulic parameters	80
4-1	Unsaturated soil hydraulic parameters inversely estimated using HYDRUS-1D.	107
4-2	Initial values of unsaturated soil hydraulic parameters	120
4-3	The values of the coefficient determination (R2) and the Modified Index of Agreement (MIA) for two simulation scenarios with a_L=0.5 m and a_L=0.15 m	125
5-1	Calibrated aquifer parameters	149
5-2	Parameters found by solving the inverse of 1D transport in groundwater using CXTFIT.	150
B-1	Soil texture at locations of the multisensor capacitance probes installation	B-5
B-2	Soil bulk density around the multisensor capacitance probes	B-6
B-3	Original and corrected for different depths multi-sensor capacitance probe calibration equations	B-7
B-4	Root-mean-squared differences of plot average water contents (cm^3 cm^{-3}) for the original and corrected multi-sensor capacitance probe calibration equations	B-8

EXECUTIVE SUMMARY

This study was designed and performed to demonstrate the applicability of model abstraction techniques to subsurface flow and contaminant transport problems. The study focused on future applications of modeling to contingency planning and management of potential and actual contaminant release sites within the scope of the US NRC operations. Our main objective was to use modeling along with field and laboratory observations to optimize the characterization of flow and transport processes in the subsurface. A systematic model abstraction methodology was developed and tested in previous work on flow in soils. This study aims to test and confirm the application of model abstraction to pollutant transport processes in soils and shallow groundwater systems.

Two test cases were developed that included field tracer experiments and subsequent modeling with a series of sequentially simplified models. Modeling is generally only one component of subsurface characterization that may, as in this study, also include the use of borehole data, laboratory measurements of the soil hydraulic properties, application of geophysical methods, monitoring of soil moisture and the pressure head, groundwater monitoring, field hydrogeological tests, and tracer studies. The important role of modeling in characterizing the subsurface is to describe the prevailing flow and transport conditions. Given the non-uniqueness of interpretations of geophysical data, the often small scale of borehole and laboratory data as well as of most groundwater samples and tests, and the limitation of soil moisture monitoring in revealing the hydraulic conductivity of soils, development of alternative conceptual subsurface transport models, and distinguishing between these models, should be part of any overall modeling effort.

The OPE3 experimental field site near Beltsville, MD, has been extensively studied for more than 10 years using geophysical, biophysical, remote sensing, and soil and groundwater monitoring methods. Available data are analyzed using a systematic procedure based on a broad vadose zone modeling context developed in this study. A major focus was on the existence of subsurface structural units and features that may drastically change the fate and transport of contaminants in the vadose zone, as well as of projected trajectories of the contaminant plume in groundwater. We found that solute transport in soils and shallow groundwater at the site is potentially affected by such features as the presence of a restrictive fine-textured layer that is not fully continuous laterally, the complex topography of the restrictive layer favoring preferential flow and transport along preferred pathways along its surface relief, the presence of natural capillary barriers, possible funnel flow in a coarse-textural layer between more fine-textured layers, and local high-conductivity parts of the soil pore space.

An extensive field survey and monitoring program had to be initiated as part of this work in spite of the existence of a large database of soil and groundwater properties at the site. The main reason for this was the difference in scale at which the site was characterized previously, and the scale at which flow and transport processes are of a concern in contaminant release applications. Specifically, our 20 x 20 m research site required additional characterization since the site presented only a single pixel in the characterization of the entire 300 x 300 m OPE3 site.

The employed geophysical methods provided essential information about transport-controlling subsurface features. A 2x2 m ground penetrating radar survey showed the existence of a mostly continuous restrictive layer with complex topography. Soil electric resistivity monitoring furthermore revealed the existence of narrow hydrologically active vertical zones. The obtained data indicate that large parts of subsurface soils may not fully participate in the

prevailing flow and transport processes. Biophysical monitoring of the research area allowed delineation of relatively large structural units in the soil cover that provided distinctly different conditions for plant growth. The size of those units exceeded the scale of investigation in this work.

Borehole log data and laboratory hydraulic measurements both confirmed the potential for subsurface preferential solute transport, while at the same time indicating that an exact definition of a representative elementary volume for the subsurface may be difficult, if at all possible. Measurements of the water content and pressure head produced information about the hydraulic properties of the unsaturated soils. Field water retention was well defined using these measurements. This suggests that the Richards model did provide an appropriate conceptualization of the prevailing flow processes at the field site.

Two field experimental studies, both of original design, were carried out and analyzed using model abstraction. One study, referred as the solute flux experiment, was meant to imitate a soil column experiment at the plot scale. The experiment involved the application of a conservative tracer around a well and subsequent irrigation with simultaneous pumping of ground water. This experiment should provide insight into the significance of zones in the soils having a high vertical conductivity. A second study was designed to observe the lateral transport of a surface-applied conservative tracer pulse when transport was controlled by regular irrigation pulses and natural precipitation. This second experiment should demonstrate the effect of the topography and continuity of the restrictive layer, as well as the significance of funnel flow due to the presence of a coarse layer between the finer-textured layers. The vadose zone during both experiments was monitored for soil water content and pressure heads, while groundwater levels and the groundwater chemical composition were also recorded. Groundwater compositions were monitored at three different depths.

Two preliminary modeling projects preceded the lateral transport experiment. One was undertaken to estimate the potential importance of runoff and the need to intercept this runoff. This study required developing a new model and software to simulate coupled surface-subsurface flow and transport at the plot scale for the 30x30 m study area. The software coupled the FEMWATER and 2DSOIL codes, the former simulating subsurface flow and the latter overland flow using a diffusive flow approximation. For the second modeling project we used the new software, HYDRUS-3D, to simulate flow and transport in the three-dimensional subsurface domain at the site. The purpose was to estimate the required duration of the experiment and the frequency of sampling needed to capture in detail the solute breakthrough curves in a number of observation wells. Both preliminary modeling studies were found useful in terms of improving the experiment setup and the schedule of the experiment.

The solute flux experiment comprised approximately 7 days, whereas the lateral flow experiment continued for four months. About 10,000 analyses were made of the tracer concentration in order to develop the breakthrough curves. A preliminary analysis of the experimental results was used to obtain a conceptual representation of the prevailing subsurface transport processes. We hypothesized that preferential transport of solutes occurred in both experiments. Vertical transport in the unsaturated zone seemed to occur much faster than suggested by the observed water fluxes. The tracer breakthroughs in the lateral transport experiment occurred at substantially different times in the wells at similar distances from the application area. The differences in times to some extent corresponded to soil textural differences.

There were no indications in the solute flux experiment results that the Buckingham-Darcy flow model and the corresponding Richards equation were not applicable to the data. Therefore, water flow in both the unsaturated zone and in groundwater was simulated with the Richards equation using the HYDRUS2D software package. The seepage face along the observation well was found to be an important feature of the experimental setup of the solute flux experiment. Transport occurred both in groundwater as well as in the capillary fringe. The Richards equation for flow and the convection-dispersion model for transport were both successfully calibrated and provided good representations of the experimental results. No assumption about preferential solute transport in highly conductive parts of the soil pore space was needed.

The 2D model for flow and transport in the variably-saturated zone was abstracted to a 1D model for vertical water flow and solute transport to groundwater. While ignoring the presence of a seepage face, the 1D model allowed preferential transport of solutes to occur. It appeared that this model was able to provide only approximate qualitative and quantitative predictions of solute breakthrough. The invoked abstraction demonstrated that ignoring the actual geometry of the flow and transport domain and the essential features of the flow process in the field can create a distorted conceptualization of transport in the subsurface.

One more abstraction step was considered for 2D solute transport to demonstrate that a simple analytical model sometimes may be sufficient for certain modeling application. This abstraction was used to investigate the ability of the pumping well to intercept all of the surface-applied tracer, which is a critical aspect of the solute transport experimental setup. For this to occur, the tracer application zone must remain within the groundwater depression cone around the well. We showed that a simple analytical model evaluated the depression cone size with the same degree of accuracy as the more refined 2D saturated-unsaturated flow model.

Results of the lateral flow experiment were relatively more complex than those of the solute flux experiment. Some relatively small temporal scale (1 to 2 day) phenomena were observed in several wells that could not be explained well. We ignored these fine-scale phenomena and concentrated on conceptualizations of the flow and transport processes at larger temporal scales.

The fine-textured low-permeability layer was found to divert the tracer according to the topography of the layer. There were no indications that the Buckingham-Darcy flow model and corresponding Richards equations were inapplicable at the larger scale, likely because flow and transport at that scale seemed to be driven mostly by the hydraulic gradients in groundwater. The complexity of the flow and transport domain required the use of a full 3D representation. For this reason we used the HYDRUS3D software to simulate flow and transport in the lateral flow experiment.

No attempt as yet has been made to calibrate the 3D flow/transport model assuming a layered profile. Since HYDRUS3D does not have a calibration option, only trial and error calibration could be applied. Given that 2 days of computation were needed for each simulation run with this code, we streamlined the calibration procedure by calibrating the model directly to the breakthrough curves, and not to groundwater levels. This created a dilemma in terms of selecting an appropriate conceptual model for transport. Solutes could be delivered to a well via two different transport mechanisms: (a) transport via a network of well-connected pathways that comprise only part of the bulk soil porosity at the field scale, thus assuming that part of the domain does not participate in the transport process, or (b) transport through all of the domain. To deliver solute to a well at approximately the same time, average water fluxes should be smaller in case (a) as compared to the case (b). We selected case (b) and used several model abstractions to justify this selection.

The trial-and-error calibration based on zonation of the flow and transport domain was reasonably successful. The maximum concentration levels and the 50% concentration arrival times were described satisfactory. However, we could not accurately reproduce the shape of the breakthrough curves.

A dimension reduction abstraction considered only 2D flow in groundwater. MODFLOW and MT3D were used for this purpose. A special effort was undertaken to use in this abstraction the same zonation and layering as in the complete 3D representation. MODFLOW calibration capabilities were used successfully to reproduce the groundwater levels, while dispersivity and effective porosity values were estimated by trial and error from the breakthrough curves. The 2D abstraction process showed that the assumption of part of the soil not significantly participating in the solute transport process created a better representation of the breakthrough curves. A reasonable representation of solute transport was achieved with an effective porosity of 60-70% of total soil porosity. Thus, the model abstraction step helped to substantially improve the conceptualizaton of the subsurface transport conditions.

A 1D abstraction step allowed efficient assessment of intrinsic groundwater velocities and the hydrodynamic dispersion parameters in different directions. The results also suggested the location of preferential flow pathways. Using pedotransfer functions to estimate saturated hydraulic conductivities and/or to substitute the heterogeneous soil profile by an equivalent homogeneous medium indicated that this kind of model abstraction may lead to incorrect estimates of tracer front arrival times at some locations. Actually, results depended on the complexity of the heterogeneity being abstracted. Since small-scale heterogeneities may control flow and transport at the larger scale, a careful profile aggregation and analysis of the results is required.

The data analyses in this study permit several observations. First, our detailed studies revealed considerable soil heterogeneity at a very small site. We do not know how common such a degree of heterogeneity is since studies at this level of detail are relatively rare. It is important to recognize that the scale of our experiment was comparable the scale of solute release. Exclusion of a substantial part of the soil from the active solute transport process appears to be an important consequence of soil heterogeneity at the field scale.

Second, calibration of vadose zone models is much more trying than calibration of groundwater models. This because of nonlinearity of the governing flow processes and the large number of parameters involved. Substantial changes in soil water contents and flow rates must occur to reliably calibrate a vadose zone model.

Third, the use of models that assume the presence of mobile and immobile zones was avoided in this work. Such models are undoubtedly important when breakthrough tails are of interest. However, measuring tails takes time that is often impractical for field scale tracer studies where transport is controlled by weather conditions rather than by regional groundwater flow rates. And even when the tail is known, severe correlations are usually observed between the many parameters needed in this type of modeling. Assuming an effective porosity allowed us to characterize the subsurface so as to obtain the correct arrival times, and to obtain a reasonable approximation of the concentration maximum and the center of the mass position.

Fourth, results of this study have implications for solute monitoring transport in heterogeneous formations. Well data generally represent a fairly small scale. In our experiments we encountered distinctly different breakthrough curves in wells that were approximately in similar positions relative to the source along the tracer plume propagation direction. A more

general representation of solute transport in terms of integrated properties may be needed in order to provide a more reliable and accurate representation with models.

Overall, this study demonstrated the usefulness of model abstraction in simulations of flow and transport in a variably-saturated subsurface. Whereas multidimensional and multi-process representations leaves room for several competing conceptual models for flow and transport, simpler models that retain the most essential features of those representations could provide meaningful alternatives.

ACKNOWLEDGMENTS

This work was partially supported via Interagency Agreement RES-02-008 between the U. S. Nuclear Regulatory Commission and USDA Agricultural Research Service.

The authors acknowledge with thanks contributions by the following individuals:

Dr. Robert Hill and Mr. Zane Hadzick of the University of Maryland for their work in the electric resistivity survey, Mr. Randy Rowland and Mrs. Lynn McKee of USDA-ARS-Beltsville for their exceptional support of field and laboratory work; Dr. Daniel Gimenez and Dr. Dennis Timlin for their thoughtful comments of a draft version of this manuscript.

Abbreviations

1D, 2D, 3D	One-dimensional, Two-dimensional, Three-dimensional
2DSOIL	Modular simulator of soil and root processes
ANN	Artificial neural networks
BTC	Breakthrough curves
C	Clay
CV	Coefficient of variation
DGPS	Differential global positioning system
EM	Electromagnetic induction
ET	Evapotranspiration
FAO	Food and Agriculture Organization of the United Nations
FEMWATER	Finite element model for groundwater
GMS	Groundwater Modeling System
GWD	Groundwater depth
HPLC	High performance liquid chromatography
HYDRUS	Software package for simulating the movement of water, heat and multiple solutes in variably-saturated media.
IC	Ion chromatography
L	Loam
MA	Model Abstraction
MCP	Multi-sensor capacitance probes
MODFLOW	Three-dimensional finite-difference ground-water flow model
MT3D	Modular 3-D Solute Transport model
MWBUS	Model of Water Budget of Unsaturated Soil
NRC	U. S. Nuclear Regulatory Commission
OPE3	Optimizing Production Inputs for Economic and Environmental Enhancement
PEST	A nonlinear Parameter Estimation and optimization package
PFBA	Perfluorobutyric acid
PTF	Pedotransfer function
PVC	Polyvinyl Chloride
RES2DINV	Software designed to interpolate and interpret field data of electrical geophysical prospecting (2D sounding) of electrical resistivity (conductivity) and induced polarization.
REV	Representative elementary volume
ROSETTA	Windows-based program that implements artificial neural network to soil hydraulic parameters
SCL	Sandy Clay Loam
SiltCL	Silt Clay Loam
SiltL	Silt Loam
SL	Sandy Loam
STANMOD	STudio of ANalytical MODels software designed for evaluating solute transport in porous media using analytical solutions
SURFER	Environmental software designed to produce contouring maps and surface plots in 2D
TDR	Time Domain Reflectometry

SYMBOLS

Roman symbols

A	cross-sectional area of the well
a	empirical parameter
a_L	longitudinal dispersivity
a_T	longitudinal dispersivity
B	empirical parameter
BD	soil bulk density
C	solution concentration
c_0	initial concentration
c_b	background concentration in the groundwater
Clay	percent clay
c_R	concentration of water in rain
c_{sorb}	surface density of the attached solute
c_w	concentration in the well
$C_w^{obs}(t_i)$	observed concentrations of a tracer in pumped water
$\overline{C_w^{obs}}$	mean observed concentration
$C_w(t_i)$	simulated concentrations of a tracer in pumped water
$\mathbf{D}$	hydrodynamic dispersion tensor
$\overline{\overline{D}}$	surface diffusion-dispersion tensor
d_m	molecular diffusive component
D_{soil}	solute dispersion coefficient in soil
d_w	well diameter
ER	electrical resistivity
ER_{ref}	reference electrical resistivity
g	the acceleration due to gravity
h	flow depth on soil surface
$H(r)$	the Heaviside step function
h_0	water table height at $r=r_0$
h_R	water table height at $r=R$
i	recharge rate
J	rate of solute loss from runoff to soil with infiltration
$\mathbf{K}$	hydraulic conductivity tensor
$\ddot{k}$	corrected hydraulic conductivity in surface boundary nodes
K_F	parameters of the Freundlich equation for the mass-exchange isotherm
K_{sat}	saturated hydraulic conductivity
k_{surf}	surface conductivity
$k_{z_{1/2}}$	conductivity between two nodes
m	a parameter of van Genuchten's water retention model
m	Manning roughness coefficient
M	rate of the solute mass influx from rain
MIA	modified index of agreement

n	a parameter of van Genuchten's water retention model
nF	parameters of the Freundlich equation for the mass-exchange isotherm
p	pressure head
$\mathbf{q}$	Darcy-Buckingham flux vector
q	tracer dilution rate
$\ddot{q}^{I+1}$	corrected flux at surface boundary nodes in x or y directions
Q	radial water flux to well
$Q_{c(SF)}$	mass fluxes of the tracers to the well trough the seepage face
$Q_{c(VB)}$	variable flux boundaries
q_d	apparent flow rate caused by molecular diffusion of the solute
q_f	velocity of the undisturbed ground water flow
q_h	apparent flow rate caused by density convection
q_m	apparent flow rate caused by the mixing device
q_s	apparent flow rate caused by vertical currents in the well screen
q_z	water flux in the vertical direction
r	radial coordinate
R	rainfall rate
R	radii of the outer boundary
r_0	radii of the well
RMSD	root-mean-square difference
S_0	surface slope in x-direction
Sand	percent sand
S_e	soil water saturation
SF	multi-sensor capacitance probe scaled frequency
Silt	percent silt
T	temperature
t	time
T_{ref}	reference temperature
u	velocity components in x-direction
v	velocity components in y-direction
V	water-filled well volume
z	gravitational head
z_s	land surface elevation

Greek symbols

α	dispersivity tensor
α	a parameter of van Genuchten's water retention model
Δz	distance between two nodes
$\eta(h)$	Heaviside function
θ	volumetric water content
θ_{max}	maximum volumetric water content
θ_{min}	minimum volumetric water content
θ_r	residual water content
θ_s	saturated water content

$\ddot{\theta}^{l}$	corrected water content of surface boundary nodes
λ	decay or biodegradation rate coefficient
τ	parameter of Genuchten-Mualem model
ω	spread parameter in a step function approximation

1 INTRODUCTION

U.S. NRC staff reviews of performance assessments of nuclear facilities (e.g., decommissioning of the facilities, management of low-level and high-level radioactive waste disposal sites) frequently involve assessing models for subsurface water flow and solute transport in the vicinity of a nuclear facility (U. S. NRC, 1993, 1994). These models seek to represent complex and highly transient subsurface systems. Representations of those complex systems in existing models ranges from very simple to extremely sophisticated formulations (Davis et al., 2004; Meyer et al., 1997; Neuman and Wierenga, 2003; Reily and Harbaugh, 2004; Hill and Tiedemen, 2007).

Soluble contaminants are typically expected to be released into a variably-saturated subsurface (or vadose) zone, which may include soils and fractured rocks. The vadose zone is made up of soils in many or most practically important cases. Soil properties of the vadose zone control contaminant travel times to groundwater, the actual locations where contaminant will reach groundwater, and the chemical, and biological transformations that contaminants are subjected to while moving through soils. A successful understanding and modeling of contaminant transport in soils is hence a precondition of risk-informed predictions of subsurface contaminant transport.

Many mathematical models of subsurface flow and transport may be formulated for the same site. One reason for this is the inherent complexity of vadose zone layering and the properties of soil layers, lenses and other structural units that are generally resent. This complexity needs to be grossly simplified to be expressed in mathematical terms, with different sets of simplifying assumptions leading to different models (Neuman and Wierenga, 2003). And even when the kinds and relative positions of the structural units are selected, knowledge is never certain about the locations of the boundaries of these units, and about the flow and transport properties of the soils making up those units. This creates substantial uncertainty in the parameters of the models.

The existence of several candidate models for the same observation site or for the same phenomenon is common in the environmental sciences and their applications, as well as in other disciplines. Making use of several models has been shown to be more beneficial than looking for the "single best" model. One approach, called multimodeling, uses outputs from several models, and assigns weights to those outputs to obtain the best fit to data. Multimodeling has been widely used in atmospheric sciences (Barnston et al., 2003; Palmer et al., 2000, 2004), and is now increasingly accepted also in groundwater modeling (Ye et al., 2004; Poeter and Anderson; 2005) as well as vadose zone flow modeling (Guber et al., 2006, 2008). The use of simpler modes to complement a complex model is another approach to utilize the multiplicity of models (Bigelow and Davies, 2003; Van Ness and Scheffer, 2005). Simple models have advantages regarding the collection of data, the computations involved, the interpretation of the simulation results, and conveying the simulation approach to both technical and lay audiences. On the other hand, the explicit description of mechanisms in more complex models may cause their better performance outside of conditions for which the simple models have been developed and tested.

Currently, different research fields have been using different approaches to the selection or derivation of simple models for use along with more complex models. One of the methods consists in a systematic derivation of simpler models from the original complex model. This method has been termed "model abstraction". In subsurface hydrology, this systematic model simplification was first suggested by Neuman and Wierenga (2004) in their work for the U. S.

Nuclear Regulatory Commission. Examples of useful simplifications of ground water models were presented by Hill (2006). For soils, the model abstraction methodology, including techniques and examples of using model abstraction to simulate water flow, was developed in a recent interagency study by Pachepsky et al. (2006). We viewed the application of model abstraction to solute transport in soils as the next logical step.

The objective of this work was to develop a test example of the application of model abstraction to solute transport in a field soil. The work was designed to be an intensive study that should include a variety of advanced methods for characterizing, monitoring, and modeling flow and transport processes in the vadose zone. We benefitted in this study greatly from using the USDA-ARS OPE3 research site in Beltsville, MD, where the subsurface hydrologic and solute transport processes have been studied for more than a decade before this particular study began.

2 MODEL ABSTRACTION IN SUBSURFACE HYDROLOGY

2.1 BACKGROUND

Model abstraction is a methodology for reducing the complexity of a simulation model while maintaining the validity of the simulation. Model abstraction techniques stem from a need to improve the reliability and to reduce the uncertainty of simulations, to make modeling and its results more explicable and transparent to end users, and to enable more efficient use of available resources in data collection and computations.

An important feature of model abstraction is the explicit treatment of model structure uncertainty. Model structure, along with data uncertainty and scenario uncertainty, is known to introduce uncertainty in the modeling results. Unlike uncertainty in input data, model parameters and scenarios, the effect of model structure uncertainty on the uncertainty in simulation results is usually impossible to quantify in statistical terms. Using model abstraction, a series of models with feasible structures can be built and evaluated in a systematic manner. Each of the models is evaluated from results of an ensemble of simulations by its accuracy to measurement data, and by its predictions with respect to scenarios that have not been observed.

Earlier collaborative work of ARS and NRC staff resulted in the definition of several categories of model abstraction techniques relevant to subsurface flow and transport modeling (Pachepsky et al., 2006). These categories included abstractions of model structure and model parameter determination, and were based on a comprehensive review of model simplification techniques developed for subsurface flow and transport (Fig. 2-1). A brief review of available model abstraction techniques is given below for clarity and reference purposes; more detailed descriptions are in the above cited NUREG report.

2.2 ABSTRACTIONS OF MODEL STRUCTURE

Hierarchies of models. An example of the hierarchy of models available to simulate water flow in variably-saturated porous subsurface media is presented in Fig. 2-2. A pre-defined hierarchy of models has been suggested previously for flow and transport in structured media (Altman et al., 1996). Fig. 2-2 shows a schematic representation of increasingly complex models that may be used to simulate preferential flow and transport in macroporous soils or unsaturated fractured rock. The simplest water budget model describes the accumulation of water in the soil matrix and its discharge when the water content exceeds the field water capacity, or during evaporation periods (Fig. 2-2a). The classical approach of simulating flow/ transport processes in a vadose zone devoid of macropores or fractures is to use the Richards equation for variably-saturated water flow and the advection-dispersion equation for solute transport (Fig. 2-2b). The simplest situation (Fig. 2-2c) for a fractured medium arises when the Richards and advection-dispersion equations are still used in an equivalent continuum approach, but now with composite (double-hump type) hydraulic conductivity (permeability) curves of the type shown by Mohanty et al. (1997), rather than the classical smooth curve for the relative permeability shown in Fig. 2b. More involved dual-porosity type models (Fig. 2-2d) result when the medium is partitioned into fracture and matrix pore regions, with water and/or solutes allowed to exchange between the two liquid regions (e.g., Ventrella et al., 2000). Different formulations of this type are possible. For example, one could permit transient variably-saturated flow in the fractures only, while allowing water to exchange between the fracture and matrix domains. The latter situation leads to both advective and diffusive exchange of solutes between the fractures and the matrix but still

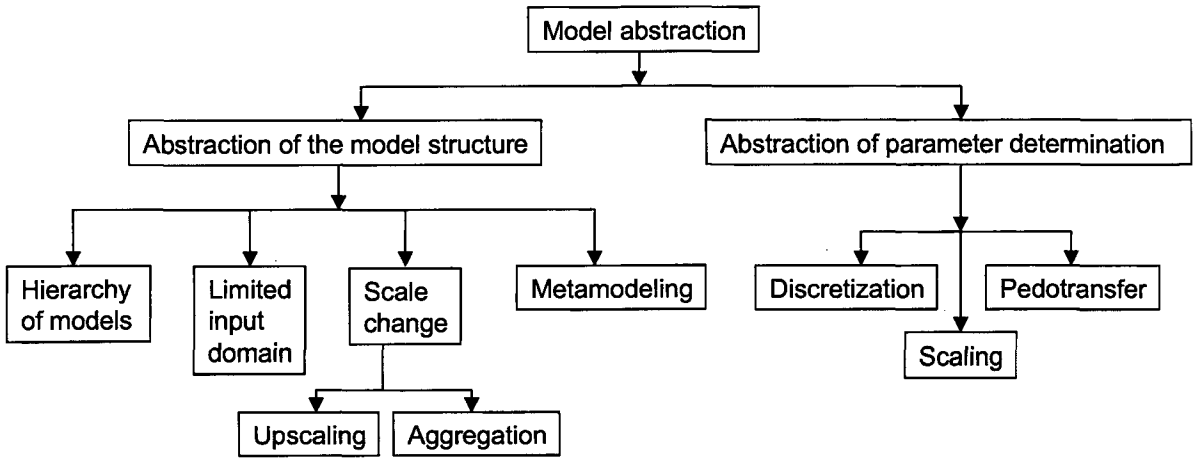

Figure 2-1. Categories of model abstraction techniques relevant to flow and transport modeling in subsurface hydrology.

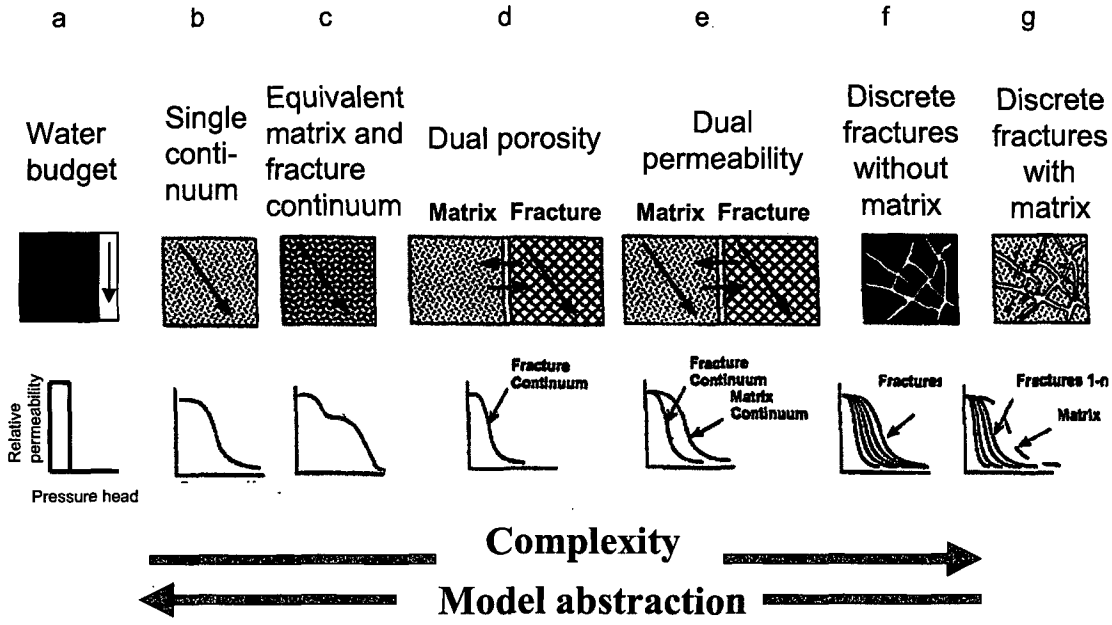

Figure 2-2. Hierarchy of models to simulate water flow and solute transport in structured soils or in unsaturated fractured rock (Pachepsky et al., 2006).

without vertical flow in the matrix (e.g., Zurmühl and Durner, 1996; Zurmühl, 1998). Dual-permeability models (Fig. 2-2e) arise when water flow occurs in both the fracture and the matrix domains. Examples are models by Pruess (1991), Gerke and van Genuchten (1993) and Jarvis (1999). These models use different formulations for the exchange of water between the fracture and matrix regions. In some models (e.g., Wilson et al., 1998) more than two domains are considered, each one having its own hydraulic properties. The modeling approach can be refined further by considering transient flow and/or transport in well-defined discrete fractures without (Fig. 2-2f) or with (Fig. 2-2g) interactions between the fractures and matrix. The latter approach is based on the assumption that the flow and transport equations of the fracture network can be solved in a fully coupled fashion with the corresponding equations for the matrix (e. g., Therrien and Sudicky, 1996).

Limited input domain. Model abstraction techniques based on delimiting the input domain rely on the notion that some feature or process may not be relevant for a given class of scenarios or for a given set of model outputs. A reduction in the spatial dimensionality is one application of this technique. Two-dimensional representations of the subsurface are sometimes redundant and 1D representation may suffice as shown by Wang et al. (2003). In another example, Guswa and Freyberg (2002) explored the possibility of using a 1D model to characterize solute spreading in a medium containing low-permeability lenses; they found that the 1D macroscopic advection-dispersion equation matched results of the 2D model well when the equivalent conductivity of the domain was less than the geometric mean conductivity. This example shows that one should expect a change in parameter values when the dimensionality is reduced.

Scale change. Scale is a complex concept having multiple connotations. The notion of *support* is important to characterize and relate different scales in subsurface hydrology. Support is the length, area, or volume for which a single value of a porous medium property is defined and no variations in this or other properties are taken into account. The size of an individual sample, or the size of a discrete spatial element in the flow model, are typical examples of support. The terms "resolution," "pixel size," "grid size," and "voxel size" are used often to define the resolution in terms of length, area, or volume. An area or a volume that is sampled with given support determines the extent of measurements. Distances between sampling locations define the spacing, which is also a function of scale. Blöschl and Sivapalan (1995) suggested using the triplet of numbers *support-spacing-extent*, rather than a single value of support, spacing or extent, to characterize the scale of a hydrologic study.

In practice, vadose zone investigations generally define the supports of core scale, soil profile or "pedon" scale, field scale, and watershed scale operationally, i.e. based on the measurement setup and available equipment. Increasing the linear size by about two orders of magnitude generally corresponds to a transition from one of these scales to the next one, as shown schematically in Fig. 2-3. Changes in the spatial scale are usually reflected by changes in the temporal scale as shown in this figure.

Scale change with upscaling. This category of model abstraction recognizes the need to alter model structure when the spatial scale changes. Model equations, variables and parameters change as the scale changes. A key premise of upscaling is the possibility to derive parameters of a coarser-scale model from parameters of a finer-scale model.

To be effective, all upscaling techniques must use the correct statistical representations of relatively rare but essential features at the finer scale since these features often govern relevant media properties or processes at the coarser scale. For example, if the hydraulic conductivity is distributed lognormally, then five percent of a fine-scale representative elementary volume

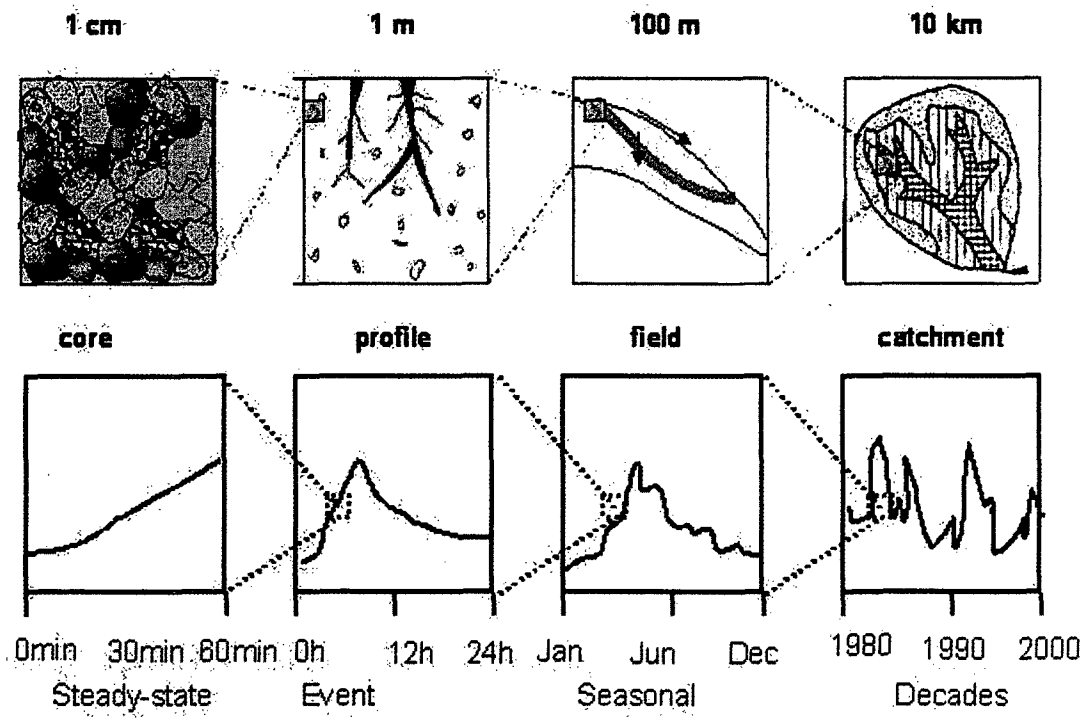

Figure 2-3. Spatial and temporal operational scales in hydrology (Pachepsky et al., 2006).

(REV) will conduct 95% of all flow, which implies that relatively rare features at the smaller scale will control flow at the coarser scale. Macropores (i.e. relatively large pores) provide another example of the importance of relatively rare fine-scale features. Relative to smaller matrix pores, macropores are rare in soils and are easy to miss during sampling. Yet, continuous macropores largely control rates of water flow and solute transport in a soil profile. Similarly, lateral preferential flow pathways in the subsurface are fine-scale features at the field or watershed scale, and relatively difficult to locate. Yet, lateral preferential flow pathways may well control lateral flow and solute transport often at the larger scale.

Scale change with aggregation. Aggregation also leads to a change in the governing equations and model parameters. However, unlike with upscaling, no relationship is assumed between the model parameters at the fine and coarse scales. Parameters of the coarser-scale model are deemed to be lumped, which suggests that field data are needed to calibrate the coarse scale models. An example is the use of a water budget soil flow model (Fig. 2-2a) at the field scale, while the Richards equation is used at the soil profile scale (Fig. 2-2b). Soil water retention is then parameterized in terms of field capacity at the coarse scale, whereas soil water retention curves are used at the fine scale. No reliable relationship exists between the water content at field capacity and the soil water content at a specific value of the pressure head, and therefore no relationship exists between the coarse- and fine-scale soil water retention parameters.

Aggregation can be also implemented without a change in the model equations by combining several soil horizons or geologic strata. For flow and transport in vadose zone, one common application is to replace a heterogeneous soil profile with an equivalent homogenous profile while retaining the Richards equation as the flow model (Zhu and Mohanty, 2002). In such case, flow and transport parameters are still lumped. Attempts to determine the effective hydraulic properties of the equivalent soil profile from the layer properties have shown that the effective properties depend not only on layer properties as such, but also on the type of predominant water regime (infiltration or evaporation).

Many examples of distributed watershed modeling with various degree of sub-watershed aggregation have recently been developed in surface hydrology. In general, excessive aggregation worsens model performance. For example, Boyle et al. (2001) showed that the aggregation from eight to three sub-watersheds did not worsen model performance, whereas aggregating all sub-watersheds in only one watershed did.

Metamodeling. Metamodeling is a group of abstraction methods that uses results of multiple simulation runs to extract information helpful for simplifying a complex model. Metamodeling literally means modeling a model. Also known as the repromodeling (Meisel and Collins, 1973) or response surface modeling, Metamodeling creates a relatively simple empirical model intended to mimic the performance of a large complex model in order to reproduce the object model's input-output relationships (Davis and Bigelow, 2003). A common way to develop a metamodel is to generate "data" from a number of large-model runs and then to use statistical methods to relate model input to model output without attempting to understand the model's internal working.

Machine learning methods have become a popular means to build metamodels. Artificial neural networks (ANNs) are the most popular among these since they are powerful approximators and, as such, are popularly used to relate multiple input variables to outputs from the complex model (Hecht-Nielsen, 1990). Examples of the application of artificial neural

networks to mimic MODFLOW output for a range of scenarios for particular remediation sites were published as early as 10 years ago (Kron and Rosberg, 1998; Masket et al., 2000). The use of ANNs requires development of a large number of training datasets covering the range of possible scenarios of forcing variables. Generating such datasets requires extensive computing efforts, but after the ANN is trained, computations with the derive ANN are several orders of magnitude faster than simulations with the original model. An example involving regional wastewater planning in which, for reasons of computational efficiency, an artificial neural network was employed is given by Wang and Jamieson (2002). The ANN replicated the process-based model in multiple evaluations of the model output during optimization aimed at determining both the best sites and individual discharge standards. Other machine learning methods such as support vector machines, classification and regression trees, and genetic programming are increasingly being appreciated in subsurface hydrology.

Machine learning methods can be used to simulate not only the model output of interest, but also the results of any part of the computations performed during a model run. For example, Hassan and Hamed (2001) demonstrated the use of ANNs to predict particle trajectories in a particle-tracking algorithm simulating plume migration in heterogeneous media. Their metamodeling approach substantially improved the computational efficiency of the entire algorithm.

2.3 ABSTRACTION OF PARAMETER DETERMINATION

Discretization. Using a set of discrete parameter values, instead of continuous functions, can sometimes lead to substantial simplifications. This simple but very important abstraction approach is commonly used in flow and transport modeling by employing soil and geological textural maps to define soil or sediment structural units that have the same hydraulic properties, even though real-world hydraulic properties may more gradually change from one unit to another. Zonation of the hydraulic conductivity was found to be efficient when geophysical and hydrogeological data were combined (Chen et al., 2001, 2004; Hubbard et al., 2003). Automated zonation is now also feasible (Tsai, 2003), which has the advantage of not needing a specific equation to simulate the dependence of parameters on the spatial coordinates.

Abstraction by temporal discretization is often used to create soil surface boundary conditions or discharge values. The temporal support of precipitation and evaporation or discharge is then coarsened to time intervals of months or years to speed up computations or to avoid generating synthetic weather patterns. Unfortunately, this type of abstraction can potentially also introduce substantial errors. For example, McLaren et al. (2000) studied the transport of ^{35}Cl in fractured tuff at Yucca Mountain and showed that changing the infiltration regime from a constant value of 5 mm y^{-1} to a pulsing regime with the same annual average value greatly enhanced the transport of the radioactive isotope. The effect of infiltration pulsing was model dependent; low rates of mass exchange between preferential flow zones and the matrix further enhanced transport to make the predictions more consistent with observations (Bandurraga and Bodvarsson, 1999). Relationships between flow properties and water contents are highly nonlinear in the vadose zone. Temporal coarsening for this reason may cause simulated plumes to move much slower and to become much more compact from they would have been otherwise.

Pedotransfer functions. Parameters of models for flow in variably-saturated porous media are nonlinear functions of the pressure head or water content. The parameters in these hydraulic functions are notoriously difficult to measure. Accurate measurement of water and solute fluxes

in unsaturated soils remains a major research issue; no routine methods have been devised to-date. Therefore, defining parameters using inverse methods is often problematic. Substantial efforts have been made to estimate the hydraulic parameters from data available from soil surveys or borehole logs. Empirical functions used for this purpose are often called pedotransfer functions (PTFs). Extensive work has been carried to develop PTFs. The proceedings of two international conferences (van Genuchten et al., 1992, 1997) and a book on this topic (Pachepsky and Rawls, 2004) provide a panoramic view of these fast-developing studies.

The performance of pedotransfer functions can be evaluated in terms of their accuracy, reliability, and utility. In broad terms, the accuracy of a PTF can be defined as the correspondence between measured and estimated data for the data set *from which a PTF has been developed.* The reliability of a PTF may be viewed as the correspondence between measured and estimated data for data set(s) *other than the one used to develop the PTF.* Finally, the utility of a PTF in model applications can be assessed in terms of the correspondence between certain *measured and simulated environmental variables.*

PTFs developed from regional databases have been shown to be more reliable in regions with similar soil and landscape histories. For example, PTFs developed from the country-wide US database by Rawls et al. (1982) appear to be more robust than PTFs developed from regional databases. However the accuracy of any PTF outside of its development dataset is essentially unknown, and using multiple PTFs instead of relying on a single PTF may well be preferred. Ye et al. (2004) suggested averaging spatial variability models for unsaturated fractured tuff in situations where standard information criteria provide an ambiguous ranking of the models such that it was not justified to select one model and discarding all others. Guber et al. (2006, 2008) likewise used an ensemble of pedotransfer functions to simulate water flow in variable saturated soils.

Recent developments in pedotransfer technologies have focused on the use of spatially dense physical information related to soil cover. Using topographic information is based on the hypothesis that some relationship may exist between the soil hydraulic properties and topographic variables (Pachepsky et al., 2001) since (a) the basic properties of soil are known to be related to landscape position, and (b) soil hydraulic properties are related to basic soil properties. Soil water retention was found to exhibit a strong dependence upon terrain attributes in the work by Rawls and Pachepsky (2002) who used U. S. soil survey data from the National Resources Conservation Service (NRCS). Terrain attributes were also used by Romano and Palladino (2002) to improve PTFs.

The use of hydrogeophysical, remote sensing, and crop yield data is based on a similar premise as using topography. The basic soils data should affect both the sensor readings and the soil hydraulic properties. Therefore, some relationship between the dense data and the hydraulic properties should be expected. A recent first book on hydrogeophysics (Rubin and Hubbard, 2005) summarized the rapid progress in this field. Cross-borehole resistivity measurements are now also showing promise in improving estimates of flow and transport properties of the vadose zone (Looms et al., 2008; Deiana et al, 2008). One recent example involved the use of airborne gamma radiometric sensing to estimate the clay content of surface soils and using a simple pedotransfer function to convert this information into a spatial representation of soil water retention parameters (Smettem et al., 2004). In another example, Timlin et al. (2002) related biophysical information from yield maps to the soil field capacity.

The use of dense auxiliary data in PTFs reflects an attempt to trade data quality for data quantity. Since dense coverage can be treated as an image, image analysis techniques may be

used for segmentation and classification, as well as for delineating the structural units of soils. Data assimilation techniques may be suited also for combining soil survey and sensor information (McLaughlin, 1995). PTFs developed with auxiliary data are probably highly site-specific and, therefore, useful mostly only for sites for which they were developed. Nevertheless, the availability of sensor data can make such PTFs a viable component of supplying parameters of models for water flow in the vadose zone.

2.4 SYSTEMATIC MODEL ABSTRACTION

Earlier collaborative work between ARS and NRC staff resulted in the development of a systematic and objective approach for model abstraction (MA) relevant to subsurface flow and transport modeling (Neuman and Wierenga, 2003; Pachepsky et al., 2006). The approach included (a) justifying the need for model abstraction, (b) reviewing the context of the modeling problem, (c) selecting applicable MA techniques, and (d) determining alternative MA directions and simplifying the base model in each direction.

We emphasize here that model abstraction is always site-specific. Appendix A provides details of the model abstraction process. In this section we give only a brief description.

2.4.1 MODEL ABSTRACTION STEPS

The MA process starts with an existing *base* model that can be calibrated and used in the simulations. The *key output* of the model is defined in this first step. The output provides the necessary and sufficient information required to make decisions about a certain issue of interest.

The model abstraction process includes the following steps.

1. Justify the need for the envisioned model abstraction
2. Review the context of the modeling problem
3. Design the model abstraction using selected techniques
4. Perform model abstraction

Model abstraction justification. Any model simplification requires calibration of the abstracted simpler model and its confirmation with multiple model runs. This is a separate modeling project that demands resources, and may be used later to justify the need for model abstraction. The base model may need abstraction for one or more of the following reasons:

- The base model includes a complex description of processes that cannot be observed well, but still needs to be calibrated; the calibrated values of parameters of those processes may be very uncertain.
- The base model propagates uncertainty in the initial distributions, the parameters, and the invoked boundary conditions (forcing) in a manner that creates unacceptable uncertainty in the key output.
- The base model produces inexplicable results in terms of the key output.
- The base model requires an unacceptable amount of resources for the computations, data preprocessing, or data post-processing (e.g., the base model is not suited to be part of an operational modeling system that requires real-time data processing).
- The base model lacks transparency to make the model and its results explicable and believable to users of the key output.

The lack of transparency of the base model is often a result of abstraction motivated by the perception of potential users or critics of the simulation results. Incomprehensible simulation results with the base model or the unacceptable resource demand of the base model are often reasons that preclude the completion of a modeling project.

The need for abstraction may stem also from uncertainty in the calibrated parameter values because of the limited observation ability or uncertainty in the simulation results. The decision to carry out the model abstraction may be based on the statistics of parameter estimates and the key output, as discussed by Pachepsky et al. (2006).

Context of the modeling problem. The context of a modeling project has to be reviewed to assure the objectiveness and comprehensiveness of the selected model abstraction. One must realize which details and features of the problem are to be omitted or de-emphasized when abstraction is performed. Neuman and Wierenga (2003) list the following issues that constitute the context:

1. What is (are) the question(s) that the base and abstracted models are to address? The answer should consider (a) the existing or potential problem in which modeling is one of the solution instruments, (b) the existing or potential causes of the problem, (c) the issues needing resolution, and (d) the criteria to be used for deciding the level of resolution. The key output has to be provided with the spatial and temporal scale at which model abstraction is evaluated. Acceptable criteria for accuracy and uncertainty of the model output must to be established by the end users. In some cases mandatory regulations exist on performance measures that articulate the statistics to use in a particular case. If there are no such regulations, then the statistics have to be selected and defined; they should describe simple and clear ideas about the correspondence between the data and the simulations, such as how variability in the model errors compares with variability in the data, if the model residuals have trends, or if systematic relative or absolute errors exist in the predictions.
2. What type of data is available to calibrate the base and abstracted models and to test them with respect to the key output? An essential prerequisite is to have a database that is as broad as possible. The database must include data from public and private sources, cover both quantitative and qualitative (expert) information, and encompass both site-specific and generic information. A list of base model inputs and outputs would provide a convenient template for the necessary parts of the database. It is imperative to have statistics of all available model inputs and measurable model outputs, including (a) the initial distributions of water contents and/or pressure heads, and the concentrations of solutes of interest, (b) surface and subsurface soil properties including horizon or layer thicknesses, porosities, bulk densities, adsorption parameters, and in some cases redox conditions, (c) the forcing that provides the boundary conditions and the source/sink terms, and (d) the model parameters typical for the site. The latter can be inferred from an ensemble of pedotransfer functions, provided the necessary soil survey and/or borehole log data are available to serve as pedotransfer inputs. Statistics includes the type of statistical distribution used, median values and variability measures, information about observed outliers, and correlations between parameter values.
3. To make sure that the abstracted models are sound, additional information may have to be collected to ensure that the abstracted models include descriptions of all essential processes of flow and transport at a given site. This information may be of lower quality compared with the necessary part of the database. For example, one must be sure to not ignore certain small-

scale internal heterogeneities that may have a dominant effect on flow and/or transport at the scale of interest.

2.4.2 MODEL ABSTRACTION DESIGN AND EXAMPLE

The design of a model abstraction project should include selection of the model abstraction techniques, definition of uncertainties that have to be simulated using Monte Carlo or other methods, and selection of the software to be used (Pachepsky et al., 2006). The selection of model abstraction depends on the reasons for the model abstraction. In general, model abstraction can lead to simplifications via:

- the number of processes being considered explicitly,
- simpler process descriptions,
- coarsening the spatial or temporal support
- the number of measurements to be used for reliable parameter estimation,
- reduced computational burden,
- simplified data pre-processing and post-processing.

An example of model abstraction design and implementation was developed in a study focusing on infiltration in a variably-saturated soil subject to natural rainfall (Pachepsky et al., 2006). The base model for this study was previously developed by Jacques et al. (2002) who simulated water flow in a layered soil using a single-continuum pore space model (media b in Fig. 2-2). Parameters were estimated by calibration using measured water content and pressure head time series. The key output was the soil water flux at three depths. The base model provided an excellent fit to the soil water contents but failed to simulate measured soil water fluxes. The results could not be explained well (Jacques et al., 2002).
Fig. 2-4 shows the selected model abstraction techniques, the uncertainty treatment, and the software selected (Pachepsky et al., 2006). Four abstraction techniques were used. Two techniques simplified the base model via (1) a simpler process description, i. e., by changing the porous media model from a single-continuum (Fig. 2-2b) to a water budget model (Fig. 2-2a), and (2) by aggregating soil layers into a single layer with effective hydraulic properties. Two other techniques simplified the parameter determination by using only laboratory data, or by using an ensemble of pedotransfer functions. Fifty Monte-Carlo simulations were performed with each abstracted model using data on variability of calibrated, measured, or estimated hydraulic properties. The HYDRUS 2D and MWBUS software packages were used to simulate water flow in the single-continuum medium and with the water budget model, respectively. The model abstracted from the hierarchy of models correctly simulated fluxes and showed why inexplicable results had been obtained with the more complex model. Simultaneous calibration of a large number of parameters in the base model caused unrealistic flow simulations that included substantial runoff generation, whereas no runoff was observed during the experiments. The model abstraction via pedotransfer functions showed that an ensemble of pedotransfer functions produced a satisfactory representation of field uncertainty in the soil hydraulic properties.

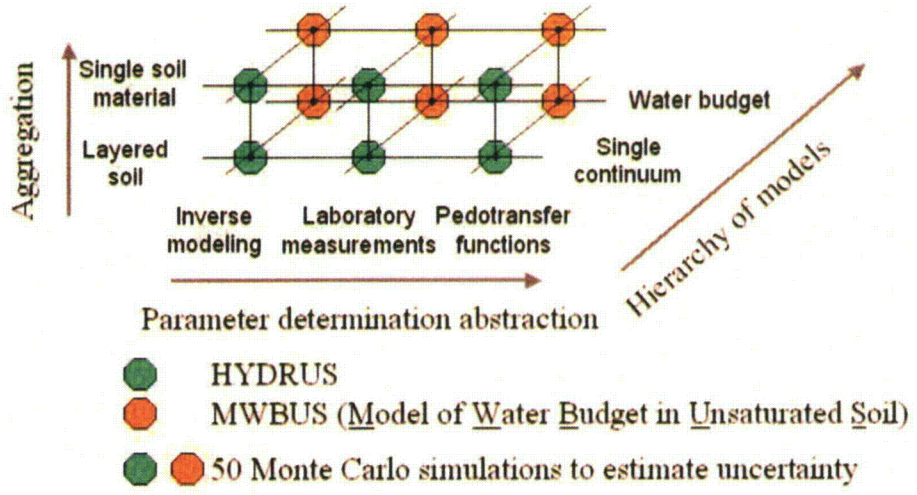

Figure 2-4. Design of model abstraction via model structure and parameter determination

2.5 MODEL ABSTRACTION VS. ARBITRARY SELECTION OF A "SIMPLE" MODEL

Models used in performance assessments of waste disposal sites generally ignore small-scale heterogeneities in space and time. Preferential pathways are typically ignored when a single-continuum pore space representation is used. Observed strongly asymmetrical distributions of the pore water velocity are then often represented by an average velocity. Similarly, strongly asymmetrical temporal distributions of actual rainfall or discharge are represented by rates averaged across long periods of time. Thus, the often-used models are actually abstractions of more realistic models that explicitly account for spatial and temporal heterogeneities.

One argument for using a simplified model based on averaging is that locating and quantifying small-scale spatial and temporal heterogeneities has substantial conceptual and resource limitations. However, the magnitude of errors caused by ignoring the small-scale heterogeneities is never known *a priori*. Recent research shows that heterogeneities are common, and that even slight reductions in soil texture may lead to flow barriers and associated lateral flow. These lateral flow paths may lead to solute mass losses, reduced vertical fluxes, and increased longitudinal dispersivities (Looms et al., 2008). This shows that it is imperative to evaluate possible prediction errors when the "simple" model is used. Deriving the simple model from the more complex base model provides opportunities for such an evaluation.

3 EXPERIMENTS TO TEST AND CONFIRM MODEL ABSTRACTION FOR FLOW AND TRANSPORT IN SOILS

In this study we apply a systematic abstraction process to base models accounting for heterogeneities in subsurface flow and transport. The abstraction will lead to often-used simplified models, with as overall objective the estimation of pattern and magnitudes of possible errors obtained with the simplified models. The purpose of this section is to provide an analysis of the exhaustive ARS OPE3 vadose zone flow and transport database within the context of model abstraction, and to describe the experiments and measurements carried out to develop the base flow and transport model. This model was developed and then subjected to abstraction as described in the following sections.

3.1 Outline of experiments to test and confirm model abstraction in soils

A century-long history of experimentation on solute transport in soils has resulted in a multitude of advanced experiment setups and procedures, as well as methods of data analysis. Experiments may be carried out at different scales as shown in Fig. 2-3. Currently no single-source compendium of experimental methodologies exists to study flow and transport in soils, and to characterize the ability of soils to transmit and retain chemicals. One exception may be a recent monograph by Dane and Topp (2002). Applying a model to infer soil properties from experimental results is still the standard method of data analysis.

Generally, there are three sources of information about solute transport in soils: outflow breakthrough sampling, destructive soil sampling after transport has occurred, and monitoring of pore solution concentrations within the soil during the observed solute transport event. The applicability and relative reliability of those sources depends on the scale of the study.

Outflow breakthrough sampling is probably the most reliable methodology since it effectively integrates solute transport for the given support area or volume. However, its applicability is limited when no or little breakthrough is present. Such situations are typical for strongly absorbed chemicals, colloids and microorganisms, and generally for all solutes if the soil is unsaturated and transport is slow. Even if considerable breakthrough occurs, the presence of several transport and retention processes may complicate the interpretation of results. This because multiple parameters describing those processes cannot be simultaneously inferred from a single breakthrough curve.

Destructive post-experiment sampling is a useful complement to breakthrough data in that this may help to diminish or eliminate ambiguity in parameterization of the retention processes in soil column experiments. As the scale coarsens, the resource demand may become daunting and sample cross-contamination may become an issue, while field variability may increasingly compromise data reliability. A destructive sample may not contribute much to understanding the physical or chemical heterogeneity of a soil.

Monitoring the pore solution composition is in principle the best approach for obtaining data. Unfortunately, monitoring devices tend to distort the concentration field within a soil. It is often not clear what part of the soil solution affects the sensor reading, or what part of the pore solution is extracted. As the observation scale coarsens, field variability introduces additional uncertainty in the data.

Although the ambiguity of data and/or their analysis undoubtedly creates difficulties in solute transport experiments at the field scale, the importance of the vadose zone in controlling

chemical fate and transport in the subsurface requires the development and application of field-scale predictive models. These field-scale models require field data for their calibration and testing. A list of structural heterogeneities that are important to consider within the context of vadose zone modeling is given in Appendix A1. 2. Experimental setups in general should addresses two types of heterogeneities: differences in water mobility in different parts of the soil pore space, and the effects of restricting layers and the capillary fringe on lateral transport.

Two field experimental setups were implemented as part of this study. The first setup was meant to quantify solute dispersion in unsaturated soil and to evaluate the need for explicit simulation of prevailing soil physical heterogeneities. This setup exploited the ability of breakthrough concentrations to serve as integrators of transport at the support scale. A schematic of this first experiment is shown in Fig. 3-1. A tracer was applied to a relatively small area around a pumping well, with the irrigated area being substantially larger than the tracer application area. Ground water was pumped from the well, while the pumped water volume and the tracer concentration were continuously monitored.

The second experimental setup was meant to evaluate the potential contribution of the variably-saturated zone and the capillary fringe to lateral chemical transport along a restrictive fine-textured layer. The lateral flow and transport processes were found to be relatively complex since the perched groundwater table fluctuated substantially in time. A schematic of this experiment is shown in Fig. 3-2. The tracer application area during the experiments was continuously irrigated, leading to a gradually expanding groundwater mound. The groundwater composition during the experiment was monitored using observation wells located within the projected plume.

In both experiments the chemical application area had a radius of several meters to accommodate the scale of possible releases of contaminants from waste storage facilities. A conservative tracer was used. No soil solution sampling during the experiments was envisioned. The irrigation rate was selected such that the soils remained unsaturated. Soil moisture sensors had been installed to monitor the soil moisture content. Groundwater depths were measured, while surface runoff was monitored and, if found significant, intercepted and measured. All vegetation was eliminated from the chemical application area. A base model was developed for each experiment to accommodate the encountered complexities. Application of the model abstraction process will be illustrated for different key outputs.

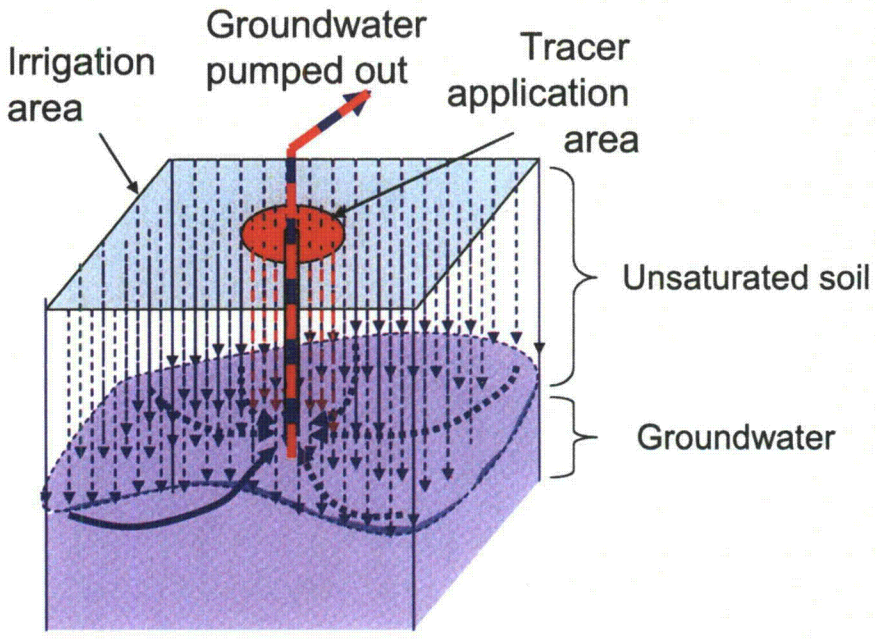

Figure 3-1. Schematic of the flux experiment.

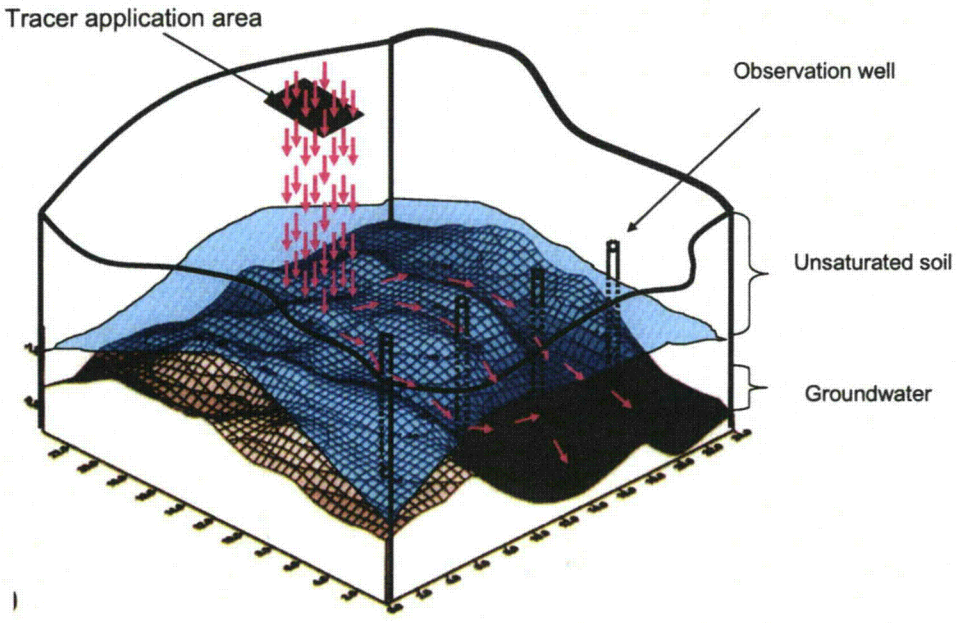

Figure 3-2. Schematic of the lateral flow experiment.

3.2 THE OPE3 EXPERIMENTAL SITE AT THE BELTSVILLE AGRICULTURAL RESEARCH CENTER

3.2.1 GENERAL DESCRIPTION

The study area was the 22-ha USDA-ARS "Optimizing Production Inputs for Economic and Environmental Enhancement," or OPE3, experimental watershed in Beltsville, MD. An aerial view of the watershed is shown in Fig. 3-3. The watershed drains into a riparian wetland forest that contains a first-order stream (Gish et al., 2002, 2005; Chinkuyu et al., 2006). The vadose zone at the site was formed in fluvial deposits. Soils are mostly sandy loams and coarse sands on a clay layer with surface slopes ranging from 1 to 4%. A description of the soil cover is given in Table 3-1. The watershed is in agricultural use and has been under corn since 1998. Tillage practices were the same each year, with fields typically being disked about one month prior to a second disking operation, followed by planting.

OPE3 is a small watershed that is intensively instrumented, and where all data are geolocated with a differential or kinematic global positioning system. Data collection included:

- Over 40 km of ground penetrating radar (GPR) data have been collected and analyzed.
- Every two years, soil cores were extracted to determine the spatial correlations and distributions of organic matter, pH, and sand, silt, and clay percentages.
- Electromagnetic induction (EM-31 and EM-38) data were collected for two of the watersheds.
- 36,000 volumetric water content measurements at 48 locations were collected daily.
- Micro-meteorological stations with eddy covariance systems monitored climatic conditions.
- Multiple pesticide vapor flux towers were operational after pesticide application.
- Water and chemical (N, P, and pesticides) runoff fluxes were collected from each watershed.
- Watershed B (Fig. 3-3) was instrumented with 52 groundwater observation wells.
- Corn grain yields were measured using a grain yield monitoring device.
- Aircraft and satellite remote sensing imagery were collected. Ground- and tower-based reflectances were collected as needed.
- Plant growth and development were measured periodically during the growing season.
- 180 observation wells in the riparian wetland were monitored for anions and pesticides.
- Stream flows and chemical fluxes in the stream were measured at five stations within the riparian wetland.
- Wetland soil cores were extracted up to one-meter depth and analyzed for grain size, bulk density, carbon content, hydraulic conductivity, water content, and denitrification potential.
- Dissolved gas was measured in groundwater samples throughout the wetland for evidence of denitrification and methanogenesis.
- Dissolved oxygen, dinitrogen, nitrous oxide, and methane were measured.

The experimental site of this particular work is located at the 3-ha field B of the OPE3 experimental watershed. The field is currently instrumented with 64 soil moisture sensors (EnviroSCAN, SENTEK Pty Ltd., South Australia) distributed among 12 capacitance probes (Fig. 3-4) that measure soil water content at depths from 10 to 180 cm every 10 min year-round. Table 3-2 shows sensor depths and durations of the continuous observations.

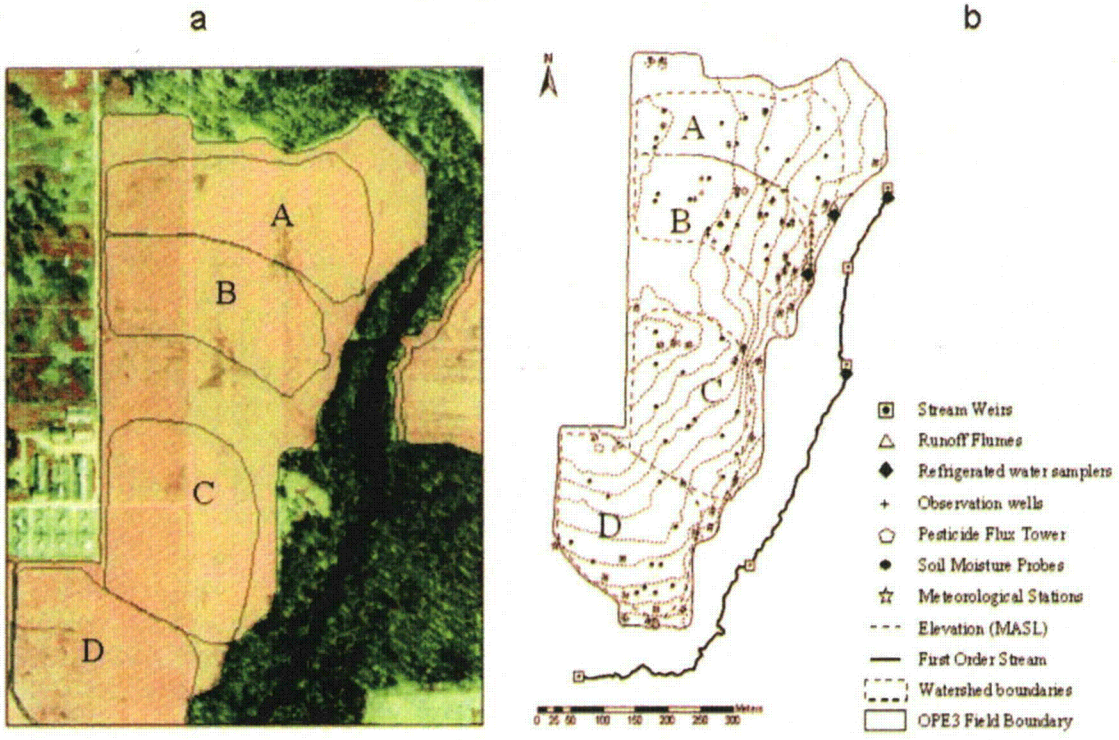

Figure 3-3. The USDA-ARS OPE3 research watershed; a – aerial view, b – instrumentation. A, B, C, D – research fields.

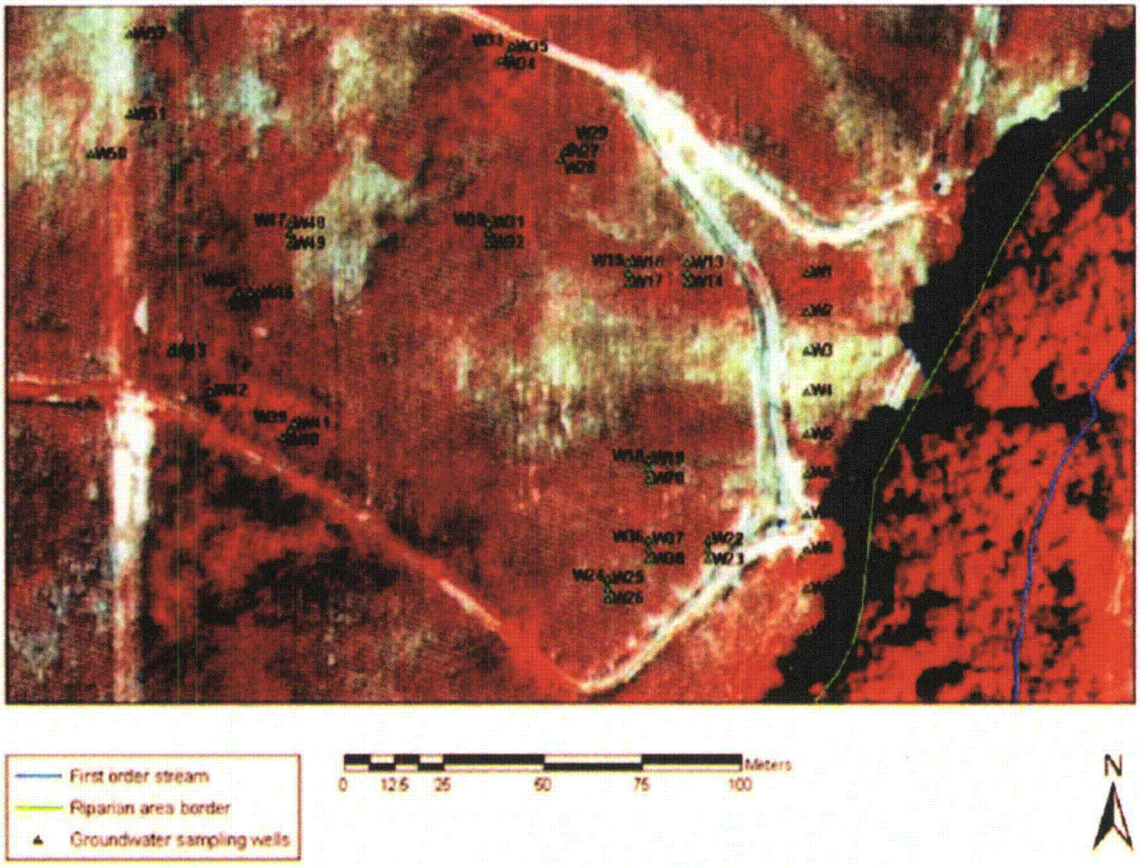

Figure 3-4. Locations of groundwater wells and soil moisture sensors at the Field B shown at the false color aerial image.

Table 3-1. Soil cover of the OPE3 crop production area.

Soil associations and soil series	Cove-rage %	Topsoil texture	Description
Downer-Muirkirk-Matawan	49	Sandy loam	
Downer			Coarse-loamy, siliceous, semiactive, mesic Typic Hapludults
Muirkirk			Clayey, kaolinitic, mesic Arenic Paleudults
Matawan			Fine-loamy, siliceous, semiactive, mesic Aquic Hapludults
Bourne	23	Fine sandy loam	Fine-loamy, mixed, semiactive, thermic Typic Fragiudults
Matawan-Hammonton	23	Loamy sand	
Hammonton			Coarse-loamy, siliceous, semiactive, mesic Aquic Hapludults
Downer-Ingleside	5	Loamy sand	
Ingleside			Coarse-loamy, siliceous, semiactive, mesic Typic Hapludults

Field B was equipped with 52 groundwater monitoring wells, 41 of which are still active (Fig. 3-4). Some of the wells were instrumented with Divers (Van Essen Instruments, Giesbeek, The Netherlands) to measure groundwater levels every 30 min.

Other monitoring equipment at Field B included an automated Sigma 980 runoff flow meter (Hach Company, Loveland, CO) that measured water flow every 10 min and periodically collected surface runoff samples so that water and chemical fluxes could be determined. The flume was installed at the field surface outlet (Fig. 3-4). The automated runoff sampler monitored fluxes on an event basis. An energy balance meteorological station with an eddy covariance tower was installed 20 m south of the boundary between Fields A and B (Fig. 3-3b).

3.2.2 EXISTING OPE3 INFORMATION RELEVANT TO FLOW AND TRANSPORT IN SOILS

Results of surveys, monitoring, and hydrologic experiments at OPE3 were reviewed according to the outline in Appendix A to develop assumptions for constructing the base model.

3.2.2.1 SMALL SCALE STRUCTURAL UNITS AND HETEROGENEITIES

The focus here was on heterogeneities that could be revealed at the core scale and could control the behavior of flow and transport at the field scale. The following information was used:

- Borehole data of soil texture and composition
- Soil water retention measurements on undisturbed samples,
- Field and laboratory soil hydraulic conductivity measurements.

3.2.2.1.1 BASIC SOIL PROPERTIES

Data on soil texture, organic matter content, and pH had been collected during a soil survey performed by the USDA-NRCS in 1997 using samples representing distinct genetic horizons. Selected data are shown in Fig. 3-5. The organic matter content demonstrated a typical decrease with depth (Fig. 3-5a), indicating the absence of recent substantial changes in soil stratification caused by floods or erosion. The sand content exhibited large variations from horizon to horizon. Although the soils were characterized as having a coarse texture (Table 3-1), sand content varied in the range between 50 and 90 % (Fig. 3-5b), with often drastic changes from one horizon to another in some profiles. Soil clay content near the soil surface tended to increase with depth, but more deeper decreased to a depth of about 90 cm as shown in Figs. 3-5c,d. Clay content varied substantially at depths below 90 cm. The relationship between soil clay and sand content was linear below 60 cm (Fig. 3-5e) which indicates a potential for having isolated lenses of predominantly coarse and predominantly fine material. Soil pH tended to have higher values at places where the clay content was lower. Values of the pH smaller than 4. 5 were encountered at greater depths. This indicates a potential for aluminum mobility and soil mass cementation that would restrict the mobility of water and solutes in some parts of the soil profile.

3.2.2.1.2 SOIL HYDRAULIC PROPERTY MEASUREMENTS

To evaluate possible effect of the macroporosity on the soil hydraulic properties, undisturbed samples having 20 cm^2 support area were taken for hydraulic conductivity measurements at the same support size in both the laboratory and the field. An example of water retention data from three depths with increasing clay content is shown in Fig. 3-6. Samples taken close to soil surface showed well-defined macroporosity. A small decrease in the pressure head close to zero caused a substantial decrease in the water content of these samples. This decrease is a result of

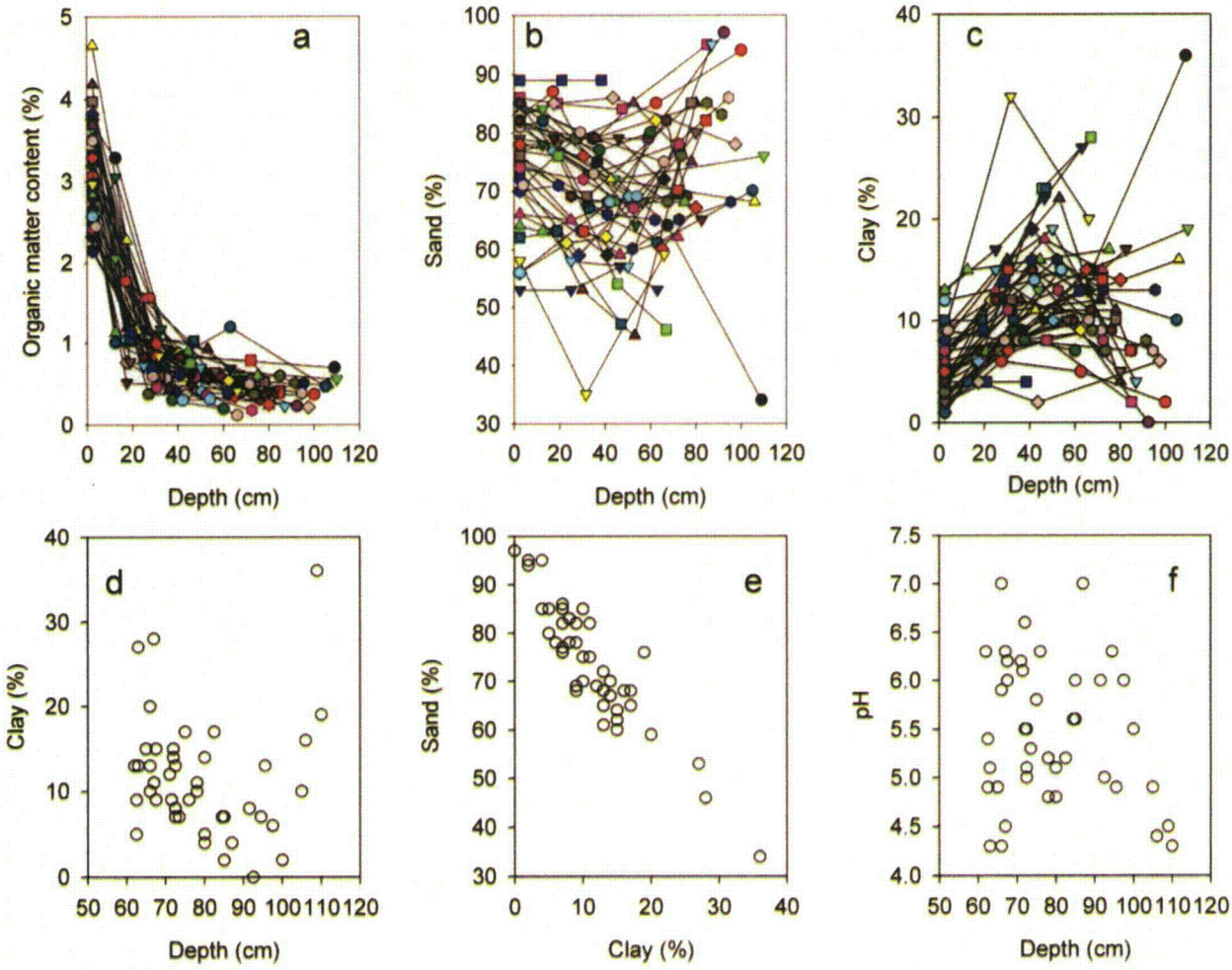

Figure 3-5. Basic soil properties at the OPE3 watershed.

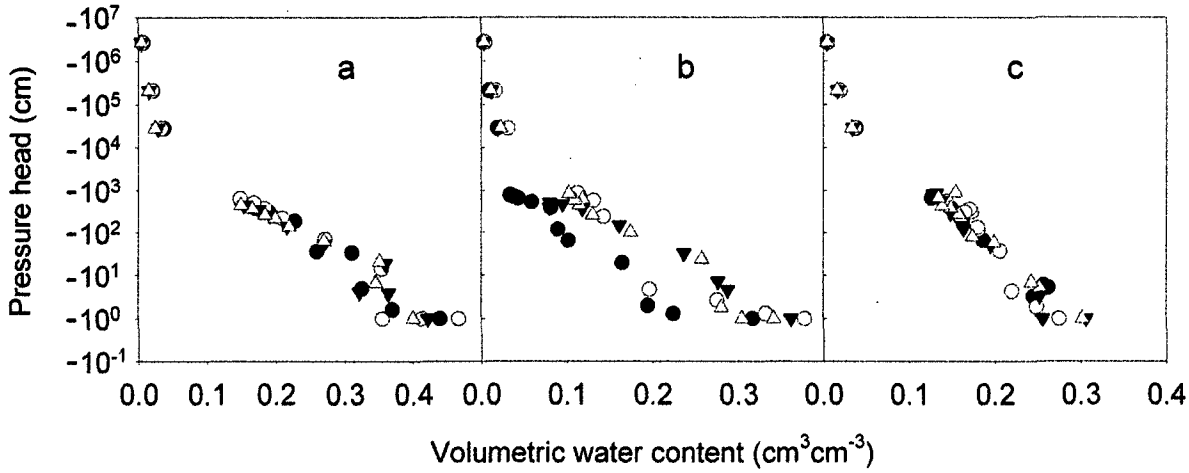

Figure 3-6. Soil water retention of samples at locations 1 and 2 near well w52 at field B; a) 2-5 cm depth, b) 20-23 cm depth, and c) 47-50 cm depth (●,○ – location 1,▲,▼ - location 2).

macropores being emptied. The effect is almost absent at 50 cm depth where the clay content is larger than close to the surface, and where root activity is also lower. Macropores may be less developed or at this depth and hence are more difficult to detect here because of their infrequent appearance.

Data for the saturated hydraulic conductivity corroborated the water retention data in terms of a decrease in macroporosity with an increase in clay content and a decrease in root activity. As shown in Fig. 3-7a, the maximum values of the hydraulic conductivity were similar at depths of 25 and 40 or 45 cm. However, a substantial part of the soil, about 25% at location 1 and 50% at location 2, did not conduct water at a measurable rate at a depth of 40-45 cm where the effects of macroporosity on water retention were observed.

Anisotropy in the saturated hydraulic conductivity is another consequence of changes in soil structure. Fig. 3-7b shows that the horizontal hydraulic conductivity was smaller than the vertical conductivity at a depth of 25 cm, whereas the reverse is true at a depth of 45 cm where all conductivity values were essentially zero of undisturbed samples taken to laboratory, with about half of the samples showing distinct non-zero horizontal conductivities. The data are in agreement with visual observations of seepage along the walls of a soil pit where the measurements were taken (Fig. 3-8). Seepage can be seen at a depth of 60 cm where the lateral conductivity was substantially higher than the vertical conductivity.

3.2.2.2 FIELD SCALE HETEROGENEITIES

Considerable field-scale heterogeneity was evidenced by observed groundwater levels and chemical compositions, measured soil water contents, ground-penetration radar surveys, remote sensing imagery, and maps of measured corn yield.

3.2.2.2.1 HYDROLOGICALLY ACTIVE ZONES AND SUBSURFACE FLOW PATHWAYS

Initially two sets of independent data were collected to determine optimal locations for subsequent soil core sampling. Photogrammetric and geophysical techniques were first used to provide a general characterization of the experimental watershed. Because surface slope and aspect influence both surface and subsurface hydrology, a 0. 25-m contour interval topographic map was derived from a stereo pair of aerial photographs and ground control points located with a submeter, a differential global positioning system (DGPS) receiver (Trimble 4000-SE, Sunnyvale, CA).

Electromagnetic induction (EM-38) was used to estimate relative clay contents near the soil surface in order to estimate infiltration rates (Doolittle et al., 1994). The results showed EM-38 values from 5 to 30. The EM data were divided into three equally sized populations, low (EM < 12), intermediate (17 >EM > 12), and high (EM >17) values.

The entire 7.5-ha site was next divided into different hydrologic groups based on surface topographic features and EM data. We assumed that areas with EM > 17 and a slope >2% would have a relatively low infiltration capacity, whereas areas with EM <12 and a slope < 1% would have relatively high infiltration capacities. All other areas were assumed to have medium infiltration capacities. Within each hydrological region of potential infiltration, 7 or 8 plots having dimensions of 25 x 25 m^2 each were randomly selected for higher resolution surveys (Fig. 3-9).

Ground-penetrating radar data were acquired for the entire 7. 5-ha field B along parallel north-south transects 25-m apart using a 150 MHz antenna. Within selected 25 by 25 m plots, additional GPR data were collected by towing the 150-MHz antenna along north-south transects

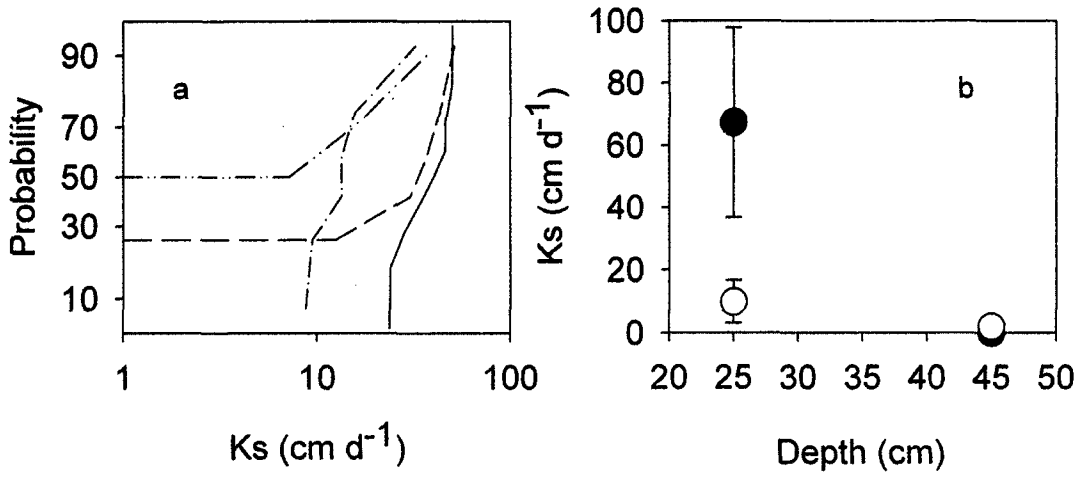

Figure 3-7. Probability distributions of the saturated hydraulic conductivity for 20 cm^2 support areas; a – field falling head measurements; ——— - location 1, depth 25 cm , — — —- location 1, depth 45 cm, —·—·— - location 2, depth 25 cm, —··—··— - location 2, depth 40 cm; b – constant head measurements of vertical (•) and horizontal (○) conductivities of undisturbed samples with 20 cm^2 support area in the laboratory (error bars show standard deviations).

Figure 3-8. Water seepage from the wall above restrictive soil layer.

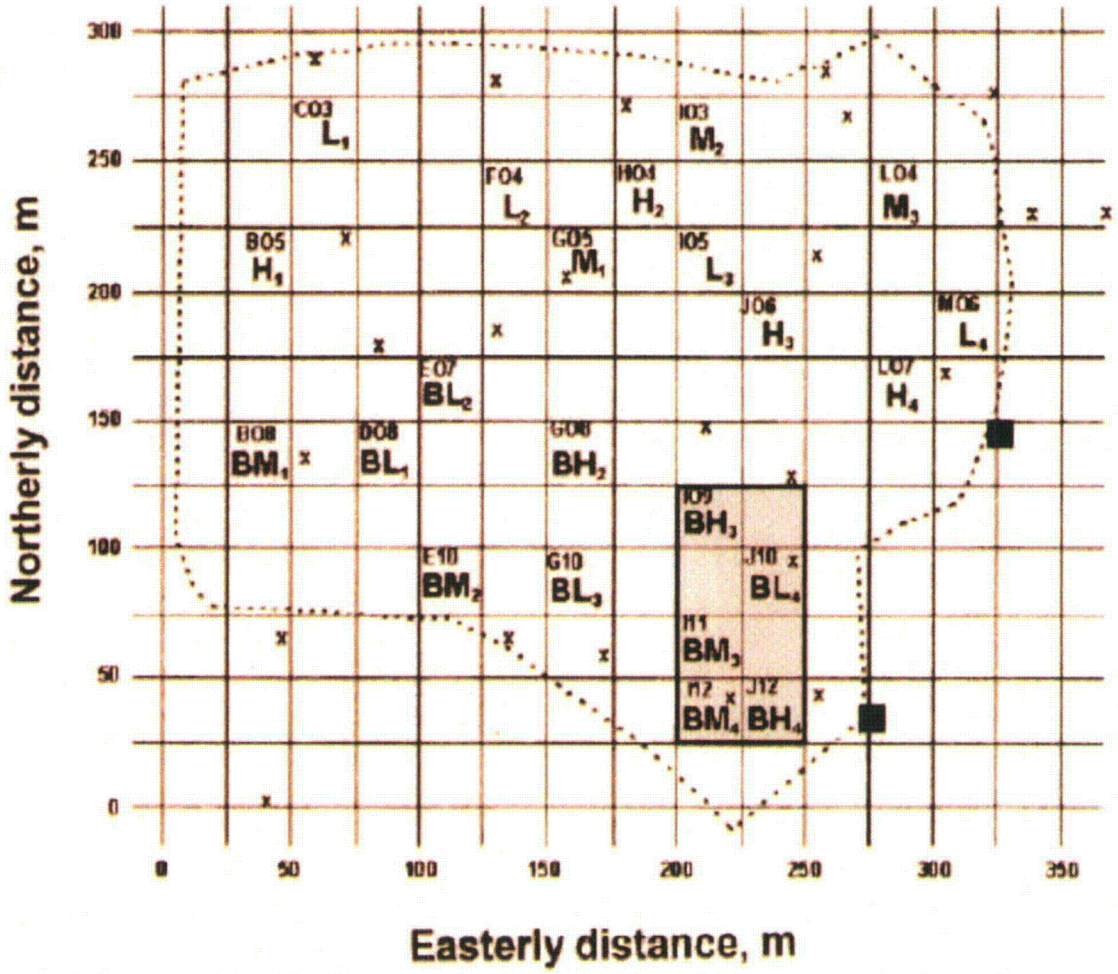

Figure 3-9. Layout of the 7. 5-ha watershed overlaid by a 25 by 25 m sample grid. Blocks with alphanumeric and infiltration capacity designations make up the stratified random sample of grid cells selected for soil moisture monitoring probes. The shaded rectangle in the southeast corner of the field site shows the 0. 5-ha subsection that was used for soil moisture measurements and flow verifications (after Gish et al., 2002. Permission to use this copyrighted material is granted by Soil Science Society of America Journal).

that were 2 m apart. GPR data were acquired in digital form so that a trace of the subsurface reflections could be produced using RADAN software (Geophysical Survey Systems, Salem, NH). The GPR data were distance-normalized and low-pass filtered prior to data interpretation. The GPR trace followed the shallowest contrasting dielectric discontinuity. Strong dielectric reflections were considered to be manifestations of water holding capacity differences due to textural discontinuities such as the presences of a clay lens below a sandy soil. Generally, the clay lens (high dielectric) occurred below the C horizon, which frequently contained much gravel (low dielectric). Depths to the strongest reflection were as shallow as 0.9 m and as deep as 3.4 m, but the majority of the data gave the strongest reflection at depths of 1.3 and 2 m. A GPR image profile is shown in Fig. 3-10. The first continuous restricting layer in this figure is situated immediately above the first continuous strong reflection, shown as a dotted line between depths of 1 and 2 m. The reflection of the restricting layer was not registered in about 5% of the total transect length. The topography of the first restricting layer was constructed using kriging assuming an omnidirectional variogram. We used the software packages GEO-EAS (EPA, Las Vegas, NV) and GS_ (Gamma Design Software, Plainwell, MI) for this purpose. An example of the obtained topography is given in Fig. 3-11. A first approximation of the subsurface flow pathways was constructed by subtracting the depth to the first continuous restricting layer from the surface elevation. The Arc/Info GIS hydrologic modeling tools FLOWDIRECTION and FLOWACCUMULATION were applied to a raster grid of the elevation-corrected subsurface topography to determine potential flow pathways (Fig. 3-12). The FLOWDIRECTION routine provided a grid of flow directions from one cell to its steepest downslope neighbor, while FLOWACCUMULATION determined the accumulated water from all cells that flowed into a particular downslope cell.

The location of the restrictive layer was verified using multisensor capacitance probes installed at the blocks using a 2-m GPR survey, remote sensing imagery and a yield map (Gish et al., 2004, 2005). Sensors above the restrictive layer demonstrated the accumulation of water above the layer Gish et al., 2002). Patterns of high crop density during water limited growing seasons were observed with remote sensing imagery using the Airborne Imaging Spectroradiometer for Applications (AISA) for areas corresponding to the GPR-identified subsurface flow pathways that could accumulate limited subsurface water at the site (Gish et al., 2004). During mildly dry years, corn yields decreased significantly ($P<0.01$) as the distance from the pathways decreased (Gish et al., 2004).

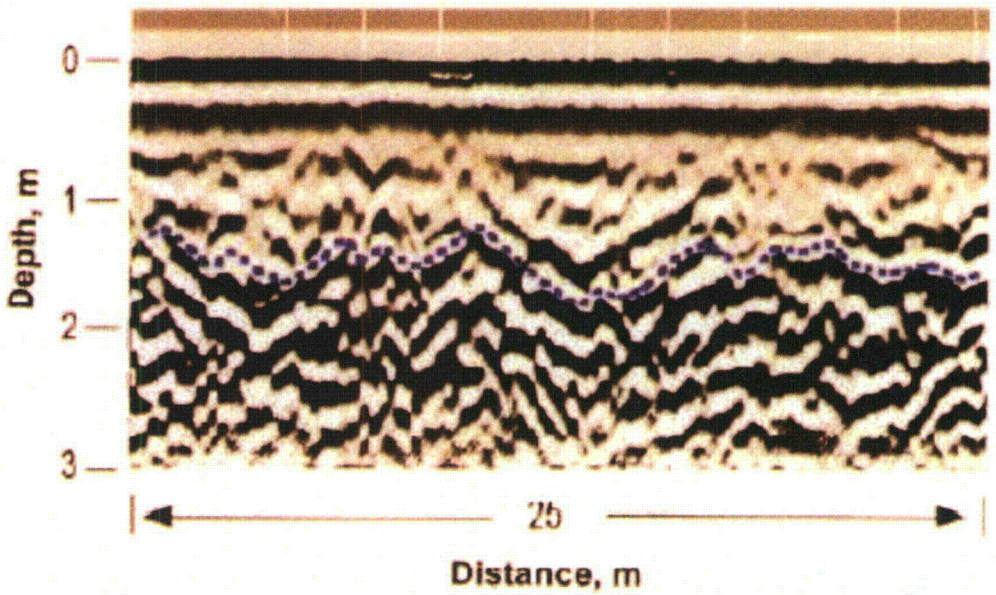

Figure 3-10. Ground-penetrating radar image with a digital trace of the first restricting layer, indicated by the dotted line (after Gish et al., 2002. Permission to use this copyrighted material is granted by Soil Science Society of America Journal).

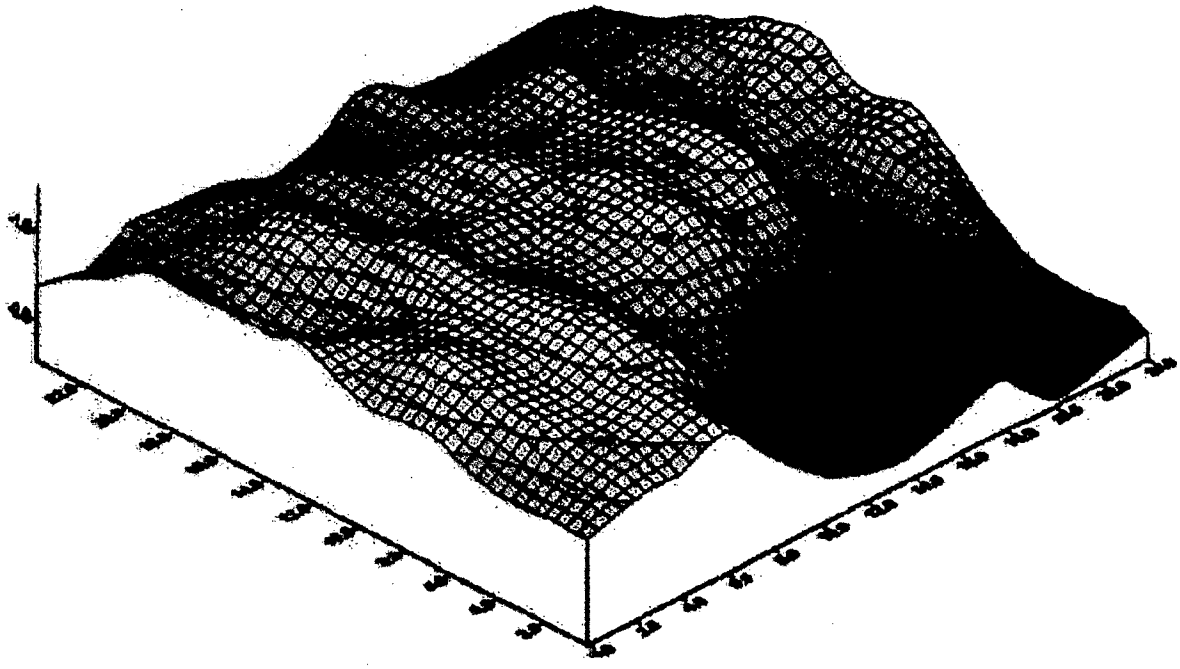

Figure 3-11. Interpolated depth to the first continuous restricting layer for Block C03. (after Gish et al., 2002. Permission to use this copyrighted material is granted by Soil Science Society of America Journal).

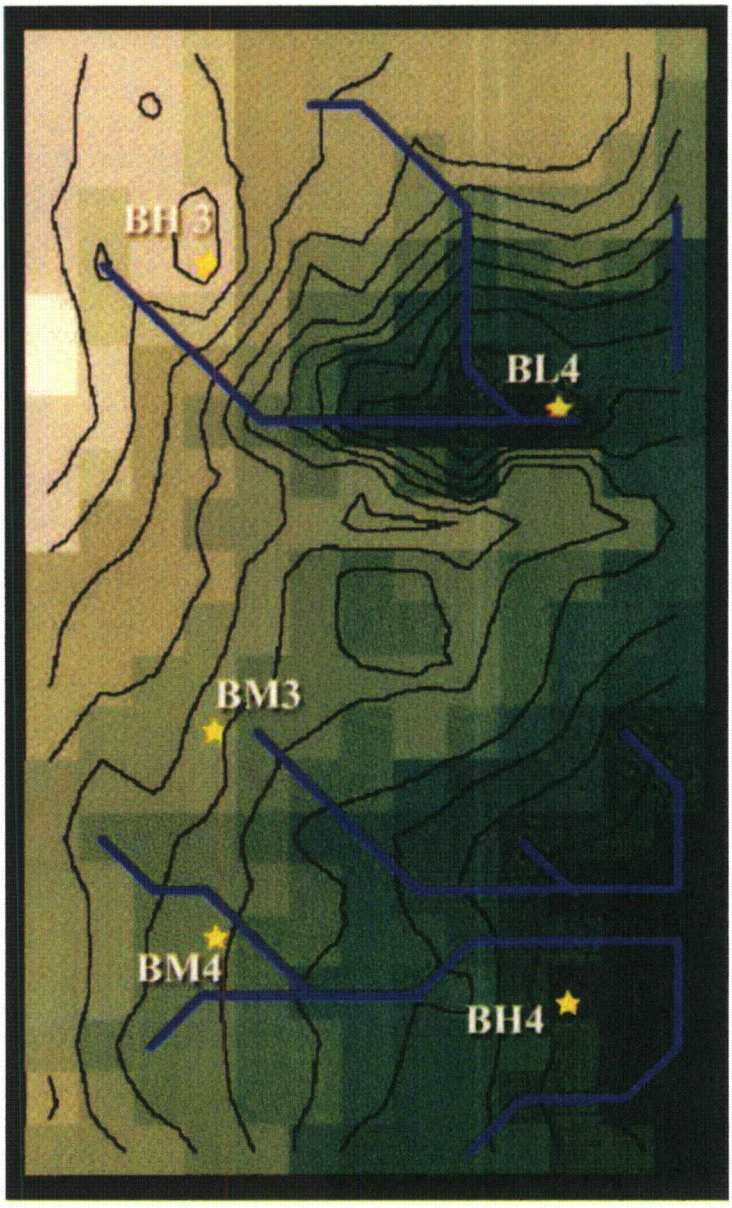

Figure 3-12. Potential subsurface flow pathways (blue lines) identified with Arc/Info hydrologic tools (after Gish et al., 2002. Permission to use this copyrighted material is granted by Soil Science Society of America Journal).

3.2.2.2.2 SOIL COVER STRUCTURAL UNITS

The multi-sensor capacitance probe (MCP) network at the site revealed the existence of areas where the soil was either consistently wetter or consistently dryer than the average of the study area. The different areas defined large spatial structural units in the top part of the vadose zone constituting the soil cover of the site. There was a noticeable similarity in the soil water storage time series measured at different locations (Fig. 3-13). Time series from different locations appeared to be vertically shifted relative to each other. Such temporal stability of soil water storage can be used to select monitoring sites and estimate missing data as shown by Guber et al. (2007).

The dense spatial coverage provided by remote sensing and yield mapping supported the existence of a spatial organization in soil cover at the site. Differences in soil water retention and hydraulic conductivity manifested themselves in either by spatially different biomass values or yield variability, or both. Areas that produced low corn yields in 2001 (e.g., BL4, BM2, BH3 and BM3 in Fig. 3-14) supposedly experienced either more intensive water logging or higher soil water losses to infiltration and/or evapotranspiration as compared to other locations. The spatial organization can be seen in Fig. 3-15, which shows an infrared image of corn biomass, superimposed on adjusted corn yields for 1999 (having a relatively dry growing season). Yields were greater than the mean inside the black polygons and less than the mean outside the black polygons. Therefore, areas with high biomass (inside the black polygons/red colors) will likely produce higher evapotranspiration rates than the low biomass areas. Multiyear mapping of the yields supported the existence of a spatial organization in soil cover, which manifested itself differently depending upon the weather conditions in a specific year (Fig. 3-16).

We note that biophysics-based spatial units are in most cases relatively large. By comparison, contaminants are typically being released within a single unit. Still, it seems important to track such an organization since observations made for a different unit may give erroneous values of the infiltration and groundwater recharge rates, i.e., those variables that drive contaminant transport in the vadose zone.

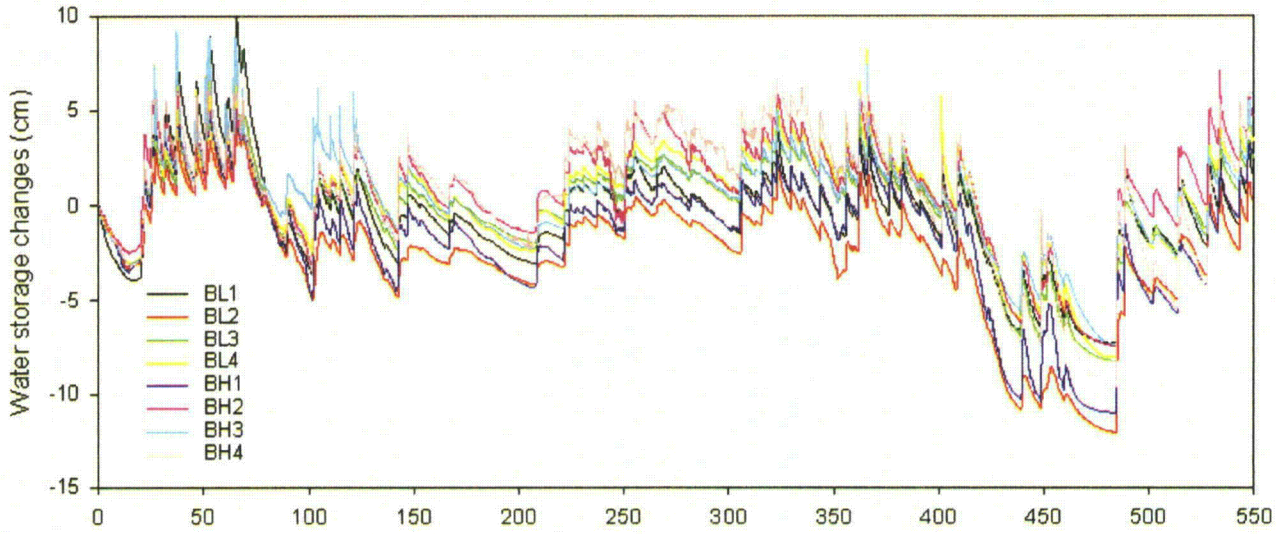

Figure 3-13. Changes in soil water storage of the 0-80 cm soil layer during the period of observations.

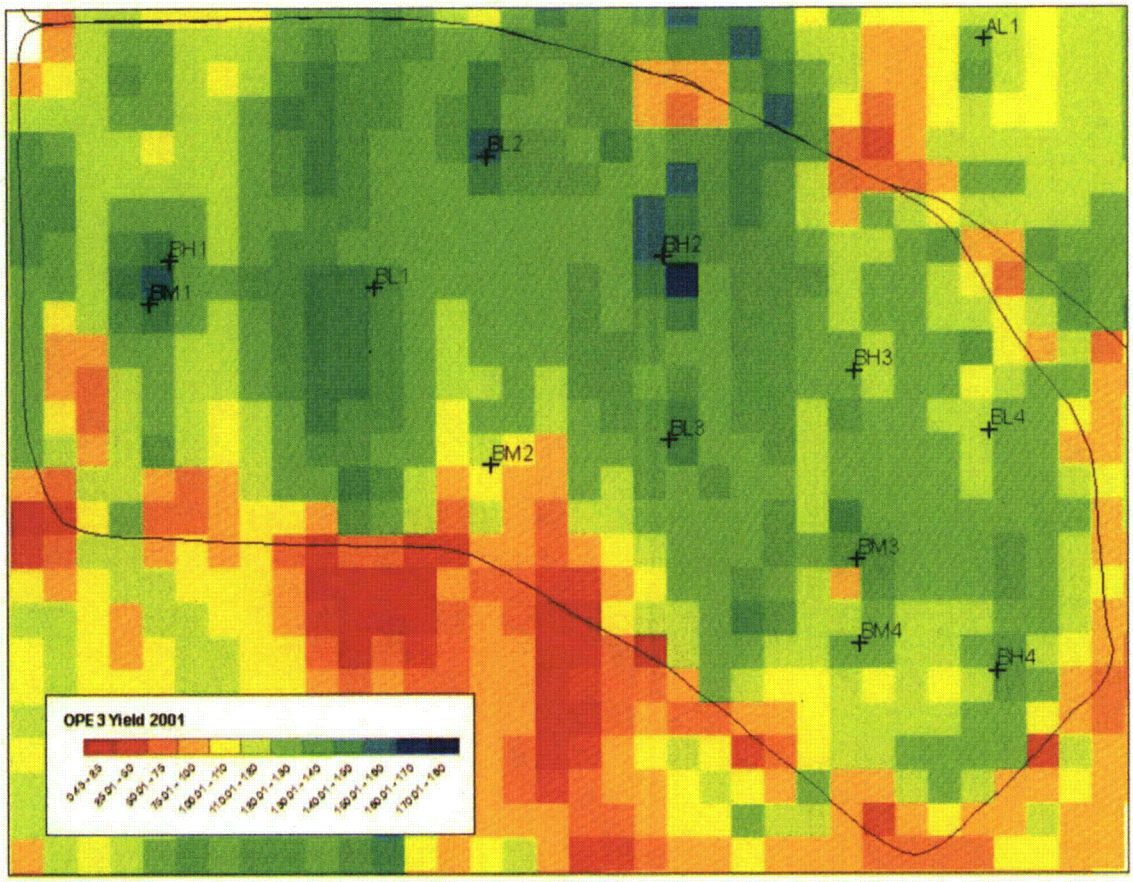

Figure 3-14. Spatial distribution of 2001 corn yields in field B. The red to yellow colors represent low corn yield areas and the dark blue colors high corn yield areas.

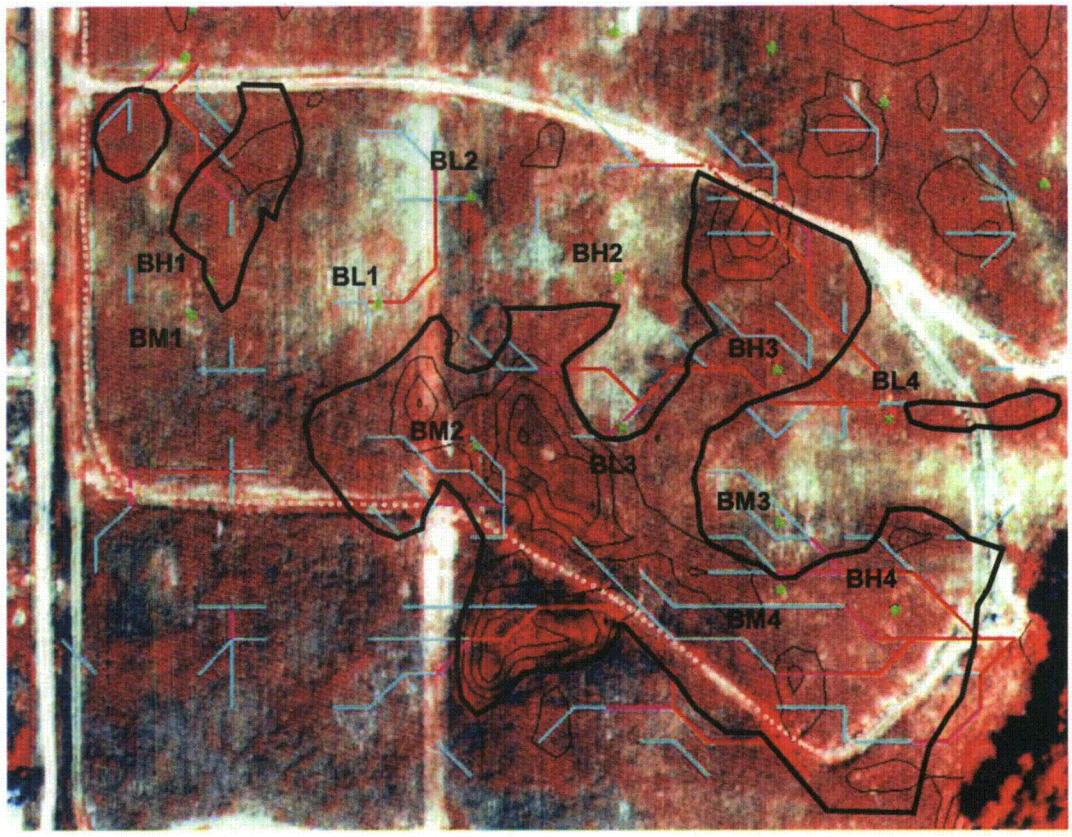

Figure 3-15. Corn yields and color infrared image of corn biomass taken in August 1999 (in a relatively dry growing season). Green stars designate moisture probe locations, while the red, pink and light blue lines designate subsurface flow pathway locations. The red color indicates regions with high biomass and the white regions low biomass, each reflecting extremes in the vegetative cycle of the corn plant. Corn grain yields greater than the mean are inside the black polygons, whereas areas outside the black polygons denote regions with yields below the mean.

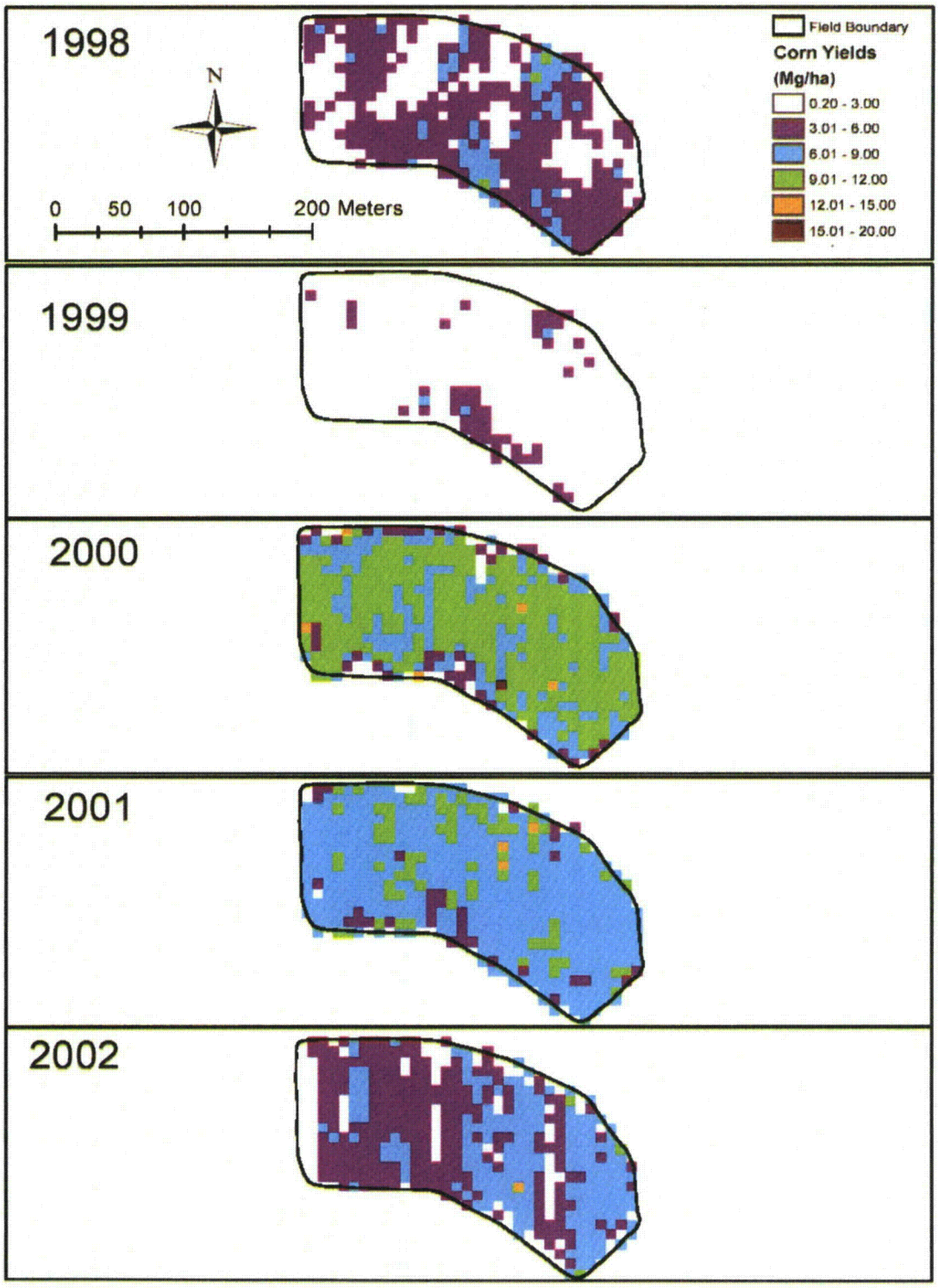

Figure 3-16. Spatial corn yield variation from 1998 to 2002. Note that 1998 and 1999 were relatively dry, 2000 was wetter than normal, 2001 was close to normal, and 2002 was dry.

3.2.3 SURVEYING, MONITORING AND PRELIMINARY MODELING TO DESIGN SITE-SPECIFIC FLOW AND TRANSPORT EXPERIMENTS

The experiments as outlined in Section 3.1 envisaged tracer applications and monitoring in areas of 10x10 to 20x20 m^2. However, the OPE3 site had been surveyed in the past mostly at a much coarser scale. The flux measurement experiment used a location where more detailed surveys had been carried out in previous years.

An additional set of measurements was made for selection and characterization of the lateral flow experiment. We decided to use for this experiment the intensively equipped South-Eastern part of Field B. Having a large number of groundwater wells (W18, 19, 20, 22, 23, 24, 25, 26, 36, 37, and 38) in this area was a major argument for selecting this location. However, the area had not been characterized at the fine scale during the ground penetration radar survey described in section 3.2.2.2.1. Therefore, an additional fine-scale ground penetration radar survey was conducted, thus allowing selection of the 30x30 m^2 site as described in the next section.

3.2.3.1 FINE-SCALE GROUND PENETRATION RADAR SURVEY

A fine-scale GPR survey was conducted in April 2006 to obtain detailed information about the topography of the restrictive soil layer and the spatial structure of subsurface preferential pathways. An area of 16,617 m^2 in the South-Eastern part of the Field B (Fig. 3-17) was surveyed with a subsurface interface radar system-2 (Geophysical Survey System, Inc., North Salem, NH). Ground-penetrating radar data were acquired for the entire site along parallel east-west transects 2-m apart. The GEO-EAS (EPA, Las Vegas, NV) and GS (Gamma Design Software, Plainwell, MI) geostatistical software packages were used to determine the spatial autocorrelation of the depth to the first continuous restricting layer. These two programs were used to produce omnidirectional semivariograms from point data derived from digitized traces (i.e., depth to the first continuous restricting layer and the associated geographic coordinates). Semivariogram models, which were fit using a least-squares approach, provided the necessary kriging parameters (i.e., nugget, range, and sill) for subsequent spatial interpolations. As a result, contour and three-dimensional surface maps of the depth to the first continuous restricting layer were produced. Results of the survey showed high spatial variability in the depth of the restrictive layer (Fig. 3-17). The depth varied within a range from 0.3 to 4.0 m, and did not correlate with the elevation of the soil surface.

As before, the ArcGIS 9.3 hydrologic modeling tools FLOWDIRECTION and FLOWACCUMULATION were applied to a raster grid of the elevation-corrected subsurface topography to determine potential flow pathways. The fine resolution used in the new survey revealed smaller branches in the subsurface flow network, although the new subsurface flow pathways resembled in general the pathways identified in the 1999 survey. Four main subsurface pathways were detected, all with a flow direction from West to East (Fig. 3-17). This direction corresponded in general to the mean surface slope direction.

3.2.3.2 LOCATION SELECTION AND SITE INSTRUMENTATION

The location for the experimental site was selected to meet the following specific conditions:
(a) The experimental area must be large enough to show spatial variability in soil properties;
(b) The size of the irrigation plot should be reasonable for both a short-duration tracer application and a continuous uniform irrigation lasting several months;

(c) The number of observation wells, and their spacing, should be large enough to reduce the influence of neighboring wells, while still capturing subsurface preferential fluxes within reasonable time intervals;
(d) The site should exclude transit runoff and subsurface preferential pathways;
(e) The site should not interfere with other ongoing long-term studies.

An experimental 10x10 m^2 site was selected in the intensively equipped South-Eastern part of Field B. Ground penetration radar data of this site indicated considerable variability in the depth to the restrictive soil layer (varying between 0.5 to 4.0 m), which was highest within the surveyed site (Fig. 3-17). Two large branches of preferential subsurface pathways as identified by GPR survey started in this area, which potentially could be used for the field tracer experiment. The beginning of the main preferential surface flow pathway was found along the Southern boundary of the site on May 11 2006 after intensive rainfall. This suggests that preferential runoff would not affect the tracer study at the selected plot. Analysis of multi-sensor capacitance probe (MCP) monitoring data at locations BM2, BM3, BM4, BL3 and BH3 showed high spatial variability in water content at different depths. The site was located 30 m from a nearby road, which did not interfere with the long-term ongoing studies at Field B.

Four plots (l-1, l-2, l-3 and l-4), each of 1 m^2 and 10 m apart, were instrumented in the spring of 2006 to monitor soil water contents, pressure heads, and groundwater depths (Fig. 3-18). MCPs (EnviroSCAN, SENTEK Pty Ltd., South Australia) and soil tensiometers were installed at depths from 0.1 to 1.0 m at 0.1 m increments to monitor soil water content and pressure heads, respectively (Fig. 3-19). The MCP and tensiometers were connected to a CR-10X datalogger (Campbell Scientific, Inc., Logan, Utah) to collect data every 15 minutes. Two AM416 Relay Multiplexers (Campbell Scientific, Inc., Logan, Utah) controlled datalogger communication with 40 pressure transducers (PX26-005GV, Omega, Stanford, CT) installed in tensiometers. Collected data were acquired from the Redwing 100 Airlink modem (Campbell Scientific, Inc., Logan, Utah) once a week (Fig. 3-19). Five additional locations 7 m downgradient from the site, as well as three locations 14 m downgradient, were equipped with observation wells and MCPs for monitoring water contents and groundwater depths (Fig. 3-20). Groundwater depths were measured at each location using Cera-Diver (Van Essen Instruments, Delft, The Netherlands) sensors installed in wells at a depth of 2.0 m. Barometric pressures were recorded using a Baro-Diver sensor (Van Essen Instruments, Delft, the Netherlands). Volumetric water contents were measured periodically at locations l-1 to l-4 to correct MCP factory calibration (see Appendix B).

A drainage line was constructed at distance of 1-m to the South and 1 m to the East of the plot boundary to collect runoff water. A ½' H-type flume was installed at the outlet of the drainage line and equipped with a 75 kHz Ultrasonic sensor connected to a Sigma 980 Flow meter (Hach Company, Loveland, CO) for continuous water level measurements.

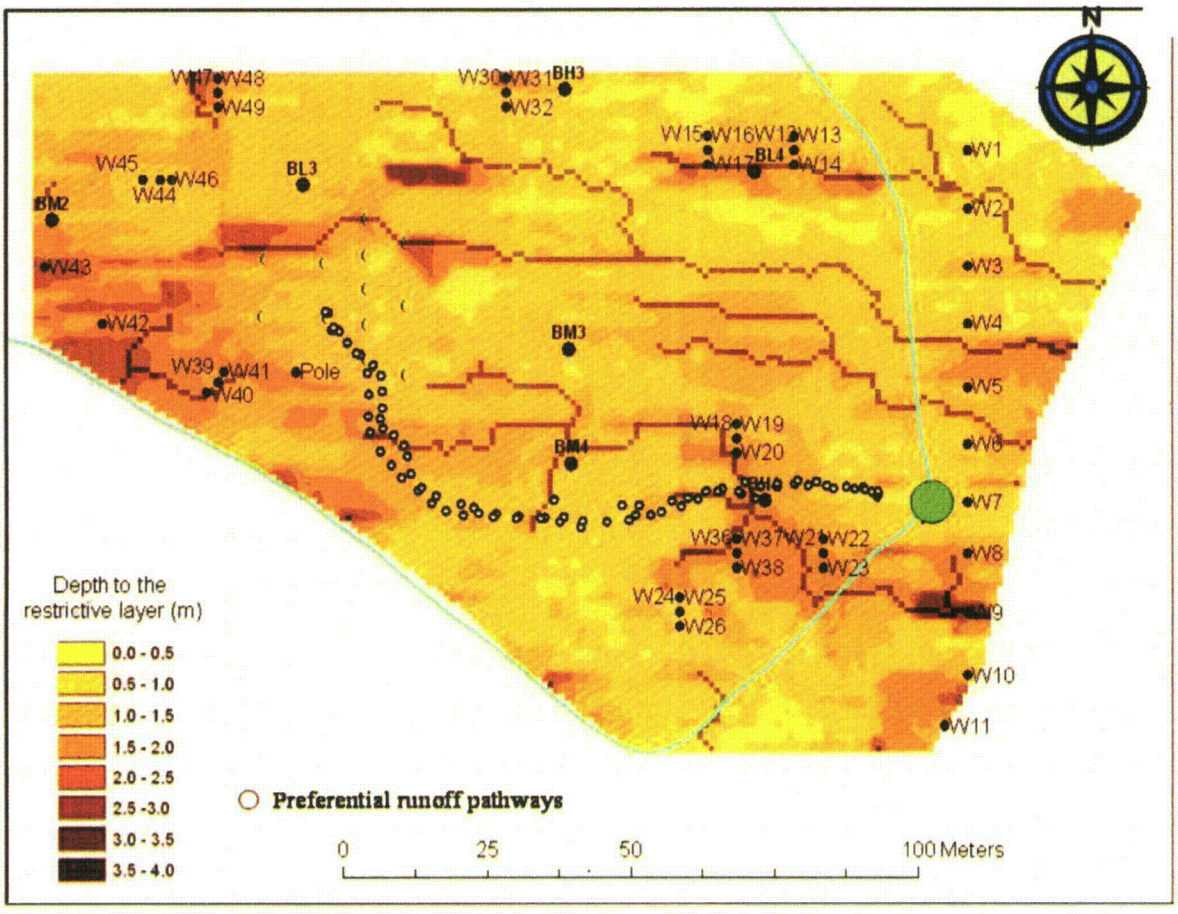

Figure 3-17. Depth to the restrictive layer, subsurface flow pathways (brown polylines), locations of existing multi-sensor capacitance probes ( ), groundwater observation wells ( ), and runoff flume ( ) in the vicinity of the lateral flow experimental site at Field B.

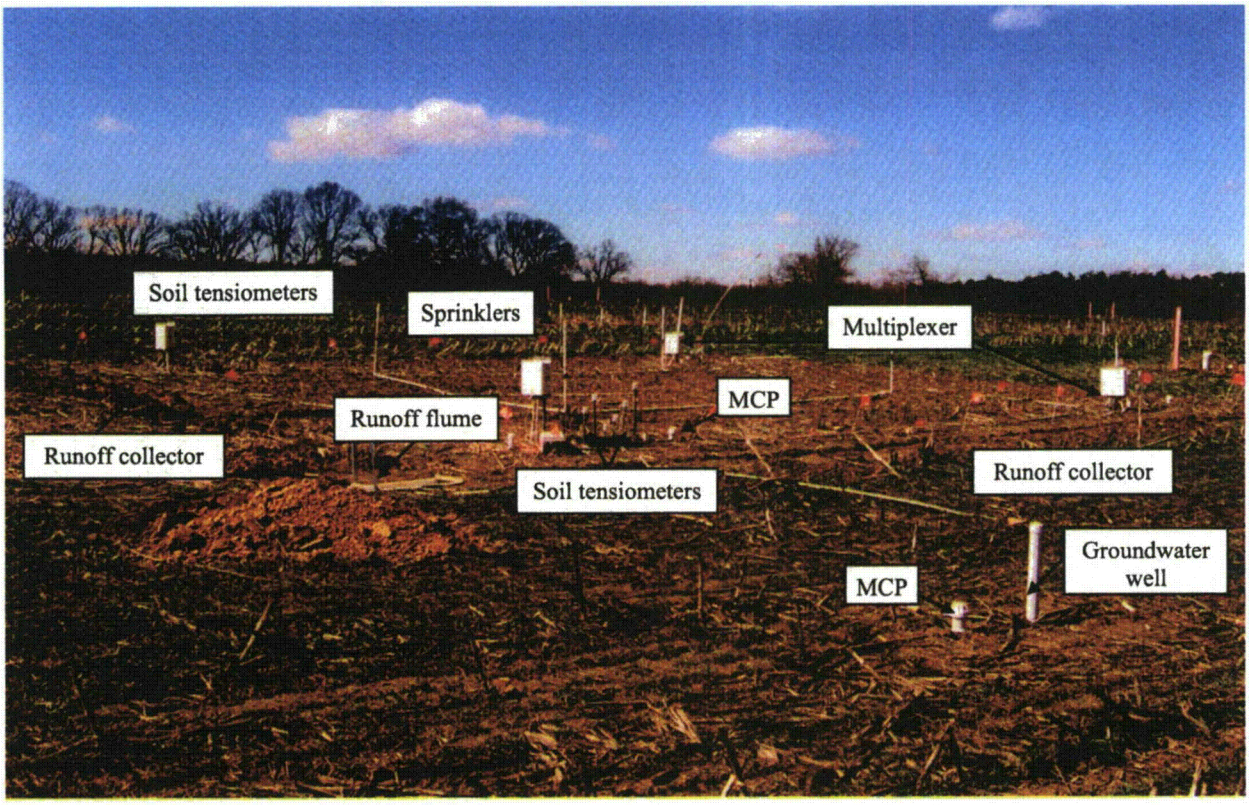

Figure 3-18 Lateral flow experimental setup.

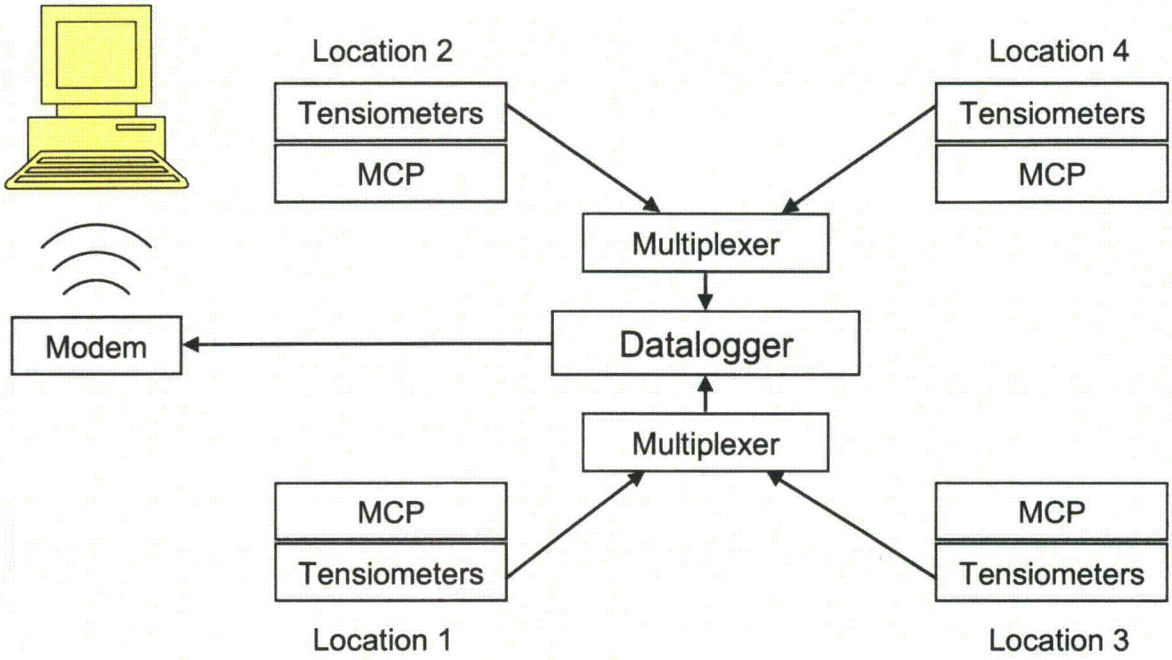

Figure 3-19. Schematic of the data acquisition and collection system.

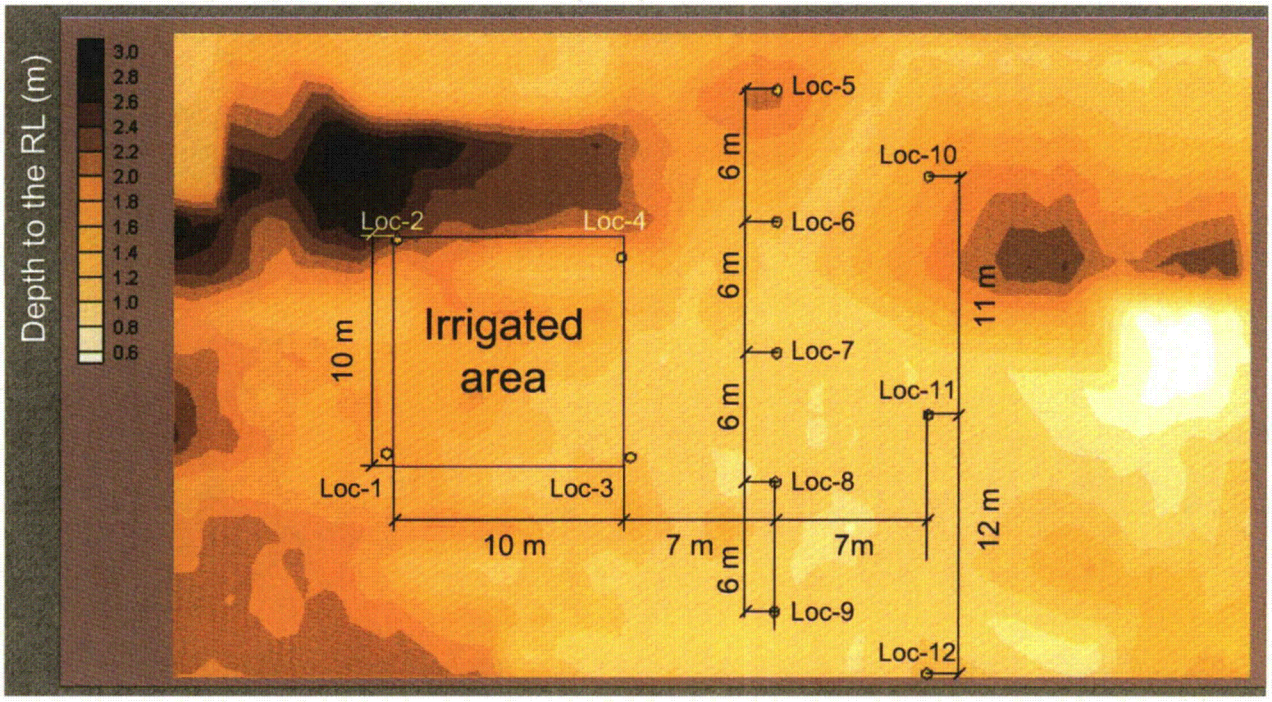

Figure 3-20. Locations of multi-sensor capacitance probes and groundwater wells at the experimental plot

3.2.3.3 BASIC SOIL PROPERTIES AT THE LATERAL FLOW EXPERIMENTAL SITE

Soil samples were taken from the soil surface to a depth of 2.0 m at each location during MCP and groundwater well installation. Soil texture was measured with the pipette method (Gee and Or, 2002) after dispersion with sodium pyrophosphate $Na_4P_2O_7$. Values of soil pH were measured at a solid to liquid ratio of 1:1 (Page et al., 1982). Organic carbon content was measured in the upper 0.6-m soil layer using the dry combustion method (Page et al., 1982).

Spatial variability in soil texture was found to be surprisingly high for the relatively small site. Soil texture was represented by six textural classes within the range from sandy loam to silty clay loam (Fig. 3-21). The particle size distribution generally did not change noticeably in the upper 1.3 m of the soil profile, where sand dominated over clay and silt. A distinct decrease in sand content and an increase in silt content can be seen below 1.3-m depth (Fig. 3-22), thus indicating a gradual transition in soil texture from sandy loam to loam and then silty clay loam. The horizontal variability in soil texture was of the same order of magnitude as the vertical variability. Coefficients of variation for sand and silt content increased with depth and were in the range from 0.06 to 0.92 and from 0.15 to 0.48, respectively. One could expect much variability in the soil water content at the studied site, since spatial variability in soil texture affects substantially the soil hydraulic properties.

The organic carbon content of the upper 0.6 m of the soil profile did not vary much at each depth; values decreased gradually from 0.4-1.2 % at 0.1 m, to 0.03-0.13% at 0.6 m depth. The soil pH was highest in the upper 0.2-m soil layer; average pH values gradually decreased with the depth from 5.9 near the soil surface to 4.5 at 2.0-m depth. Coefficients of variation for pH were within the range from 0.04 to 0.10, indicating less horizontal variability in pH as compared to variability in the soil particle size distribution.

The soil bulk density was measured on undisturbed samples taken from the upper 1.0-m soil layer at 0.1-m increments during MCP calibration at location 1-4. The bulk density generally increased with depth from 1.3-1.6 to 1.6-1.9 g cm^{-3} in the upper 0.3 m of the soil profile, but did not change noticeably with depth in deeper layers (Fig. 3-23). Coefficients of variation for the bulk density were in the range of 0.05 to 0.09 at different depths, and did not correlate with average soil bulk density values and/or sampling depths.

Soil hydraulic properties were measured on undisturbed soil samples (5 cm ID, 5.1 cm height) taken from depths of 0 to 1.0 m in 0.1 m increments at locations 1, 2, 3, and 4. Soil samples were gradually saturated from the bottom. A constant head soil core method (Reynolds and Elrick, 2002) with a water head of 0.5 m was used to measure the saturated hydraulic conductivity of the soil samples. The samples subsequently were placed into 1400 Tempe pressure cells (Soil Moisture Equipment Corp., Santa Barbara, CA) to measure soil water retention as described by Dane and Hopmans (2002). Results of the soil hydraulic properties measurements are presented in Figs. 3-24 and 3-25.

Measured saturated hydraulic conductivities (K_{sat}) varied greatly vertically and laterally; they were mostly in the range from 0.003 to 27.1 cm d^{-1}. Generally smaller values were obtained at locations 1 and 3 compared to locations 2 and 4 (Fig. 3-24). Soil samples taken from depths of 0.2-0.4 m at location 1 and from depths of 0.12-0.40 m and below 0.8-m at location 3 did not conduct water at 0.5 m pressure head. Low K_{sat} values measured on 5-cm diameter samples presumably characterized the hydraulic conductivity of the soil matrix, while higher values could be measured on large undisturbed soil samples.

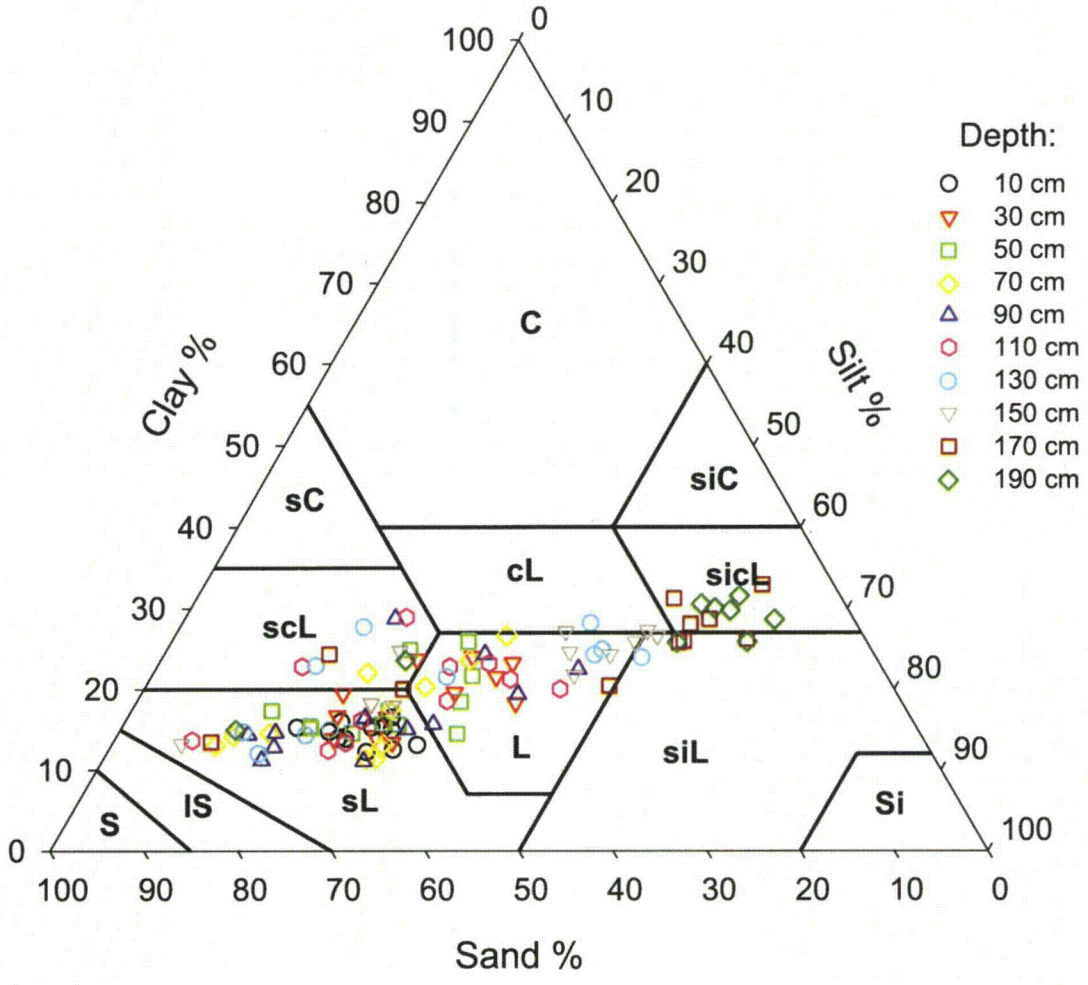

Figure 3-21. Soil texture measured at 10 depths in 12 locations.

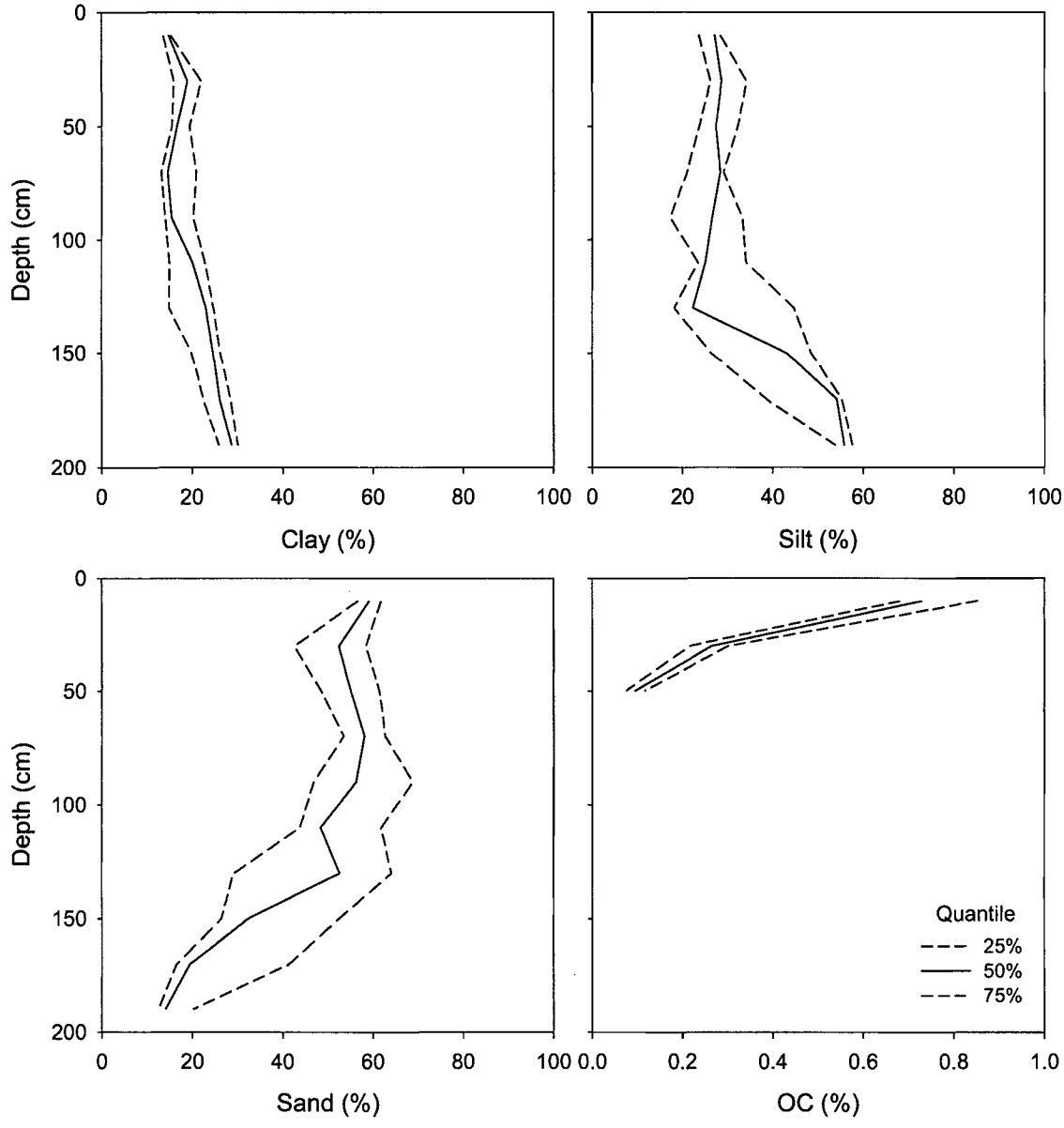

Figure 3-22. Measured clay, silt, sand and organic carbon distributions in the soil profiles.

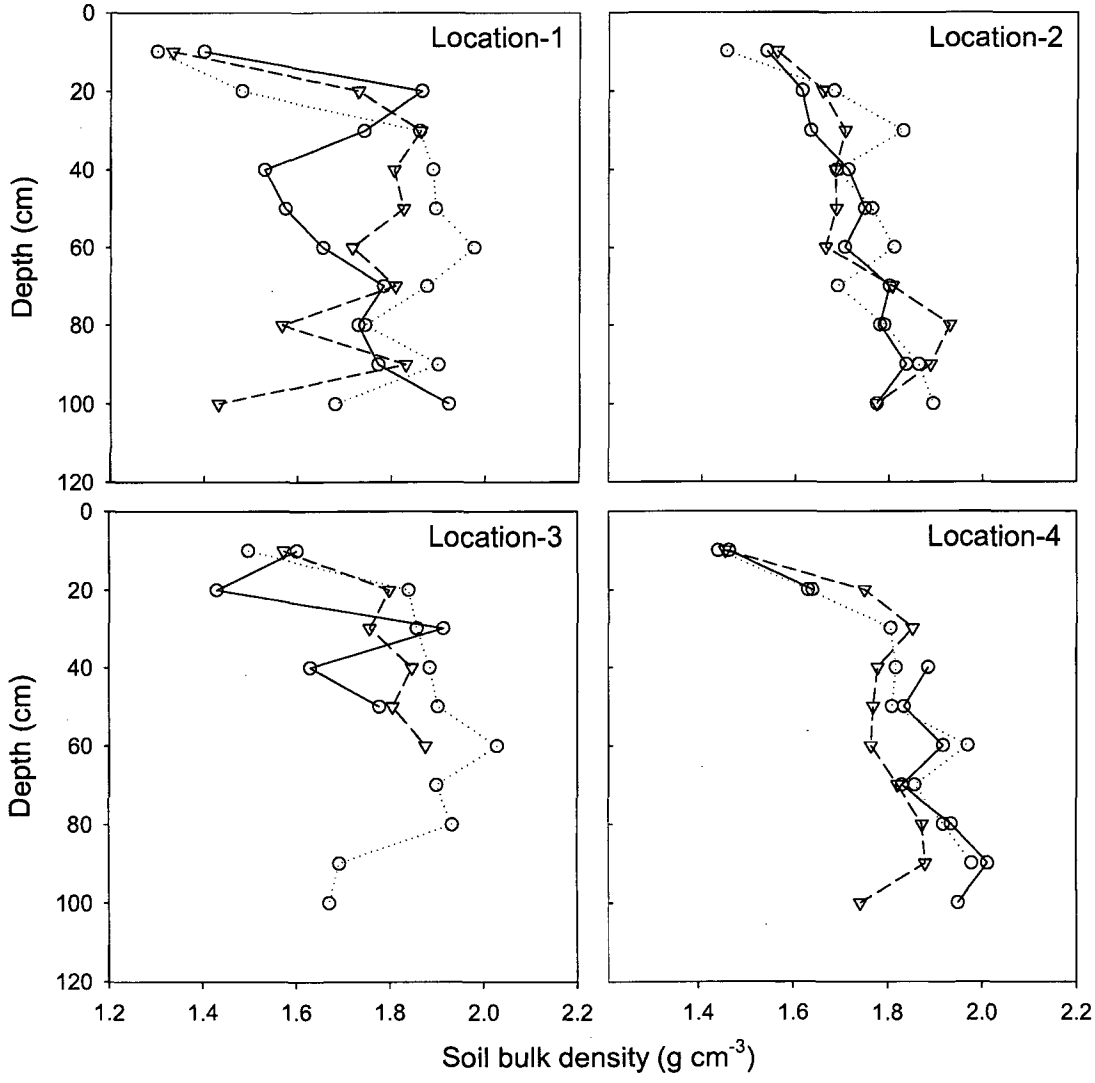

Figure 3-23. Measured soil bulk density distributions versus depth at locations 1 through 4.

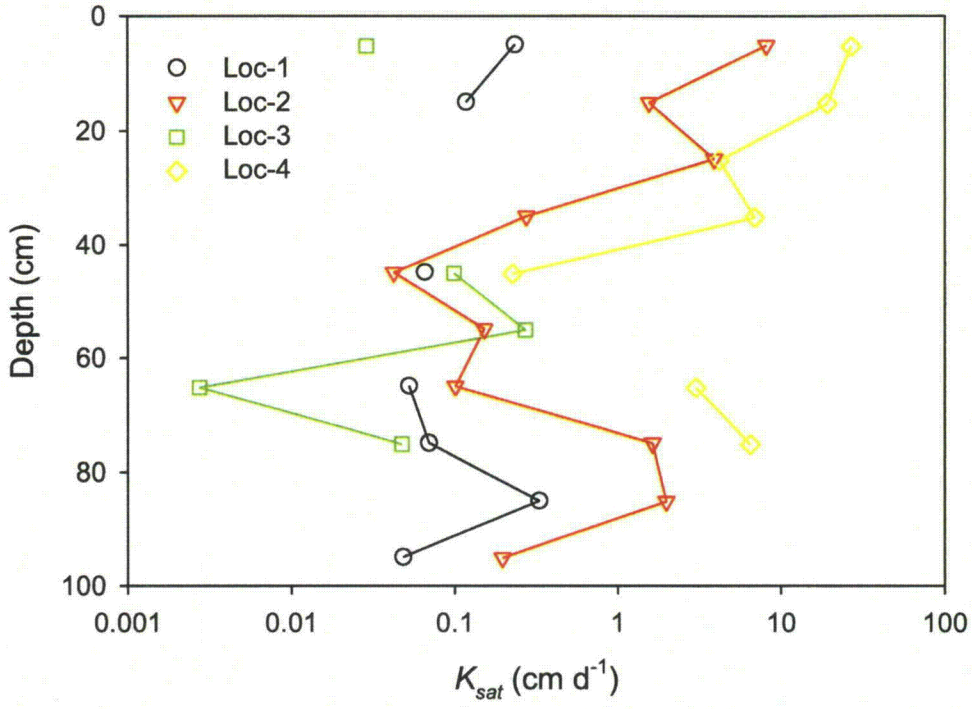

Figure 3-24. Laboratory measured saturated hydraulic conductivities, K_{sat}.

Soil water retention was found to vary with depths. Generally, the saturated water content decreased and the slope of the water retention curve increased with depth. We did not observe high lateral variability in soil water retention, except for the 30-40 cm soil layer (Fig. 3-25), where the variability could be attributed to high variability in the bulk density (Fig. 3-23). Summarizing the basic soil properties, one could expect considerable variability in the spatial and temporal patterns of the soil water content during the experiments, primarily because of high spatial variability in the saturated hydraulic conductivity.

3.2.3.4 SOIL ELECTRICAL RESISTIVITY SURVEY

Soil electrical resistivity measurements have recently gained popularity as an expedient method for studying the spatial and temporal variability of many soil physical properties (i.e., soil structure, water content, or fluid composition). Because the method is non-destructive and very sensitive, it offers a very attractive tool for describing the subsurface properties without excavating. Soil electrical resistivity measurements have already been used in many applications, such as: groundwater exploration, landfill and solute transfer delineations, agronomic management by identifying areas of excessive compaction, soil horizonization or depths to bedrock, and assessing the soil hydraulic properties (Samouëlian et al., 2005). In this study we used resistivity measurements as a monitoring tool to evaluate the degree of soil heterogeneity based on soil water content distributions.

Water content distributions in the vadose zone were studied after the tracer experiment. The apparent soil electrical resistivity of 2-m soil layers was measured 7 times when the soil water contents differed substantially. Soil temperature was measured at locations 6 and 8 at depths from 0.1 to 1.0 m using 0.1 m increments.

A preliminary study was conducted to obtain a relationship between the volumetric water content (θ) and the soil electrical resistivity (ER). Disturbed soil samples for this purpose were taken immediately after the lateral tracer experiment at 12 locations in close proximity (approximately 0.5 m) to the MCPs at depths of 0-2.0 m in 0.2 m increments, and used for the soil water content and ER measurements. The electrical resistivity was measured at the field water content using LandMapper ERM-2 (Landviser, LLC, League City, TX) in 4-electrode cells (9.6 cm length, 2.7 cm width, 2.3 cm height) especially designed for this experiment (Fig. 3-26) at a temperature of 22°C. Results were plotted as pairs (θ, ER) measured for samples from different depths (Fig. 3-27). Generally ER decreased and approached a minimum faster with an increase in water content at depths of 10 and 30 cm, than at deeper soil layers.

A regression tree algorithm (Venables and Ripley, 1996; S-PLUS 2000 Software) was used to identify soil parameters affecting the ER-water content relationships. To reduce the effect of soil structure on splitting variables, the dataset was subdivided into two datasets referred as topsoil (0-40 cm where soil structure could be affected by the root activity from previous years and by relatively high organic matter contents) and subsoil (40-200 cm) layers. The regression tree technique was applied to the two datasets separately. Soil bulk density (BD), and silt and clay content were found to be influential parameters for the topsoil, whereas BD and sand content were the influential parameters for the subsoil layer. A power function was fitted to the measured pairs (θ, ER) separately for each layer as follows:

$$ER = a\theta^{-b} \qquad (3\text{-}1)$$

where a and b are empirical parameters defined in terms of linear regressions of soil bulk density and/or the percentage of the soil textural fraction affecting the ER- θ relationship

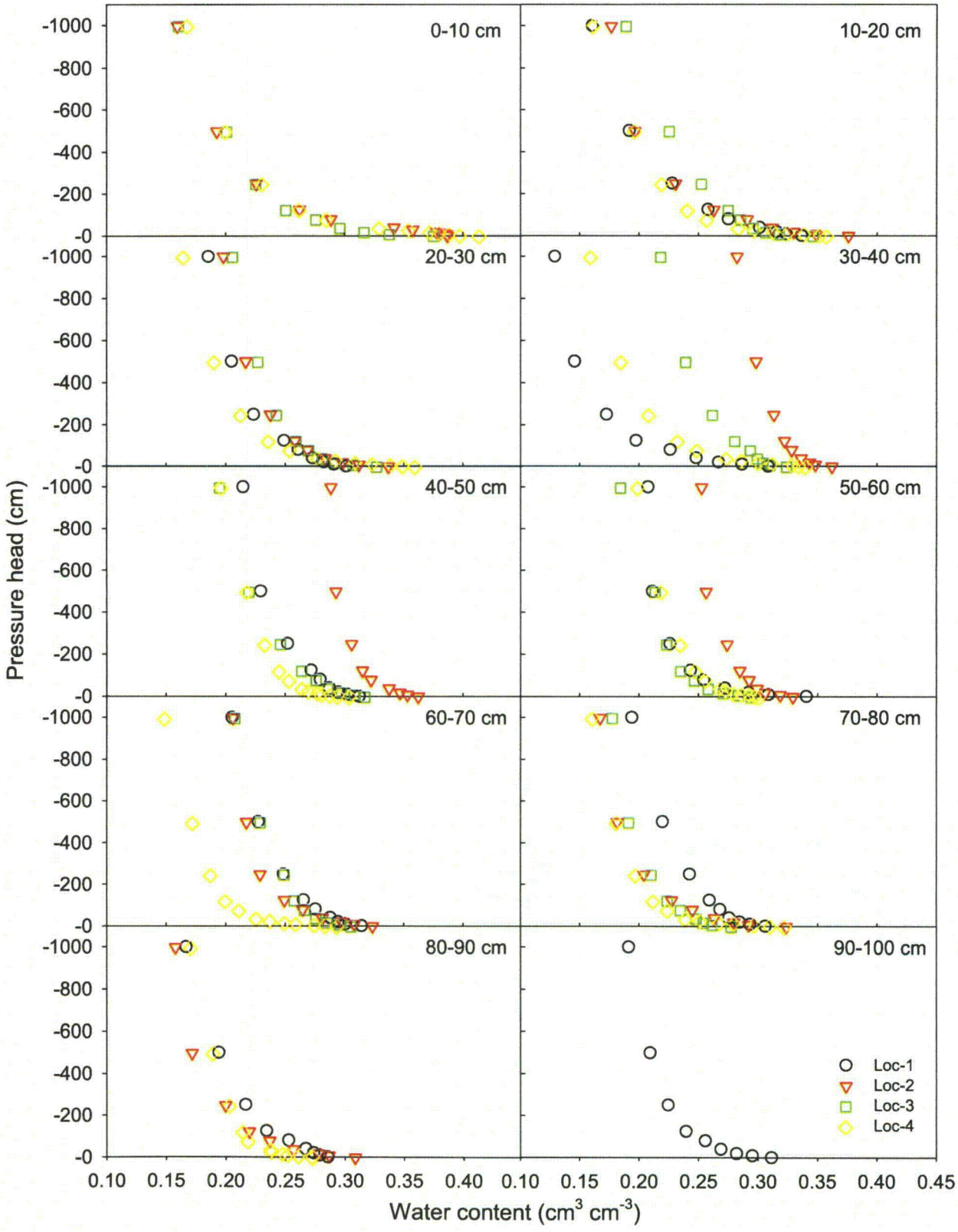

Figure 3-25. Laboratory-measured soil water retention curves.

Figure 3-26. Laboratory (left) and field (right) setups to measure soil electrical resistivity.

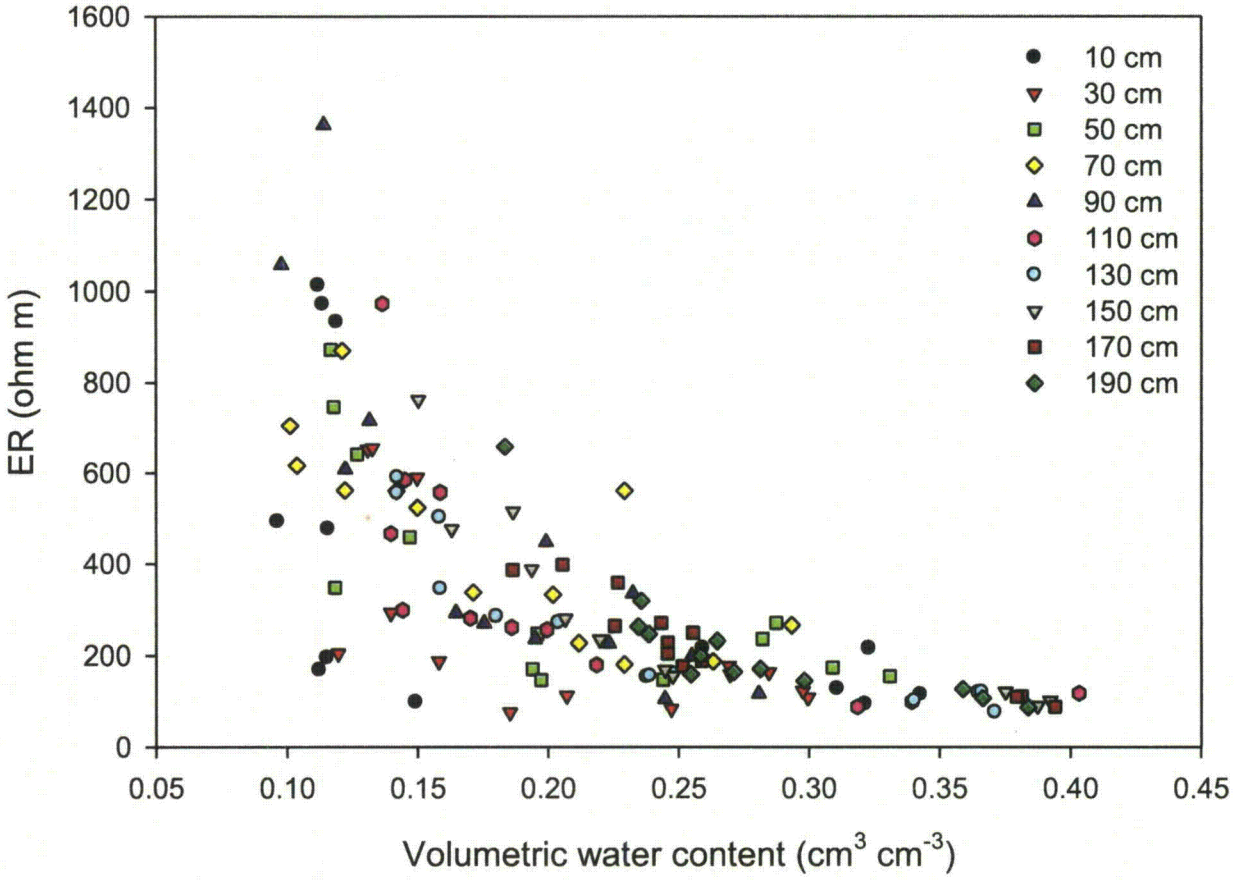

Figure 3-27. Relationship between volumetric soil water content and electrical resistivity measured on samples taken from 10 depths at 12 locations.

The fitted parameters were:

topsoil (0 – 40 cm)	subsoil (40 – 200 cm)	
$a = 977.0 - 25.1 \cdot \text{Clay} - 237.6 \cdot \text{BD}$	$a = 32.2 + 0.176 \cdot \text{Sand}$	(3-2)
$b = 0.316 + 12.5 \cdot \text{Clay} - 3.97 \cdot \text{Silt}$	$b = 2.58 - 0.920 \cdot \text{BD}$	

Fig. 3-28 shows significant improvement in predictions of ER from the water content data when the empirical parameters a and b were calculated in this way from soil bulk density and soil texture.

To perform the field survey, 50 electrodes were manufactured from stainless steel. Electrodes were installed on the soil surface at 0.5-m increments along a transect connecting wells 5, 6, 7, and 8 (Fig. 3-20). Soil temperature profile distributions were measured at locations 6 and 8 synchronously with the ER survey using Campbell 107 Soil Temperature Probes (Campbell Scientific, Inc., Logan, Utah). Apparent ER values were calculated from ER values measured with a Wenner-Schlumberger array (Samouëlian et al., 2005), and processed using the RES2DINV software (GEOTOMO SOFTWARE SDN. BHD., Penang, Malaysia).

Soil temperature generally decreased over time at all depths, was relatively constant versus depths in October 2008, and increased with depth in November 2008 and March 2009 (Fig. 3-29). Soil temperature data were used to correct field ER values to the same standard reference temperature. We used for this an equation derived recently by Besson et al. (2008) for unsaturated soils:

$$ER_{ref} = ER\left(\frac{T_{ref}}{T}\right)^{-0.3} \qquad (3\text{-}3)$$

where ER is the field-measured electrical resistivity at temperature T, and ER_{ref} is the electrical resistivity measured in the laboratory at temperature T_{ref}=22°C.

The 2-D electrical resistivity survey was conducted twice a month during September – November 2008, as well as on March 7, 2009. Results at different times are shown in Fig. 3-30. The high spatial variability in ER observed at all times indicates considerable soil heterogeneity across the 24-m transect. Relatively high ER values were observed at depths from 0.3 to 1.0 m along the first 16 m of the transect in September – October, 2008. Both high and low ER values were observed above and below these depths. The data do not suggest the existence of strict vertical soil stratification at the study site. Although the observed resistivities showed substantial temporal fluctuations, some similarities in the ER distributions can be seen in the 2-D images of October 17, 31 and November 7, as well as of September 17 and November 21.

Once corrected for temperature, the ER values were converted into volumetric water content using equation (3-1). The parameters a and b were calculated separately for the topsoil and subsoil (eq. (3-2)) using data from locations 5-8, and with soil texture and bulk density averaged for each depth. Equation (3-1) was subsequently applied with constrains on the water content range $\theta_{min} \le \theta \le \theta_{max}$, where θ_{min} and θ_{max} are the minimum and maximum water content observed at locations 5, 6, 7, and 8 during the monitoring period.

The 2-D water content images revealed high spatial variability in the soil water content (Fig. 3-31), including distinct vertical fingers representing relatively dry soil zones. While not spatially and temporally persistent, these fingers often joined a laterally extended relatively dry layer at depths between 0.3 and 1.0 m. The formation of fingers and associated dry and wet regions implies the presence of hydraulically inactive and active zones at those locations.

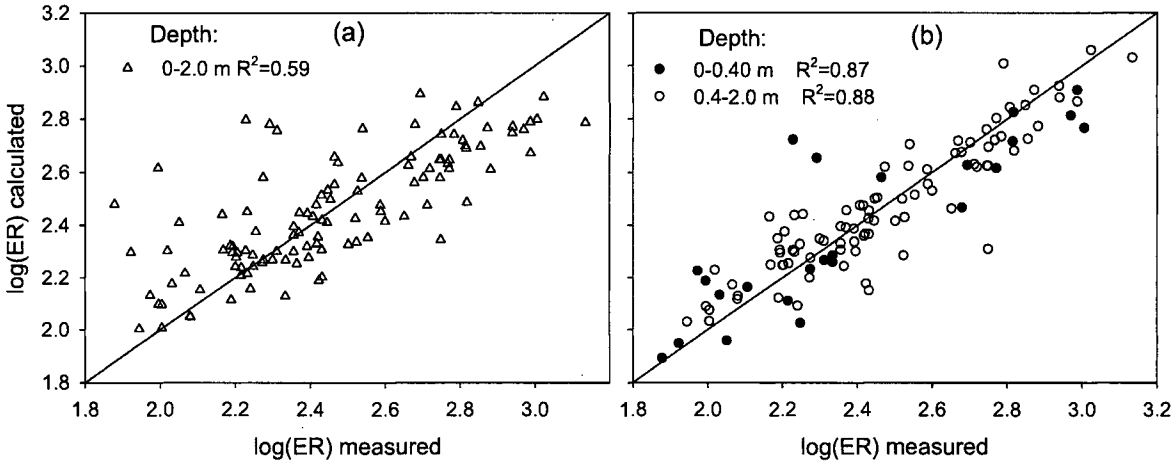

Figure 3-28. Performance of the model (Eq. 3-2) to simulate the dependence of the soil electric resistivity on soil water content. (a) model parameters do not depend on soil properties, (b) model parameters depend on soil properties.

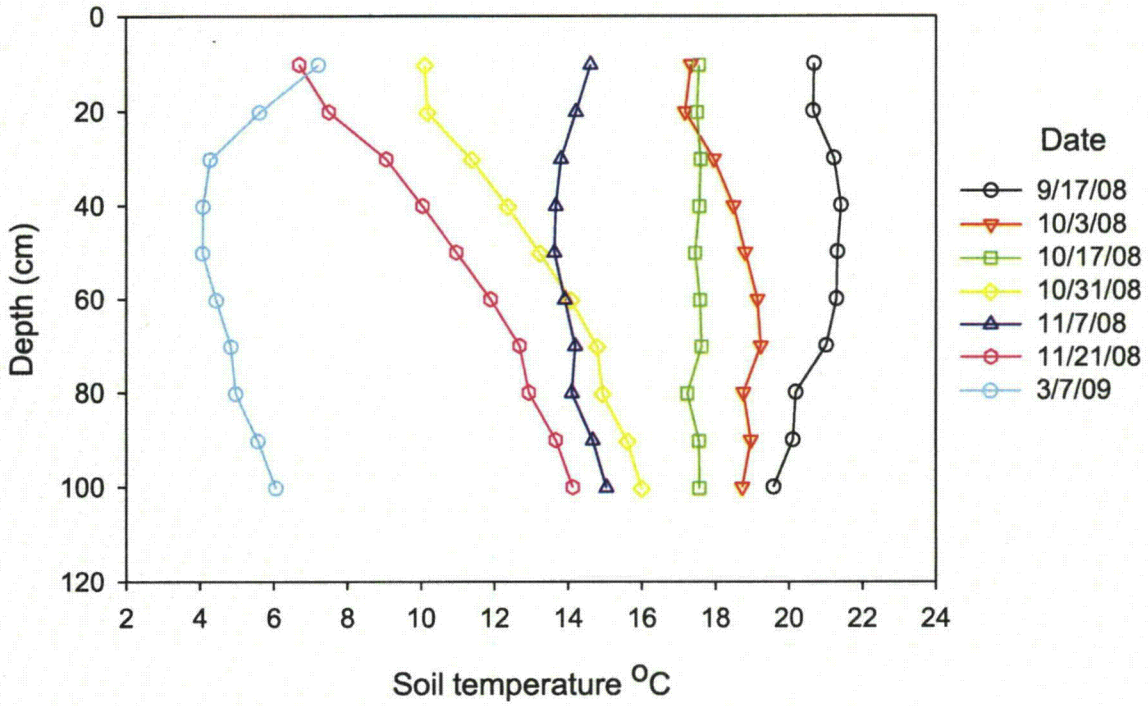

Figure 3-29. Soil profile temperature distributions measured at 7 dates at the ER measurement time. Shown are average temperatures from locations 6 and 8.

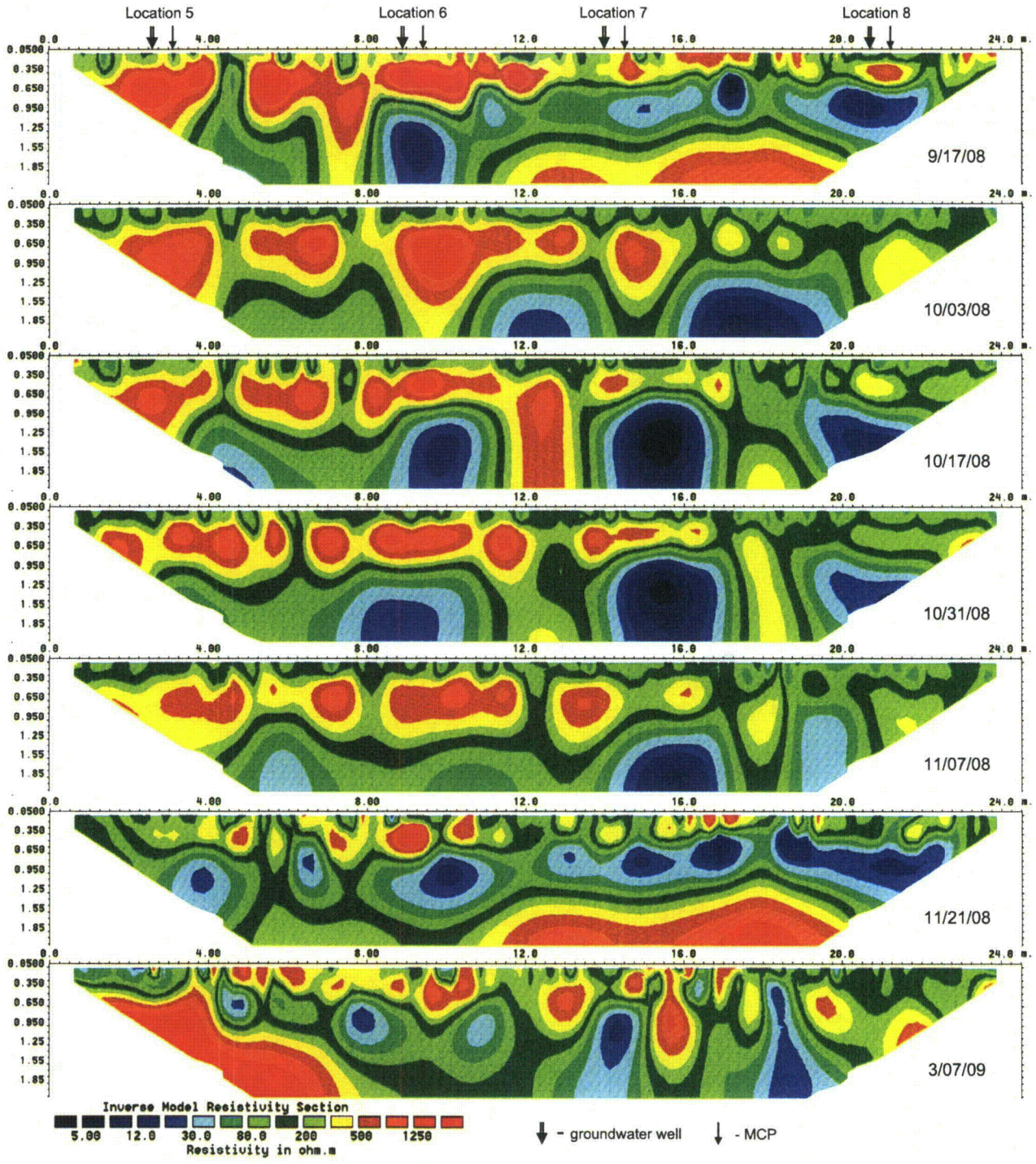

Figure 3-30. Electrical resistivity measured in a 2-m deep soil profile along a 24-m transect. Locations of groundwater wells and MCOs (multiple capacitance probes) are shown by arrows.

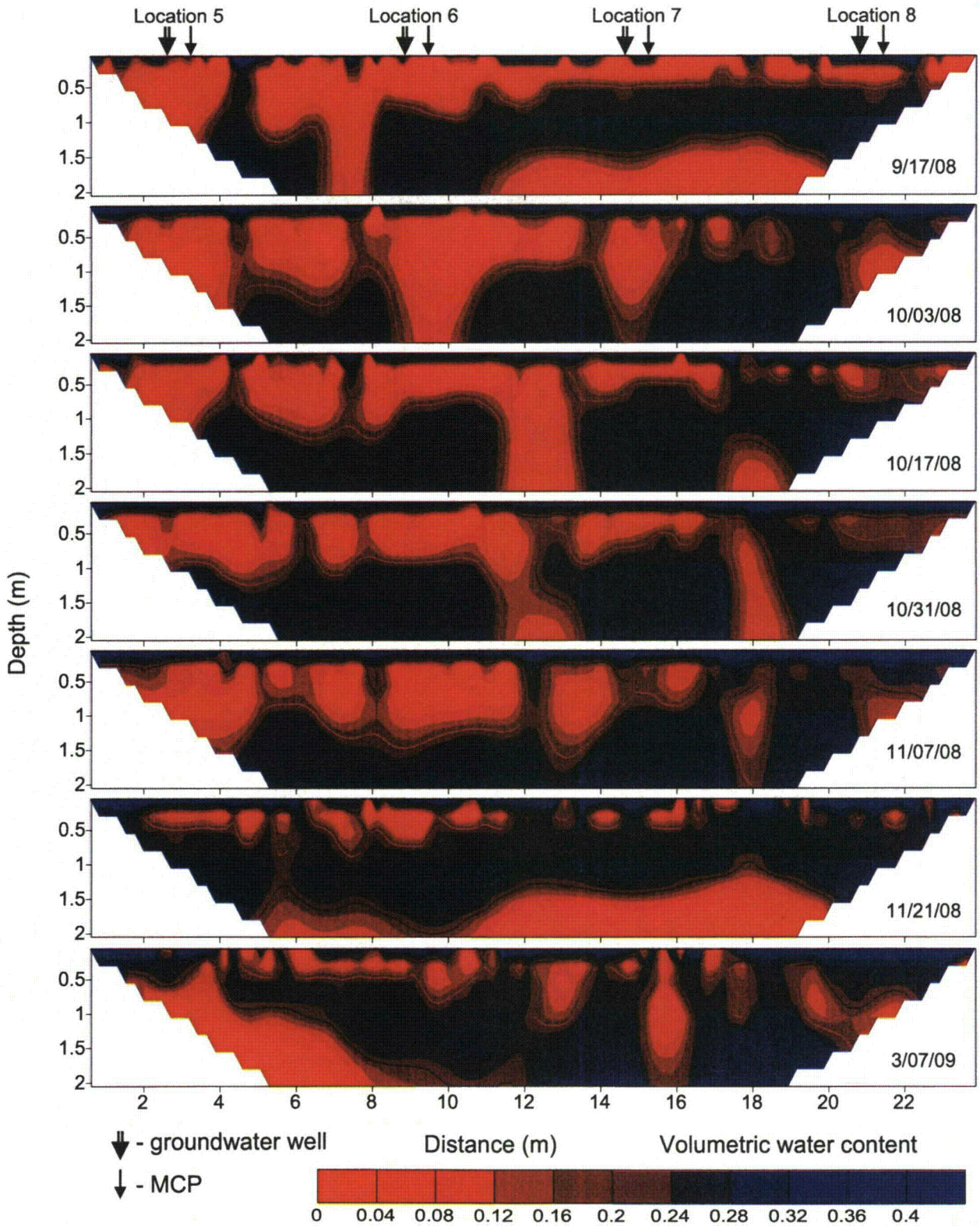

Figure 3-31. Volumetric water content distributions in a 2-m soil profile along the 24-m transect at 7 dates.

3.2.3.5 SOIL MOISTURE AND GROUNDWATER MONITORING

Soil moisture was monitored at the experimental site from July 1, 2006 through November 1, 2007. A weather station located about 80 m from the site collected meteorological data at short time intervals (10 minutes). These data included: soil temperature, soil heat flux, air temperature, relative humidity, 3-D wind speed profile, rainfall, long and short wave solar radiation, net solar radiation, saturation and actual vapor pressure, evapotranspiration, and CO_2 fluxes. Daily evapotranspiration (ET) rates were computed using the Penman-Monteith method as documented by FAO (Allen et al., 1998). The daily ET and rainfall rates were integrated over time to obtain cumulative ET and precipitation values as a function of time from the beginning of the observation period.

Monthly and cumulative ET and rainfall rates are shown in Fig. 3-32. Daily rainfall and ET values were in the range from 0 to 6.7 cm and from $5 \cdot 10^{-3}$ to 0.4 cm respectively. The total amount of precipitation was two times larger than the total ET during the observation period. The rainfall and ET distributions were not uniform over the year. Relatively high rates of precipitation were observed in the months of April, September, October and November, and low rates in June and July. Contrary to precipitation, ET values were higher in the summer and lower in the winter.

Tensiometer and MCP readings were converted to volumetric water contents and pressure heads. The MCP factory calibrations were corrected separately for topsoil and subsoil to improve the accuracy of the water content measurements (see Appendix B). Tensiometer reading exhibited noise, which was removed using a multilevel 1-D wavelet decomposition with a Daubechies filter (db4). We used the Wavelet toolbox of the MATLAB 6.5 Software for this. Depending upon data quality, the multilevel parameter in the wavelet decomposition was fixed at values between 4 and 6.

The non-uniform distribution of precipitation and ET affected the dynamics of the water content and the pressure head in the vadose zone during the experiments. Periods of deep soil drying followed rainfall events when water content almost approached saturation. Extremely low water contents were observed in September 2006, and August and October 2007 at practically all depths (Fig. 3-33). The low water contents corresponded to pressure heads close to or below the ceramic's air entry value. For this reason, tensiometers installed at depths less than 0.8 m did not work properly in August and September 2007.

Temporal changes in the soil water content varied with depth. Water contents in the topsoil (0-0.4 m) generally increased rapidly during and after the rainfall events, while relatively small changes occurred in the subsoil (0.4-1.0 m). Water contents in deeper soil layers were less sensitive to precipitation and evapotranspiration as compared to the upper layers. This was also true for the pressure head. There always was a delay in response of the deeper soil layers to change sin the flux at the soil surface.

Water contents at similar depths varied considerably among the four locations. The differences were most pronounced at depths between 20 and 50 cm, where water contents were consistently higher at locations 2 and 4 as compared to locations 1 and 3. Consistently low water contents were observed at a depth of 70 cm at location 2 during the whole monitoring period.

Spatial differences in soil water content dynamics were reflected by different field soil water retention curves, obtained by plotting field-measured pressure heads versus water contents for 6 depths at 4 locations (Fig. 3-34). We present here only data measured during continuous soil drying (drainage water retention curves). The data in Fig. 3-34 in general resembled the laboratory-measured water retention curves (Fig. 3-25). Similarly as the laboratory data,

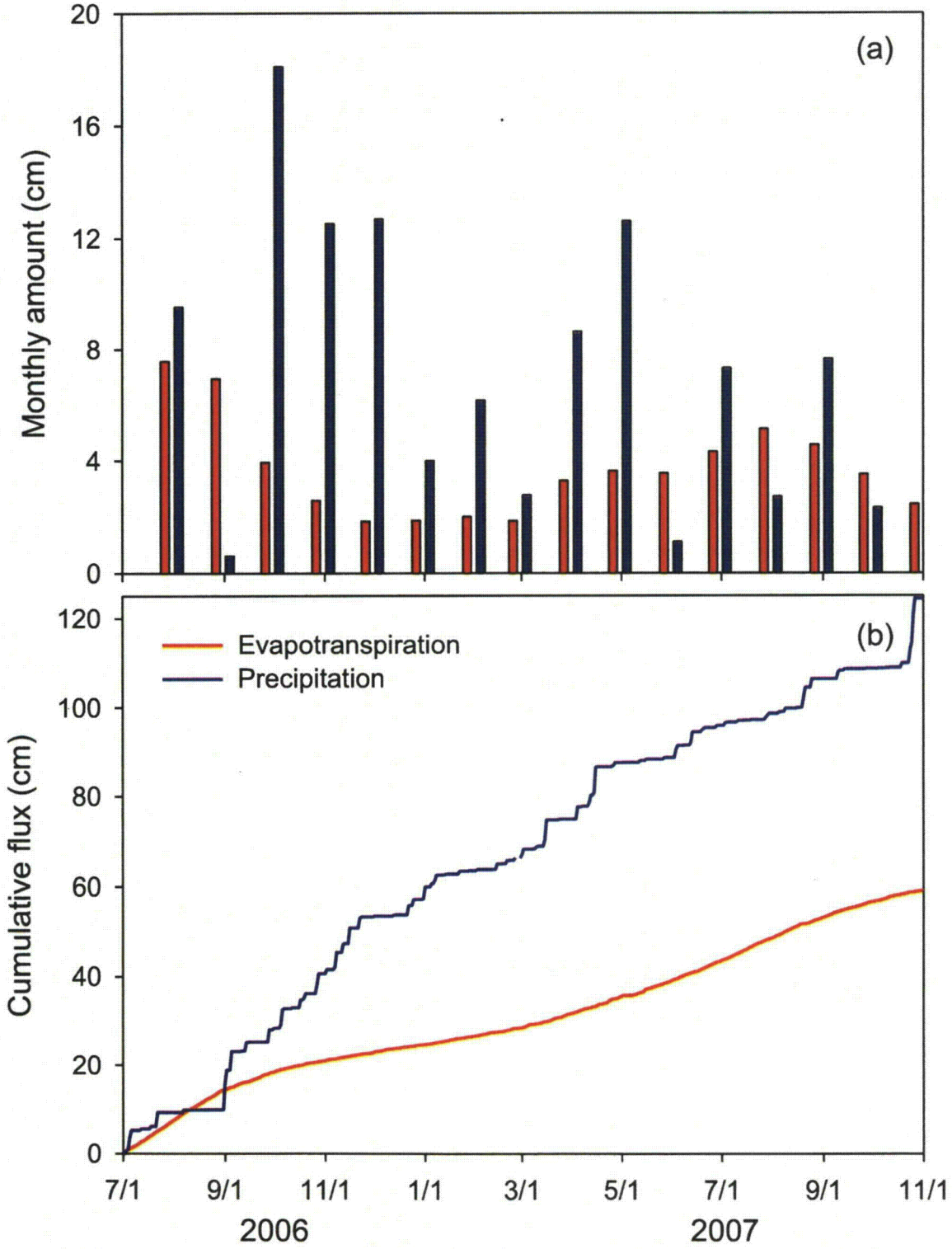

Figure 3-32. Monthly (a) and cumulative values (b) of evapotranspiration and precipitation measured at the experimental site during the monitoring period (during July 2006 – September 2007).

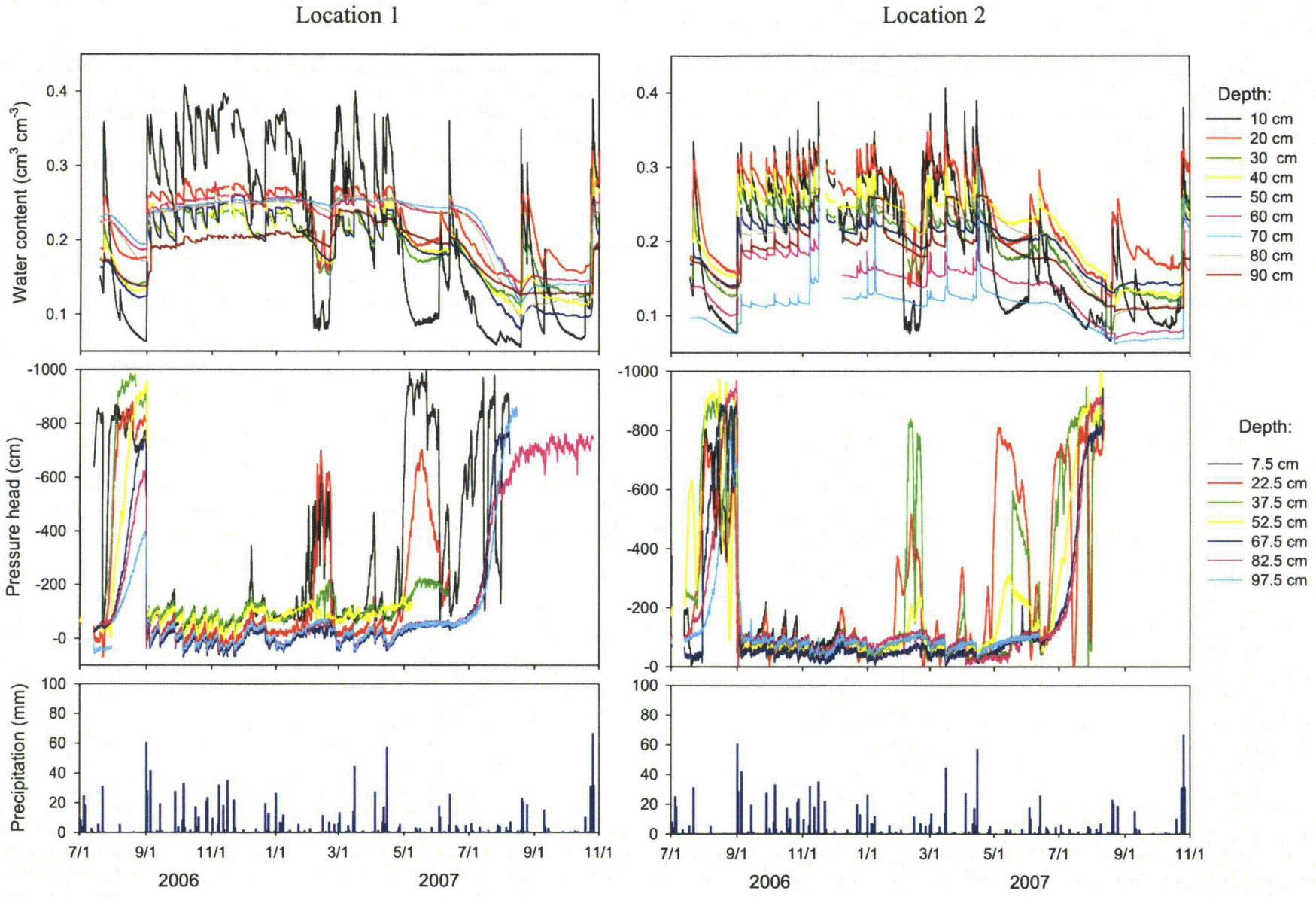

Figure 3-33. Time series of the measured soil water content and pressure heads during July 2006 – September 2007.

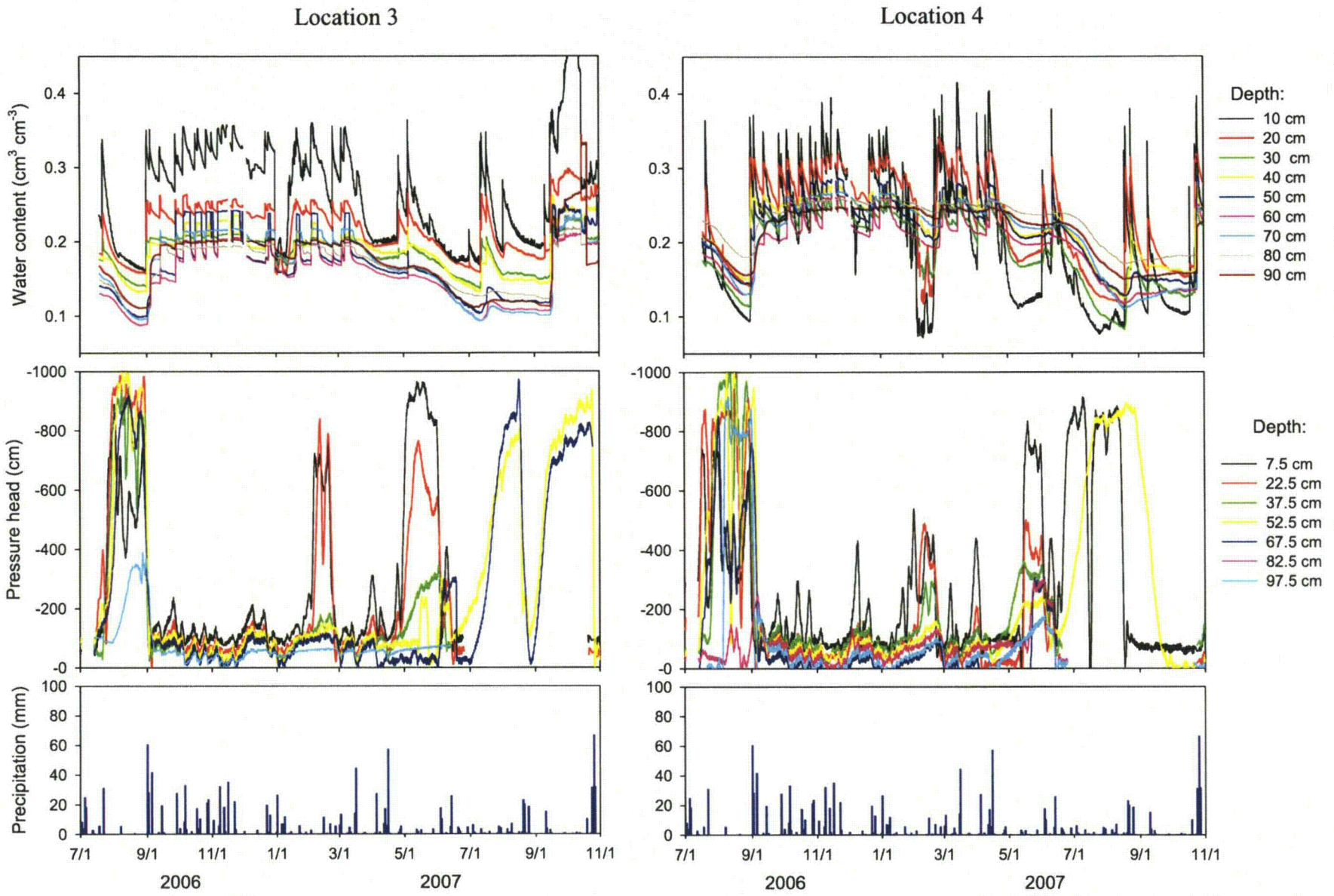

Figure 3-33 continued. Time series of the measured soil water content and pressure heads during July 2006 – September 2007.

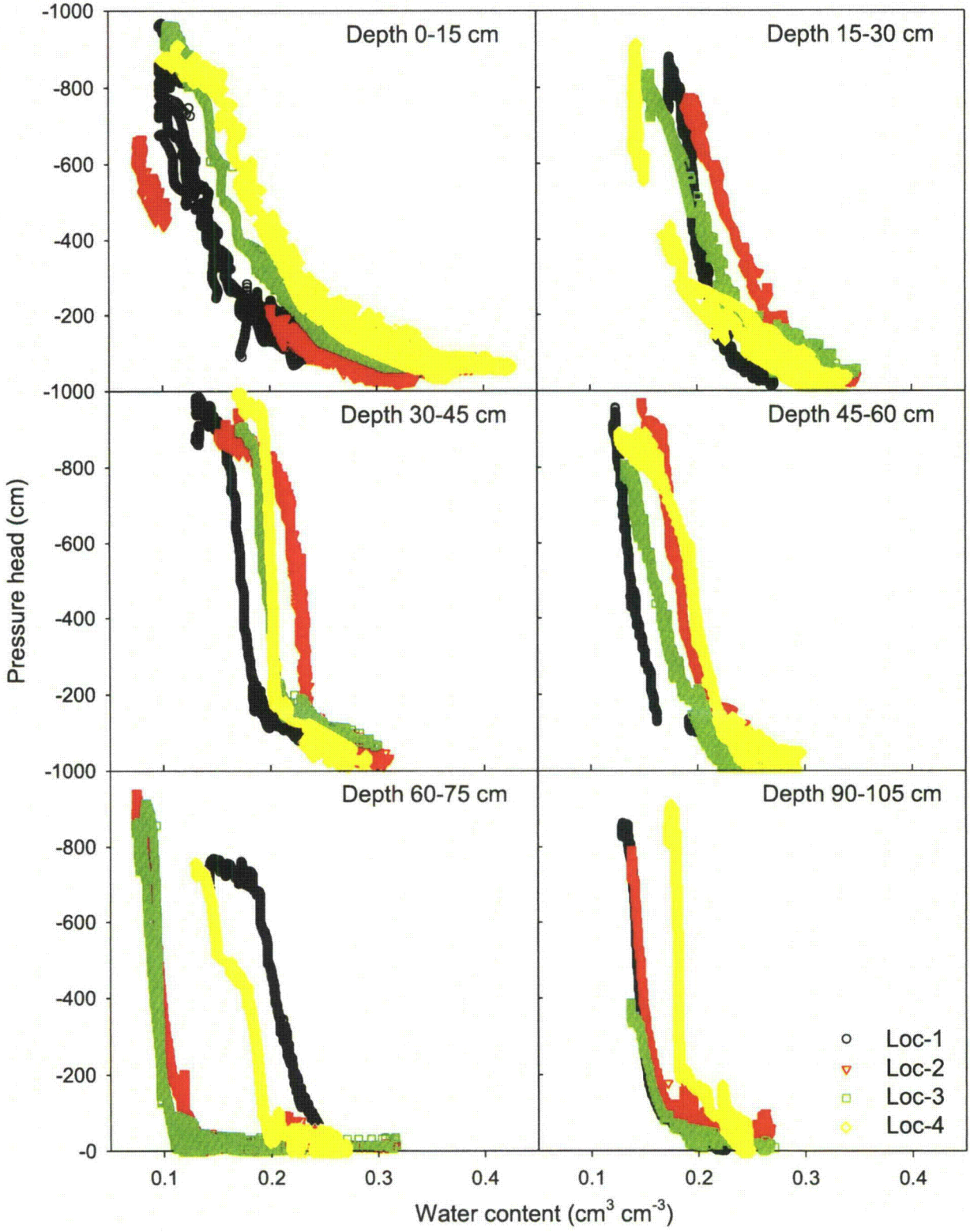

Figure 3-34. Plots of measured soil water pressure heads versus volumetric water contents at locations 1-4.

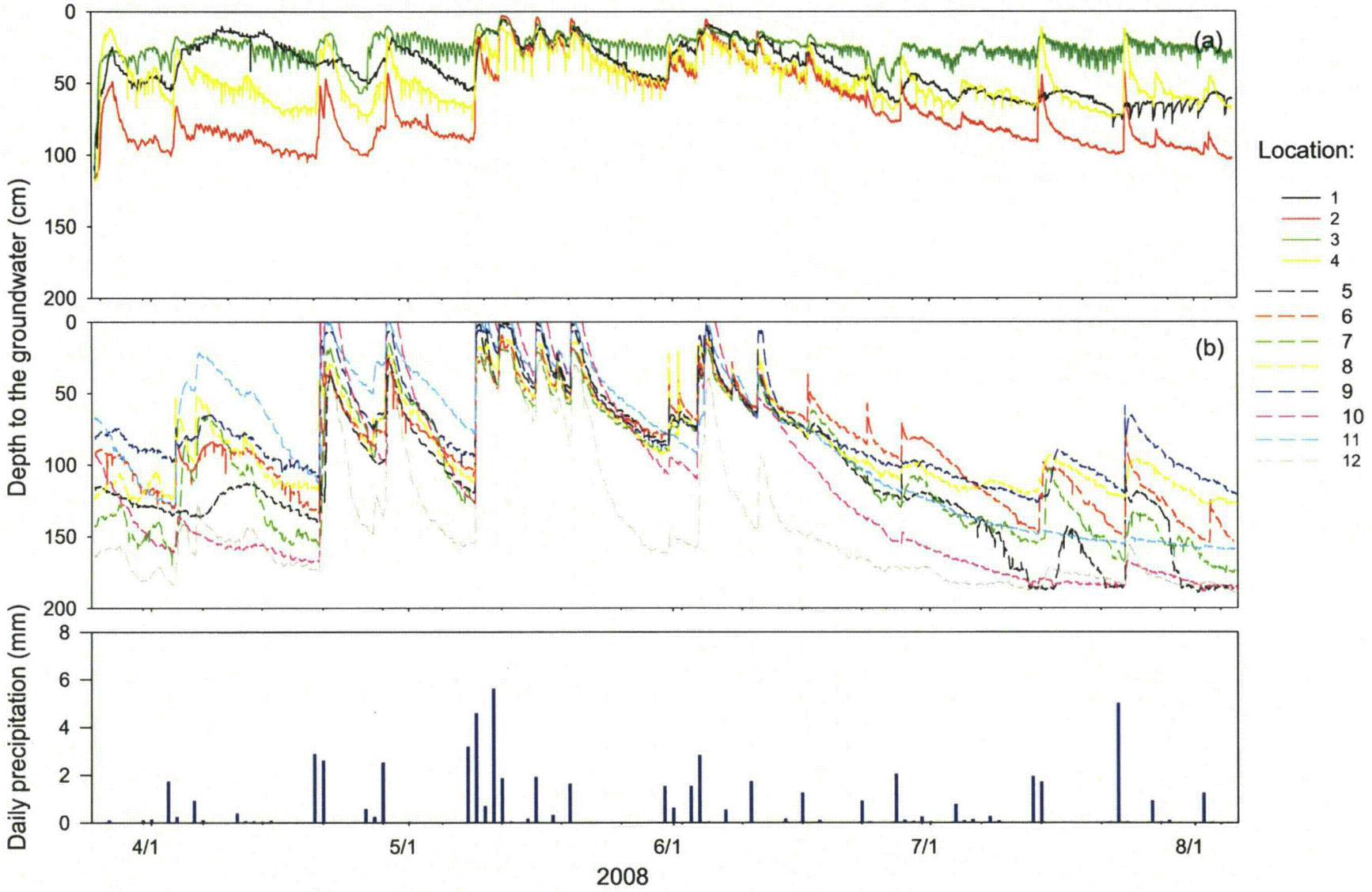

Figure 3-35. Groundwater depths measured at the experimental site during the experiments (November 2007 through March 2008).

saturated water contents gradually decreased with depth, whereas the slope of the water retention curve increased with depth. The slopes of the laboratory-measured retention curves were steeper compared to the field-measured data, resulting in lower water contents at the same pressure heads for the field measurements. The field-measured water retention curves at similar depths differed among the 4 locations. The maximum differences occurred at depths between 60 and 75 cm between locations 2 and 3 and locations 1 and 4, with the water retention curves for locations 2 and 3 shifted to lower water contents (Fig. 3-34).

Groundwater depths (GWDs) were monitored at 12 locations starting November 1st, 2007. GWD values varied between 0.0 and 200 cm during the monitoring period (Fig. 3-35). The values were consistently smaller at locations 1, 3, 6, 9 and 11, and greater at locations 7, 8, 10 and 12, particularly during continuous drying periods. Maximum seasonal variability in the GWD was observed at location 5, 8 and 12, while variability was minimal at locations 1 and 3. The GWD decreased rapidly after intensive rainfalls at all locations. Changes in the GWD were more pronounced at locations 7, 8, 10 and 12 compared to other locations during drying periods.

3.2.3.6 DILUTION TEST

A relatively simple, routinely implemented single-well tracer test is the "point-dilution" test. This test was designed to estimate the hydraulic conductivity of aquifer material. In this study we used the point-dilution test to evaluate the spatial variability of the hydraulic conductivity across the assumed tracer plume path. The test assumes that a tracer is introduced into a well and its concentration measured with time. The differential equation describing the dilution rate of the solute, $\partial c_w/\partial t$, within the water-filled well volume, V, can be written as follows:

$$\frac{V}{A}\frac{\partial c_w}{\partial t} = -q(c_w - c_b) \qquad (3\text{-}4)$$

where c_w and c_b are the concentration in the well and the background concentration in groundwater, respectively [ML^{-3}]; q represents the groundwater flux [LT^{-1}] through some vertical cross-sectional area, A [L^2], in the center of the saturated well segment; and V is the volume of water in the well [L^3].

A general definition for q describing the different factors causing dilution of a solute is given by (e.g., Halevy et al., 1967):

$$q = \alpha q_f + q_h + q_s + q_m + q_d \qquad (3\text{-}5)$$

where q_f is the velocity of undisturbed ground water flow (i.e., the undisturbed Darcy flux), q_h is the apparent flow contribution caused by density convection, q_s is the apparent flow rate caused by vertical currents in the well screen, q_m is the apparent flow rate caused by the mixing device and q_d is the apparent flow contribution caused by molecular diffusion of the solute. The factor α is defined by Halevy et al. (1967) as a "borehole effect" to account for the distortion of flow lines due to the presence of the well. A detailed definition of this factor is given in a study of Drost et al. (1968), among others. Another effect that can cause a disturbance of the flow regime may occur as a consequence of a skin created around a well. The influence of this effect on point-dilution tests was examined by Bidaux and Tsang (1991). Halevy et al. (1967) suggested that when the advective flux is relatively high compared to the diffusive flux (i.e., when $q_f >> q_d$),

the diffusion effect may be negligible. The lower limit of the measurable velocity, as suggested by Halevy et al. (1967), is in the order of diffusion (about 1 cm/day).

It is frequently assumed that the dilution rate of a solute within the injection well is simply a consequence of ground water flow only (i.e., $q=q_f$). Such an assumption is in many cases justified. Using this assumption, equation (3-4) for steady-state flow conditions (such that V, A and q are constant in time) may be integrated to produce a dilution curve that follows an exponential trend as follows (Freeze and Cherry, 1979):

$$c_w = c_b + (c_0 - c_b)\mathrm{e}^{-\frac{q_f A t}{V}} \tag{3-6}$$

where c_0 is the initial concentration in the well [ML^{-3}]. Solving for the q_f leads to

$$q_f = -\frac{V}{At}\ln\left[\frac{c_w - c_b}{c_0 - c_b}\right] \tag{3-7}$$

which shows that the Darcy flux (q_f) can be obtained immediately from the slope of a linear curve of the logarithm of the concentration versus time

Prior to the tracer experiment we carried out dilution tests for wells L10, L11 and L12. For the data analysis we used equation (3-7) and the following measured parameters: well diameters (d_w) of 0.05 m; vertical cross-sectional areas (A) of 570, 885 and 465 cm^2 for wells L10, L11 and L12, respectively; water volumes (V) of 2826, 3474 and 1825 cm^3 for the three wells, concentrations c_b=270 µSm/cm and c_0=1750 µSm/cm, and an average gradient of the water table in the area of 0.045. Using these data we obtained saturated hydraulic conductivities (K_{sat}) of 0.05, 1.34 and 2.46 m/day for the three locations (L10, L11 and L12, respectively). These numbers reflect the relatively high degree of heterogeneity of the site. They also indicate a need for substantial calibration of the flow model.

3.2.3.7 PRELIMINARY COUPLED SURFACE-SUBSURFACE FLOW MODELING

The purpose of our preliminary coupled surface-subsurface flow modeling was to estimate possible losses of water and solute to runoff. Although soils at the site are predominantly sandy, runoff had been observed in the spring and early summer. A stable runoff pathway (Fig. 3-17) was observed for three consecutive years. This indicates that the experimental site needed drainage to intercept runoff and that we needed to account for this runoff in the modeling efforts.

No software to simulate coupled surface-subsurface flow and transport was readily available when we carried out this study. We therefore developed our own modeling tool by merging the publicly available codes FEMWATER and 2DSOIL. The approach is detailed in APPENDIX C. Preprocessing and postprocessing were done in the GMS 6.0 environment.

A topography map used for the simulations is shown in Fig. 3-36. The irrigated rectangular area was located in the center of the simulated area. Rainfall was applied to this area at the rate of 0.5 m d^{-1} for 0.04 d. The tracer concentration was set to one for 0.04 d, and to zero afterwards. An initial hydrostatic distribution was assumed for the soil water content. Soil layering and soil values for the hydraulic properties were selected in accordance with the measured basic soil data (Table 3-2). Two subsurface material distributions shown in Fig. 3-37 were used in the simulations. One distribution assumed the presence of a restricting layer parallel to the soil surface, while the second distribution assumed that the restricting layer had the microtopography obtained from the ground penetration radar survey. Two initial groundwater depths (0.7 and 1.5

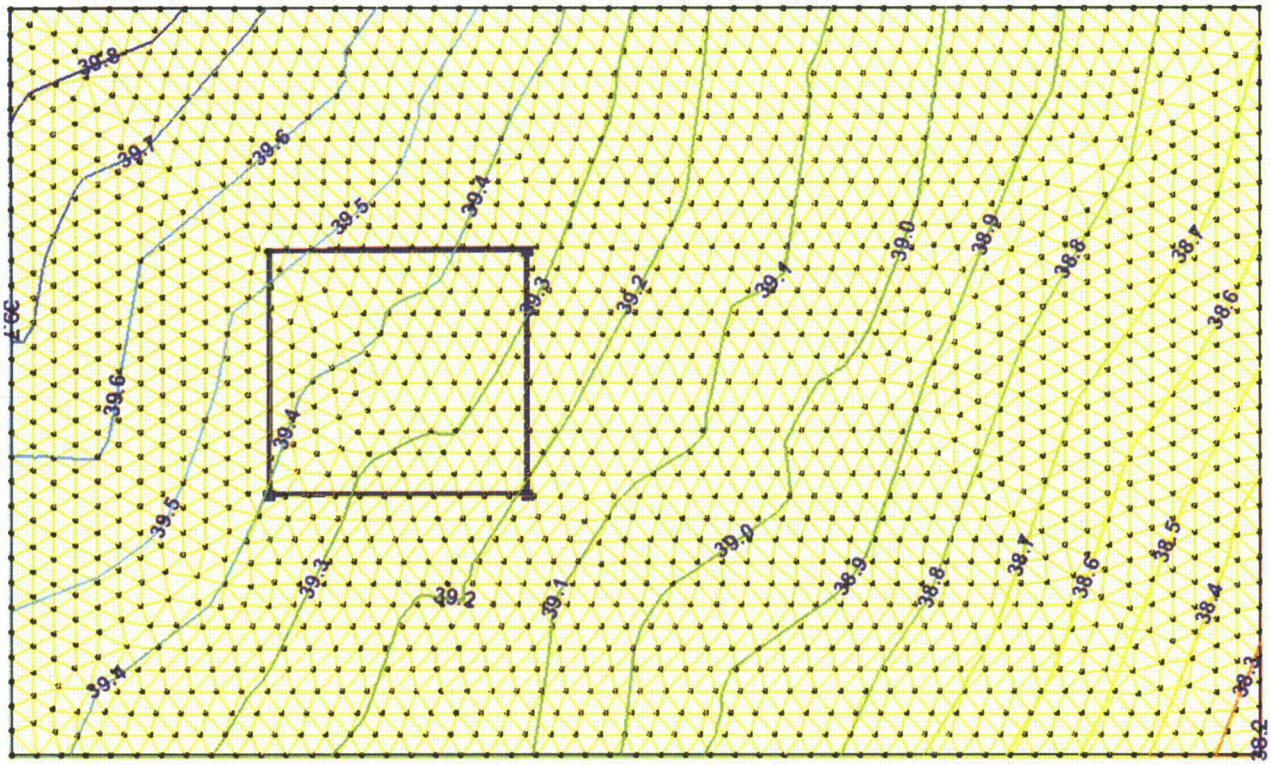

Figure 3-36. Soil surface topography and assumed finite element mesh at the surface for the coupled surface-subsurface flow and transport simulations. The blue rectangle shows the boundaries of the 10x10 m irrigated area.

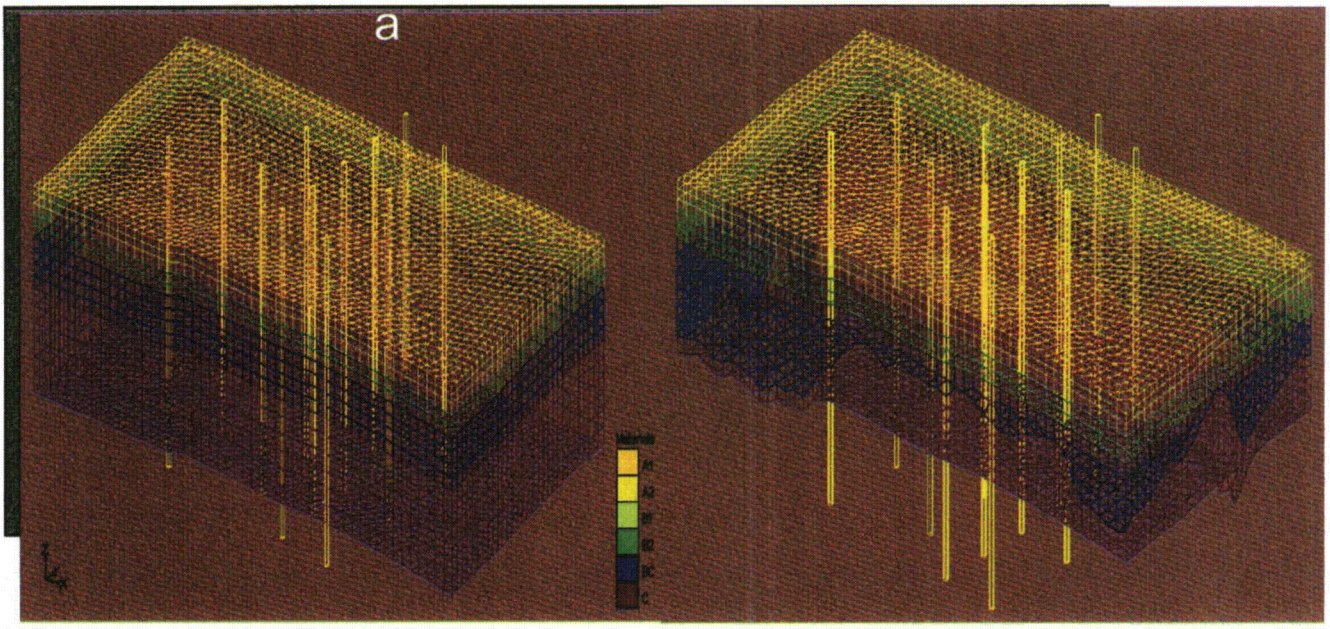

Figure 3-37. Subsurface representation and the finite element mesh in the coupled surface-subsurface flow and transport model; a –restricting layer parallel to the soil surface, b- restricting layer surface as estimated from the ground penetrating radar survey. Vertical bars show locations of the observation wells.

Table 3-2. Soil properties used in the preliminary simulations of coupled surface-subsurface flow and transport.

Horizon	Depth	Bulk density	Texture	Vertical Ksat	Lateral Ksat
	m	g cm^{-3}		m d^{-1}	m d^{-1}
Ap1	0.12	1.56	Loamy sand	0.1	0.01
Ap2	0.25	1.56	Loamy sand	0.1	0.01
B1	0.42	1.56	Sandy loam	0.1	0.01
B2	0.75	1.56	Sandy loam	0.1	0.01
BC	Variable	1.51	Sand	0.1	0.01
C	variable	1.64	Loam (60%)	10^{-8}	10^{-8}

m) were simulated, while the initial tracer concentration in the soils was set to zero. The elapsed time of the simulations was one day. The lateral boundaries of the simulation domain were assumed to be impervious.

Simulated surface flow contours are presented in Fig. 3-38. Overland flow started at t=0.0048 d and developed according to the surface topography (Fig. 3-36). Both ponding fronts and drying fronts formed during the surface runoff process. The assumed impervious lateral boundaries obviously distorted the simulated overland flow patterns. The runoff plume reached the lower (south) boundary at about 0.036 d, and then moved along this boundary. Simulated tracer concentrations in the surface water and upper soil layer are shown in Fig. 3-39. Concentrations decreased with distance from the irrigation area due to mixing with the initial soil solution and exchange between soil and surface water.

The simulations of coupled surface-subsurface flow and transport indicated that the predicted tracer concentrations in the surface water were very sensitive to grid refinement adjacent to the land surface. Very small vertical nodal spacings were required to resolve sharp concentration gradients and to control the volume of porous medium with which the surface water interacted. The lateral grid spacing was about 1 m and the vertical spacing about 0.1 m. Using smaller vertical grid sizes (~1 cm) for the surface nodes, while assuming the same horizontal mesh as before, was not successful as FEMWATER failed to run. Still, the simulations were useful in that they showed that substantial runoff was to be expected during the irrigation, and hence that surface drainage was important in order to intercept and account for the runoff.

3.2.3.8 3D SUBSURFACE FLOW AND TRANSPORT MODELING

Preliminary modeling of the planned tracer experiment was carried out using the HYDRUS-3D code simulating variably-saturated water flow and solute transport (Šimůnek et al., 2007). The model is based on the Richards equation for flow and the advection-dispersion equation for transport. Assuming a conservative tracer (no sorption and decay), these equations are, respectively,

$$\frac{\partial \theta}{\partial t} = \nabla[K \cdot (\nabla h + 1)] \tag{3-8}$$

$$\frac{\partial \theta C}{\partial t} = \nabla(\mathbf{D} \cdot \nabla C - \mathbf{q}C) \tag{3-9}$$

where θ is the volumetric water content (L^3/L^3), t is time (T), h is the pressure head (L), **K** is the hydraulic conductivity tensor (L/T), C is the solution concentration (M/L^3), **D** is the hydrodynamic dispersion tensor (L^2/T), and **q** is the Darcy-Buckingham flux vector (L/T).

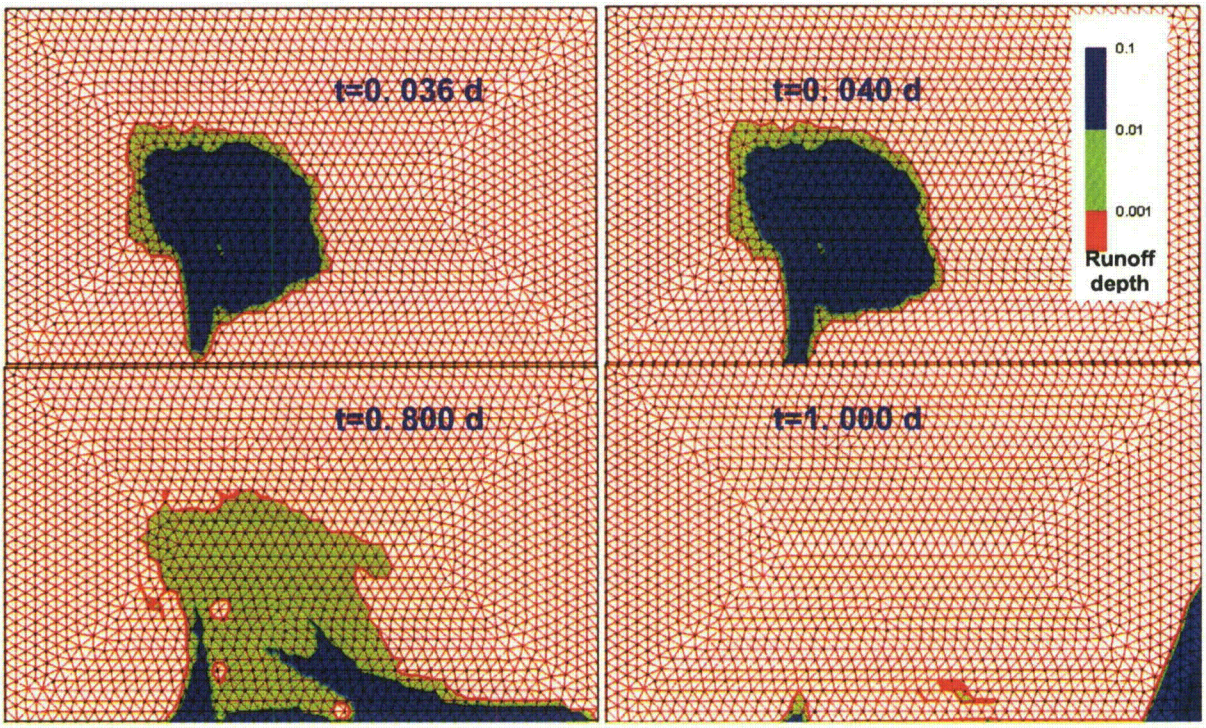

Figure 3-38. Development of the overland flow as obtained with the preliminary coupled surface-subsurface simulations.

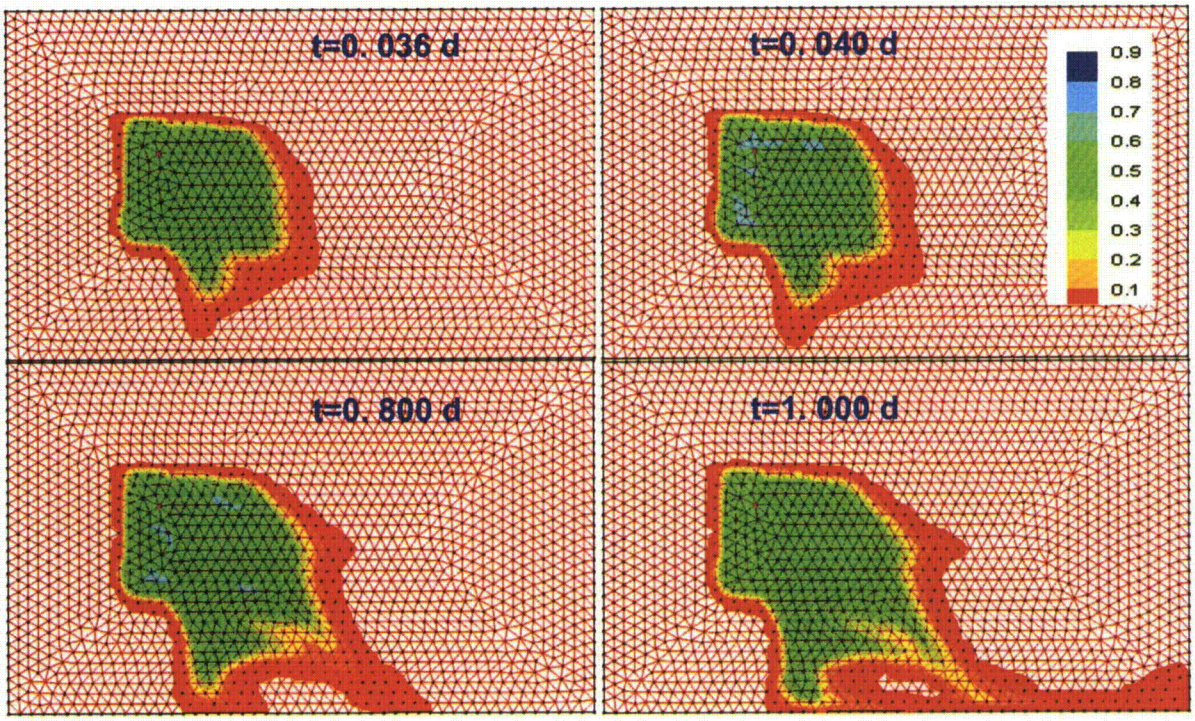

Figure 3-39. Tracer concentrations in overland flow or the upper soil layer as obtained with the preliminary coupled surface-surface solute transport simulations.

The soil water retention and unsaturated hydraulic conductivity functions needed for solution of Eq. (3-8) were described using the van Genuchten (1980) relationships:

$$S_e = \frac{\theta - \theta_r}{\theta_s - \theta_r} = \left[1 + (\alpha |p|)^n\right]^{-m} \tag{3-10}$$

$$K(S_e) = K_{sat} S_e^{\tau} \left[1 - \left(1 - S_e^{1/m}\right)^m\right]^2 \tag{3-11}$$

respectively, where S_e is relative saturation, θ_r is the residual water content (L^3/L^3), θ_s is the water content at saturation (L^3/L^3), K_{sat} is the saturated hydraulic conductivity (L/T), α (L) and n (-) are shape parameters, m=1-1/n, and τ=0.5.

Application of equations (3-8) to (3-11) to the field tracer experiment using HYDRUS-3D requires definition of the domain boundaries, the initial and boundary conditions, a numerical finite element mesh, and soil hydraulic and solute transport parameters. Based on experimental data that included the locations of the tracer application plot and observation (sampling) wells, the topography of the soil surface, and the low-permeability lower boundary, we considered a 3D layered hexahedral flow domain having 50x30 m lateral dimensions and being 4 m in height (Fig. 3-40), and having with slopes of -1.35° and 1.05° in x and y directions, respectively. The domain was discretized into a structured (triangular prisms) finite element mesh consisting of 120,000 3D elements. The finite element mesh sizes were 0.1 m and 1 m in the vertical and horizontal directions, respectively.

As initial condition for the water flow equation we used an equilibrium hydrostatic distribution of the pressure head with depth. On a horizontal plane, this distribution corresponded to a groundwater gradient of -0.045 along the x-axis such that the water table in the center of the irrigated plot was at a depth of 1.55 m. The initial concentration for the transport simulations was taken to be zero.

The boundary conditions for water flow were as follows (see also Fig. 3-41): along the side boundaries, the pressure head corresponded to the initial distribution; along the soil surface a water flux of 0.1 m/day was imposed on the irrigation plot area; the remainder of the soil surface was considered to be a zero-flux boundary. We further assumed a pulse duration of 0.5 day for a conservative tracer applied with the infiltrating water at a concentration of 1000 mg/l.

Table 3-3 presents the hydraulic parameters used in simulations of a layered soil profile. The parameters were obtained by calibrating the flow model to the flux experiment (section 4.1. 2), but with the saturated hydraulic conductivity values being decreased 10 times. The longitudinal and transversal dispersivities were assumed to be 0.5 and 0.1 m, respectively. Fig. 3-42 shows simulated distributions of the pressure head and the concentration at 1.5 m depth after 30 days. A groundwater mound developed due to intensive irrigation in the plot area. This irrigation influenced the transport of the tracer, which acquired a toroid (donut)-like distribution with higher concentrations downstream. Fig. 3-42a shows the effect of the imposed constant pressure head boundary condition on the pressure head distribution within the domain. The influence of the boundaries was quite strong since they were relatively close to the irrigation plot (10 m, except for the downstream boundary).

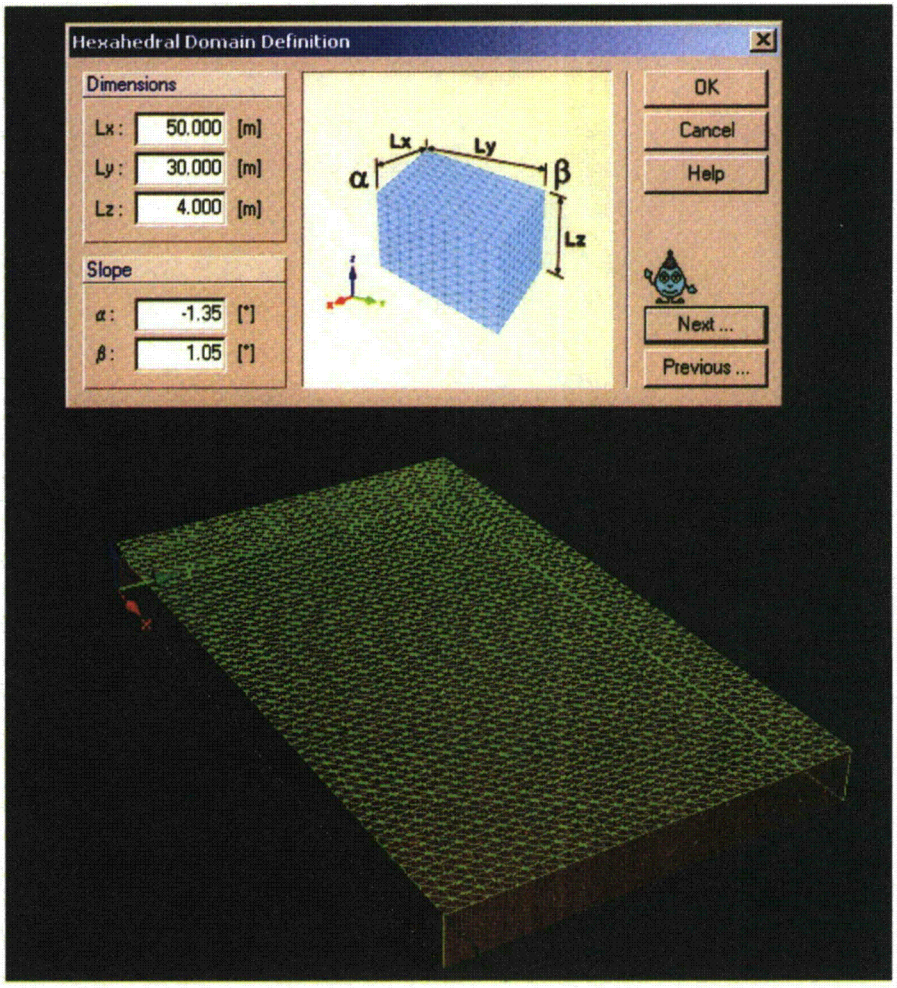

Figure 3-40. Assumed simulation domain for solving the flow and transport problem with HYDRUS-3D.

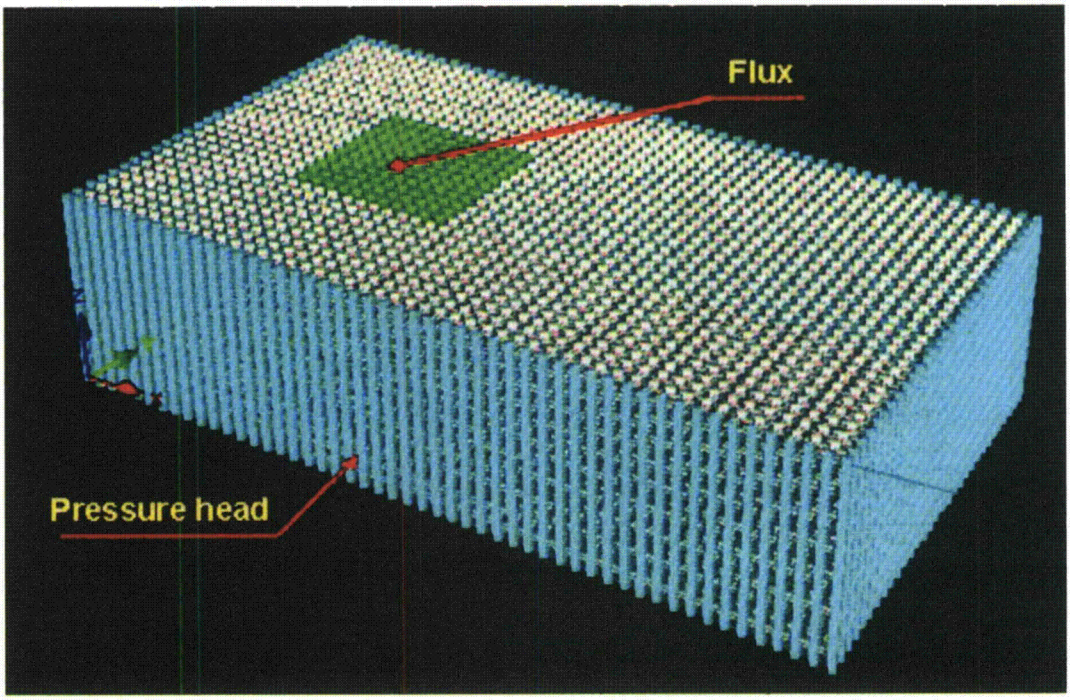

Figure 3-41. Definitions of the invoked boundary conditions.

a)

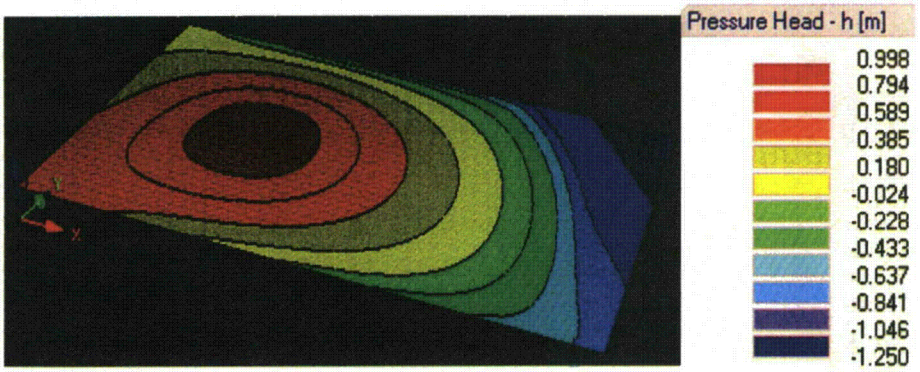

b)

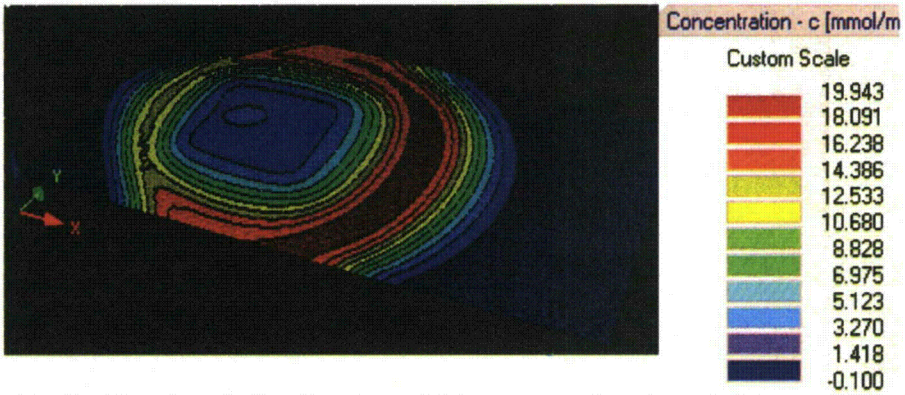

Figure 3-42. Simulated distribution of (a) pressure head, and (b) concentration after 30 days (layer 1.5 m depth).

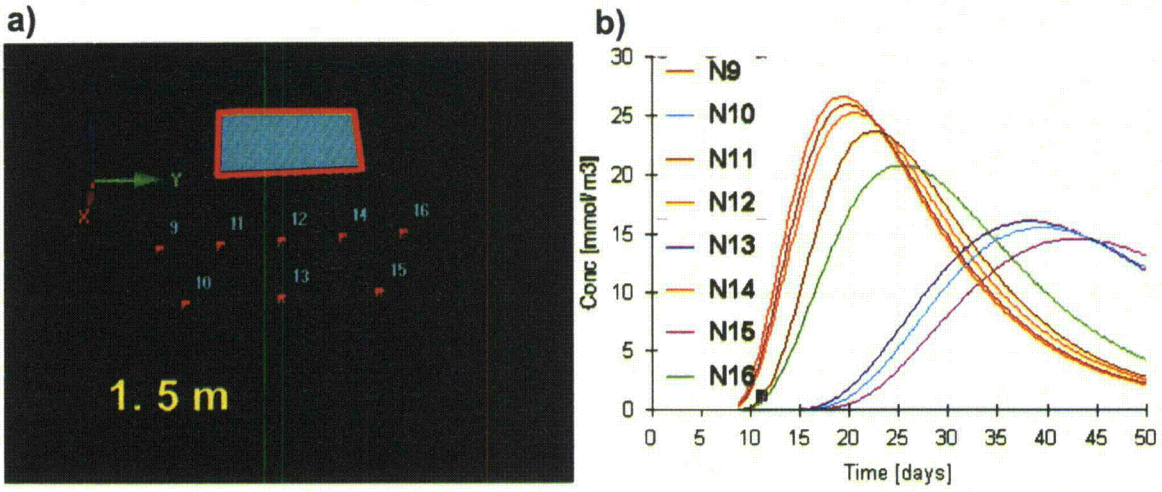

Figure 3-43. Location of (a) observation nodes and (b) the simulated breakthrough curves.

Table 3-3. Unsaturated soil hydraulic parameters.

N	Layer cm	Parameters				
		θ_s	θ_r	α , m^{-1}	N	K_s, m d^{-1}
1	0-30	0.327	0	4.6	1.62	2.4
2	30-50	0.351	0.024	5.5	1.46	2.7
3	50-80	0.260	0	5.4	1.33	4.5
4	80-150	0.315	0	6.9	1.76	3.6
5	150-250	0.330	0	4.4	3.00	1.2
6	250-400	0.410	0.095	1.9	1.31	0.01

Sixteen observation nodes (8 at the depth of 1.5 m and of 2 m) were assigned along 2 rows at distances of 7 m (5 nodes at each depth) and 14 m (3 nodes at each depth) from the edge of the irrigation plot in the downstream groundwater flow direction. Fig. 3-43b shows the simulated breakthrough curves at the observation nodes at 1.5 m depth (concentrations at a depth of 2 m were nearly identical). The simulations indicated that the tracer should arrive at the first and second rows of observation nodes after approximately 8 and 15 days, respectively. The maximum concentrations along the first row of observation nodes were observed after 18-25 days, depending upon the location of the node in the plane, but with values that were diluted about 40-50 times relative to the initially applied tracer concentration. By comparison, the maximum concentration along the second row of observation nodes occurred after 38-43 days.

A significant amount of runoff was observed after the tracer experiment started. Actually, most of the applied water turned into overland flow. We therefore decided to change the irrigation schedule by apply water only from 8:00 to 10:00 h in the morning and from 4:00 to 6:00 h in the afternoon. Consequently, a simulation was performed to account for this change in the soil surface boundary condition. The saturated hydraulic conductivity was decreased by a factor of 10 to increase runoff. The calculations suggested that for this scenario one could expect the tracer to arrive at the first row of observation nodes 30 to 45 days after starting the experiment, which actually happened.

3.2.4 EXPERIMENTAL SETUPS, SCHEDULES, AND RESULTS

3.2.4.1 FLUX MEASUREMENT EXPERIMENT

Experimental setup.

The flux experiment was set up as shown in Fig. 3-1. The flow and concentration measurements of the pumped water were supplemented with measurements of the water content using the soil moisture capacitance probes (MCPs). Fig. 3-44 shows the depth to the subsurface restricting layer at and near the experimental area, and the location of the observation wells and soil moisture capacitance probes. The MCPs were located about 11 m west of the well used for measuring solute fluxes. They monitored soil water contents every 10 minutes. The probes were centered 0.1, 0.3, 0.5, 0.8, 1.2, 1.5, 1 and 1.8 m below the soil surface. Details of the setup are given by Gish and Kung (2007). Here we give only a brief overview to provide a good understanding of the full context of the experiments.

A schematic of the well configuration is shown in Fig. 3-45. The observation well consisted of a 0.3-m wide hole in the top 0.3 m, while from 0.3 m to 3.0 m the well size was reduced to 5-cm. Since wet sand can collapse, the hole (especially for the bottom of the 5-cm hole) jettable well points were used so that the wells could be pushed to the desired depths just above the underlying clay lens (2.5 to 3 m). Once the slotted well was inserted and well extensions were attached, blow sand was poured into the gaps between the observation well and the surrounding soil (for only the 5-cm hole). Since slots in the well can become clogged upon soil insertion, a positive water pressure was applied to the top of the observation well to clean out the well slots and activate the well. Once the sand had settled from the 0.3 to 3.0 m depths, a 0.2-m polyurethane (PU) disk was tightly fitted around the well at a depth of 0.3 m depth, while the original soil from 0 to 0.3 m was placed around the well. The purpose of the PU disk was to minimize water and solute flow down along the observation well, thus forcing water and solutes to move into the soil matrix. To minimize disturbance, the observation well was configured with two extensions. The lower extension was connected to the slotted well just above the polyurethane collar (about 0.30 m below the soil surface). For tillage and planting operations the well was capped at this juncture so that tillage implements would not disturb the well while the area around the well could receive the same tillage treatment as the rest of the field. The second, more shallow extension was connected to the well just below the soil surface. This configuration allowed the above surface portion of the well to be removed for field operations.

The average depth to the water table during the week prior to this study was 1.68 m. The depth of water table was continuously monitored with a submergible pressure transducer (Eijkelkamp, Agrisearch Equipment, Giesbeek, The Netherlands) located 2.9 m below the soil surface. A line for pumping water from the observation well was inserted 0.15 cm below the water table and attached to a portable pump which ran throughout the duration of the experiment. Water flow rates exiting the well were monitored by manually capturing the water in graduated cylinders. Since water flow rates from the pumped well could vary over short time durations (seconds), three consecutive outflow volumes, each over a 1-minute duration, were collected at each observation time. To ensure that the entire solute breakthrough curve was accurately monitored, observation times for the manual collection and for monitoring the flows were scheduled every 15 minutes initially and then gradually increased to every hour. In between the water flow measurements, well water was pumped into a drainage pipe that carried the water 200-m off-site.

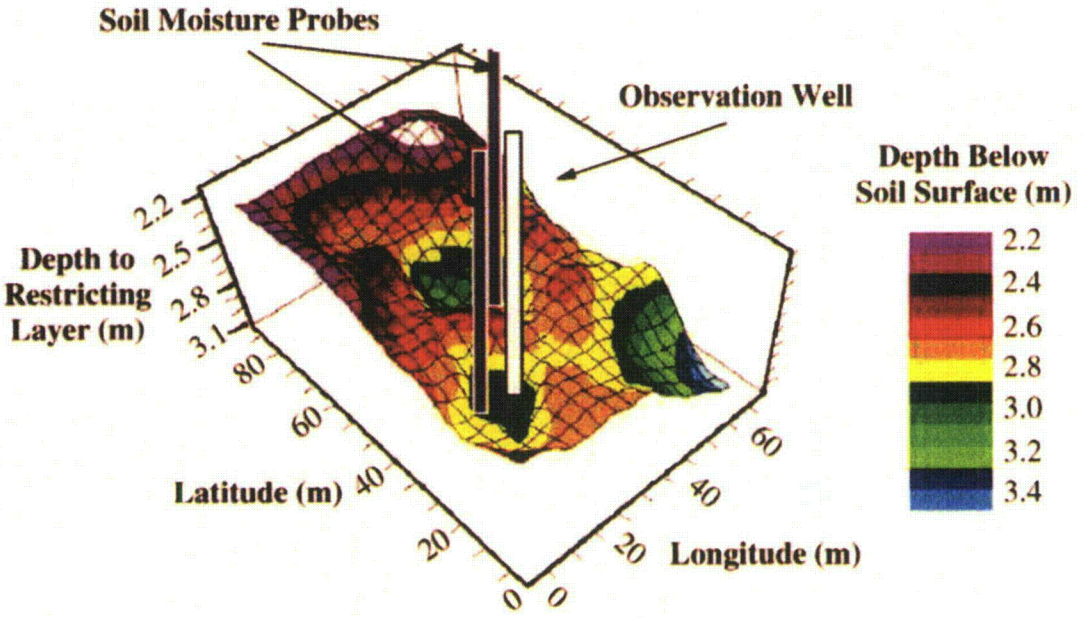

Figure 3-44. Depth to the GPR-identified clay lens and location of observation wells and soil moisture capacitance probes (after Gish and Kung, 2007. Permission to use this copyrighted material is granted by Geoderma).

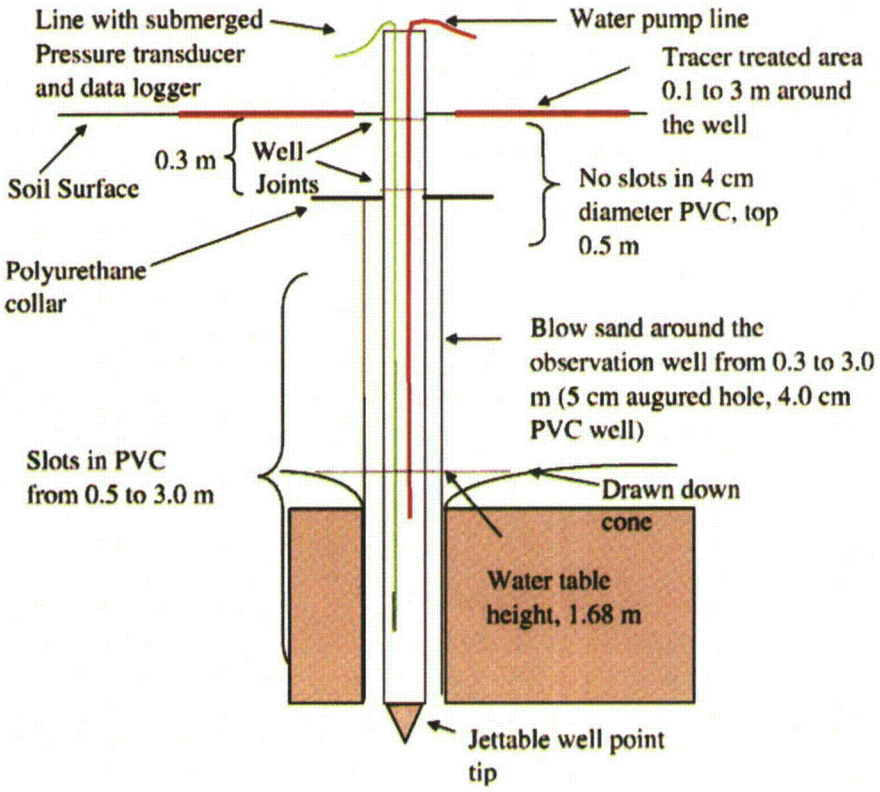

Figure 3-45. Schematics of observation well installation and instrumentation. Schematic is not to scale, i.e., the PVC well is only 3.8 cm in diameter, but 3 m in length (after Gish and Kung, 2007. Permission to use this copyrighted material is granted by Geoderma).

No tracers were applied within a radius of 0.1 m of the observation well. Three tracers were manually sprayed between 0.1 to 3.0 m around the well, resulting in a treated area of about 28.2 m^2 (Fig. 3-45). Bromide (0.1064 kg Br m^{-2}) was applied 1.5 days before irrigation was initiated, and allowed to diffuse into the coarse-textured soil matrix at the soil surface. No precipitation other than irrigation was observed at this site, nor for the duration of the entire study. To ensure that water reaching the water table would be collected, we began pumping water continuously from the observation well two weeks before Br was applied. This would also establish and maintain a steady drawdown cone around the well. About 1.5 days after the Br application, but immediately before irrigation was initiated, a Cl pulse (0.052 kg Cl m^{-2}) was surface applied. Pentafluorobenzoic benzoic acid (0.17 kg PFBA m^{-2}) was applied 7 h after the experiment began. This tracer was used to determine any changes in chemical transit times after the soil profile had became wetter and possibly more hydrologically active. According to Jaynes (1994) and Kung et al. (2000b), PFBA is as conservative as Br and Cl, and has almost identical breakthrough patterns. As a result, three mobile chemical conservative tracers were used in this study, and monitored as they arrived in the observation well

While taking the water flow measurements, a single 30 ml water samples were collected and stored in a refrigerator until its chemical composition could be determined. These samples, as well as subsequent solution samples during the experiments, were split and eventually analyzed by high performance liquid chromatography (HPLC) for PFBA and by ion chromatography (IC) for Br and Cl. Within 12 hours of their collection in the field, the samples were being analyzed for Cl and Br while the remainder of the samples were stored in a refrigerator. Analysis of PFBA did not begin until a week after the experiment was terminated. Since Cl and Br were applied first, their breakthrough curves were used to determine when to terminate the experiment. The IC conditions were: mobile-phase, Sodium Borate-Gluconate (2%), n-Butanol (2%), acetonitrile (12%); flow rate, 1.2 ml min^{-1}; guard column, Waters Corporation (Milford MA) IC-Pak Anion Guard-Pak; analytical column, Waters Corporation (Milford MA) IC-Pak Anion (50 mm x 4.6 mm i.d.); and injection volume, 50 µL; and conductivity detection. The detection limits for of Br, and Cl were 0.1, 0.2 mg L^{-1}, respectively. Calibration curves generally had r^2 values greater than 0.99. The HPLC conditions were as follows: mobile-phase, acetonitrile (40%), 15 m*M* KH_2PO_4 (titrated to pH 2.6 with phosphoric acid) (60%); flow rate, 1.8 ml min^{-1}; guard column, Spherisorb SAX (10 mm x 4.6 mm i.d., 5-µm, Sigma-Aldrich, St. Louis, MO); analytical column, Supelcosil SAX1 (25 cm x 4.6 mm i.d., 5-µm, Sigma-Aldrich, St. Louis, MO); injection volume, 50 µL; and UV detection, 205 nm. The detection limit for PFBA acid was 1 µg L^{-1}. Calibration curves generally had r^2 values greater than 0.999.

Cl measured in the observation well could eventually come from three sources: 1) Cl already in the groundwater, which had been measured weekly for several months prior to Br application; 2) Cl from city irrigation water, which was measured throughout study by sampling the irrigation water, and 3) the Cl pulse itself that was to be monitored. The average Cl concentration of groundwater prior to irrigation was 7.3 mg Cl L^{-1}, while the average concentration of city water was 8.75 mg Cl L^{-1}. To separate the various sources of Cl, the averaged concentration observed in groundwater immediately before the study, was subtracted from all well water samples after Br application. At the time when Cl levels began to rise relatively sharply, the Cl concentration of the city irrigation water was subtracted from the remaining well water samples. The remaining Cl was assumed to be from the Cl pulse applied around observation well. Unfortunately, there was some ambiguity in determining exactly when

the rapid increase in Cl occurred. Cl (from the tracer as well as from city irrigation water) will interact with the soil matrix resulting in a diffuse front (a gradual change in Cl), rather than in a sharp front (an abrupt change in Cl). As a result, Cl concentrations from city irrigation water may not have been subtracted as soon as they should have been. On the other hand, the entire 8.75 mg Cl L^{-1} was subtracted instead of only a portion. Fortunately, flows and concentrations were being taken about every 30 min at this time, so the shift should not be more than one hour (two readings).

A 4.1 mm h^{-1} irrigation rate was applied to the research area (30 m by 40 m) using 7 rows of 4 solid-state sprinklers, all set at a 6.4 m spacing. The sprinkler nozzles used were Weather Tec G50 (WCG5W with 23 degrees, Roberts Irrigation Company, Inc, Plover, WI). Christiansen coefficients of uniformity measured at 2 am (when winds were negligible) were 85%. Average daily wind speeds during the study typically ranged from 0.34 to 0.96 m s^{-1}; however, there were three days with wind speeds exceeding 1 m s^{-1}. On these three days, the average daily wind speed ranged from 1.38 to 2.5 m s^{-1}, with corresponding maximum wind speeds (for 10 minute durations) ranging from 4.8 to 5.9 m s^{-1}. Although no measurements of uniformity were taken at those times, we believe that they decreased during the periods of high wind.

Water samples from the well were collected about every 4 hours during the time period between Br application and the irrigation. The pump intake line was located 0.15 m below the water table. The pump used for our study had a capacity of more than 0.34 L s^{-1}. The background flow rates from the well before the irrigation were about 0.03 L s^{-1}, but reached a maximum of 0.18 L s^{-1} at the end of the study. Immediately following Cl application, the irrigation system was turned on and well samples were collected manually every 15 minutes for the first 24 hours. From 24 to 72 hours after irrigation began, well samples were manually collected about every 30 min, and each hour afterwards. At one point, about two days into the irrigation, the pump failed and had to be replaced.

The investigation was conducted in November when air temperatures ranged from 1 to 7° C. Samples were collected from the field every 6 hours and immediately prepared for the chemical Br and Cl analyses. From each 30 ml well sample, 15 ml was refrigerated for analysis of PFBA by HPLC. When most of the Br and Cl breakthrough curves appeared to be completed, the study was terminated.

Experimental results.

Flow rates from the observation well were approximately 0.03 L s^{-1} for the first 12 hours after irrigation began, but then slowly increased until the study was terminated 7 days later (Fig. 3-46). Three consecutively measured 1-min flow volumes at each observation time were used to estimate coefficients of variation (CV). Values were about 5%, ranging from 1 to 10% regardless of the flow volume.

Average water table depths, along with their temporal variability over each 24-h period, are shown in Fig. 3-47. At the beginning of the study, the water table height was 1.68 m and remained near that value for the duration of the experiment. Although the standard deviation generally increased as the study progressed, there was no significant change in the average water table depth with time.

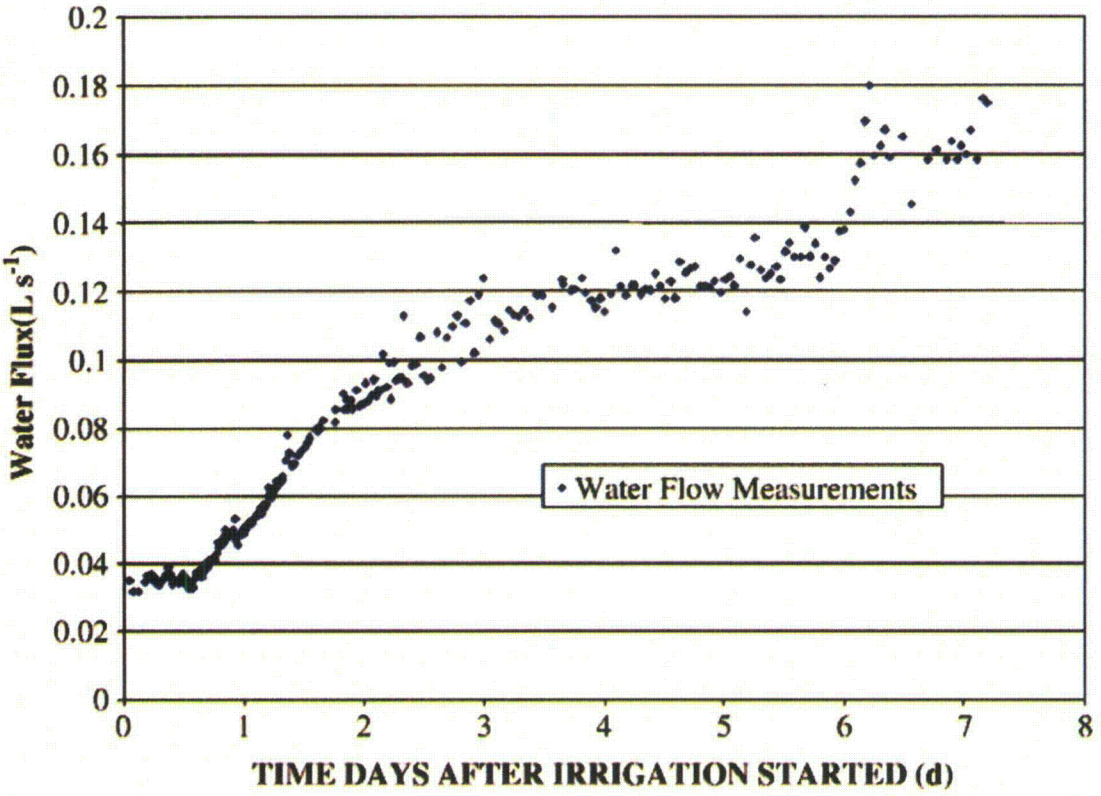

Figure 3-46. Averaged water flow rates pumped from the observation well as a function of time (after Gish and Kung, 2007. Permission to use this copyrighted material is granted by Geoderma).

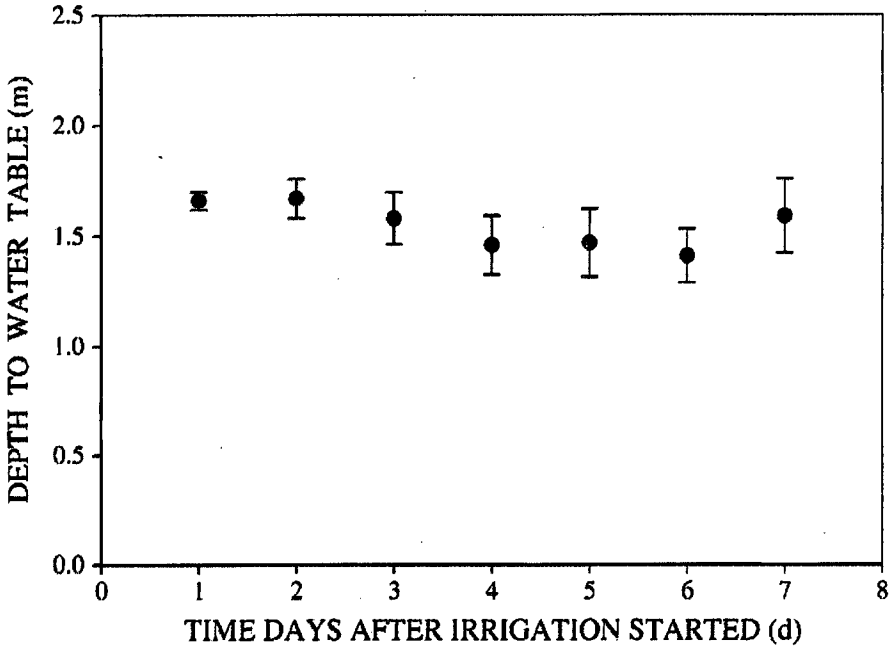

Figure 3-47. Water table heights in the observation well. Error bars represent one standard deviation (after Gish and Kung, 2007. Permission to use this copyrighted material is granted by Geoderma).

The soil water sensors indicated a sudden increase in soil water contents at about 1.5 days after Br application, which coincided with the onset of irrigation (Fig. 3-48). The relatively low water contents observed just prior to irrigation (about 0.10 cm^3 cm^{-3} at the 0.1 m depth) reflected the low water holding capacity of the coarse-textured surface soil. Soil water contents in the top 0.5 m remained well below saturation throughout the study.

The real-time soil moisture profile data also showed a lag in the rapid rise in soil water contents with depth as the infiltrating water in time reached a given depth, with the 0.1 m sensor rising first and the 0.5 m sensor rising last. Soil water contents at 0.8 m rose sharply from 0.07 cm^3 cm^{-3} to about 0.15 cm^3 water cm^{-3} two days after Br application (or about 12 hours after irrigation was initiated), but lagged slightly behind the water contents at 0.5 m. The water contents at 0.8 m remained low, near 0.15 cm^3 cm^{-3} throughout most of the study and then suddenly increased to 0.28 cm^3 cm^{-3} during the last few hours of the experiment. Saturation at this depth corresponded to a water content of 0.33 cm^3 cm^{-3}. Meanwhile, water contents 1.2 m below the soil surface started to rise such that 3 days after Br application (1.5 days after irrigation started) this soil layer began to reach saturation. The soil moisture sensor at 1.5 m showed the highest water contents even though the water table at the observation well was being maintained at 1.68 m. The soil water contents at 1.8 m were less than those at 1.5 m even though saturation was reached there. The lower water contents at 1.8 m were probably due to the presence of gravel, which in general has a lower porosity. Soil textures at 1.2 and 1.5 m were the same (although they showed slightly different maximum water contents), thus suggesting that the 1.2-m water contents were likely due to capillary fringe effects. The rapid rise in water contents at 0.8 m nearly 8 days after Br was applied (6.5 days of irrigation) indicated that the 1.2 and 1.5 m depths may have been saturated by the end of the study 11 m away from the observation well.

Solute breakthrough curves (BTC) as a function time after irrigation started are shown in Fig. 3-49. To accommodate direct comparisons, each observed concentration was divided by the mass applied. Early increases in Cl before 1.5 days after application were not known, but accounted for << 1% of the total applied Cl. The rapid increases in solute concentration between days 1.5 and 2 were well quantified, as were the solute tails which began about three days after application. The rapid rise in concentration for each tracer reflected the front of the solute pulses arriving at the well. The rapid rise appeared to occur first for PFBA, which was applied 7 hours after application. However, there was no difference in the rapid rise of Cl or Br, which suggests that for this coarse-textured soil Br and Cl were transported initially through similar pore systems, while on average slightly larger pores may have contributed to the transport of PFBA.

Cumulative tracer masses pumped out of the well are shown in Fig. 3-50. The recovery was excellent in this experiment. Percent recoveries were 100% for PFBA, 102% of bromide, and 97% for chloride (after correction of the chloride contents from ground and city water).

3.2.4.2 LATERAL FLOW EXPERIMENT

Experimental setup.

The lateral flow experiment was set up as shown in Fig. 3-18 – Fig. 3-20. A windshield (160 cm height) was constructed around locations 1-4 to minimize wind impact on irrigation uniformity. Four sprinkler nozzles (Olson Red Mini Rotor Style Drip Emitter by Olson Irrigation Systems, Santee, CA) were installed at heights of 1 m in the corners of the irrigation plot. One additional sprinkler nozzle (Olson Green Mini Rotor Style Drip Emitter) was installed at a height of 10 cm above the soil surface in the center of the plot (Fig. 3-18). The system was designed to provide continuous irrigation at a rate of 9.6 cm d^{-1}, with a uniformity coefficient of 0.86, to the

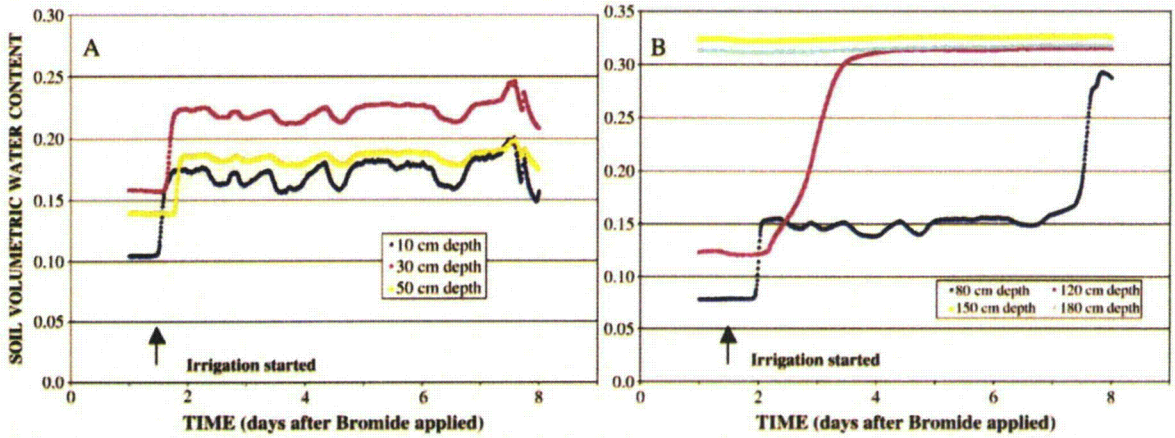

Figure 3-48. Time series of the soil water content (after Gish and Kung, 2007. Permission to use this copyrighted material is granted by Geoderma).

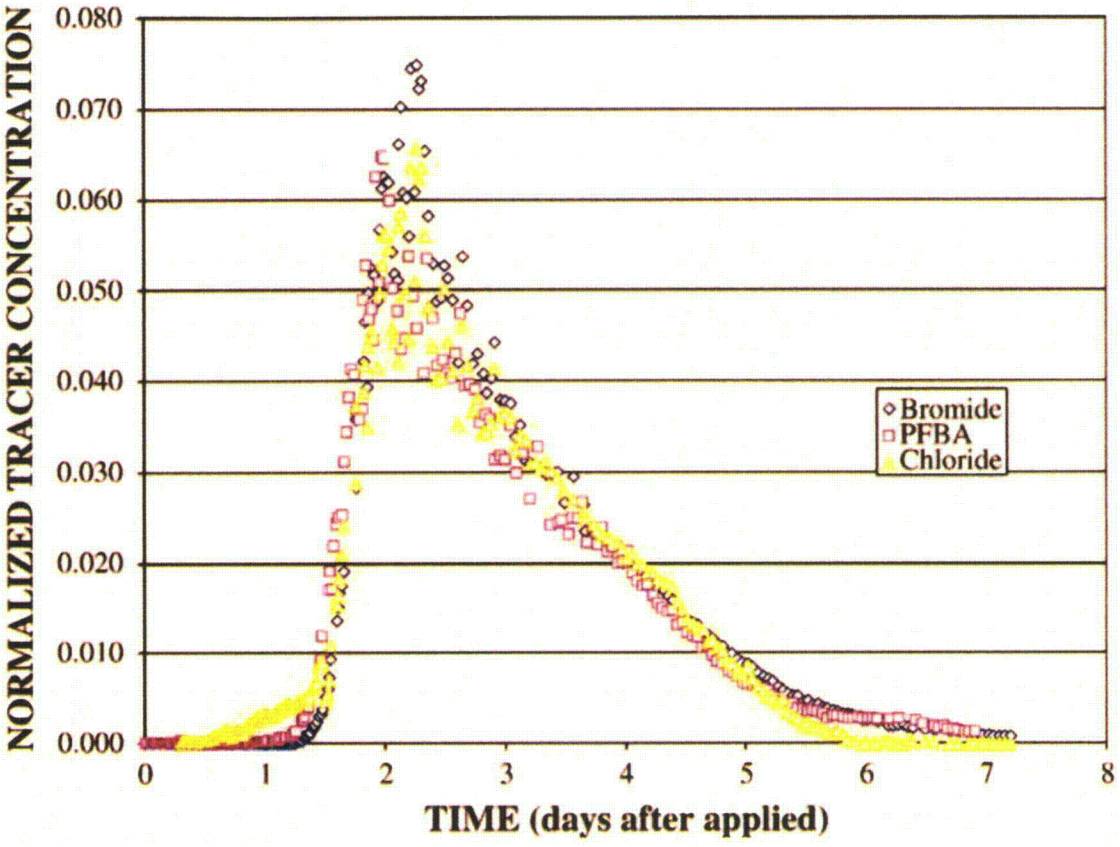

Figure 3-49. Observed tracer breakthrough curves for chloride, bromide and PFBA (after Gish and Kung, 2007. Permission to use this copyrighted material is granted by Geoderma).

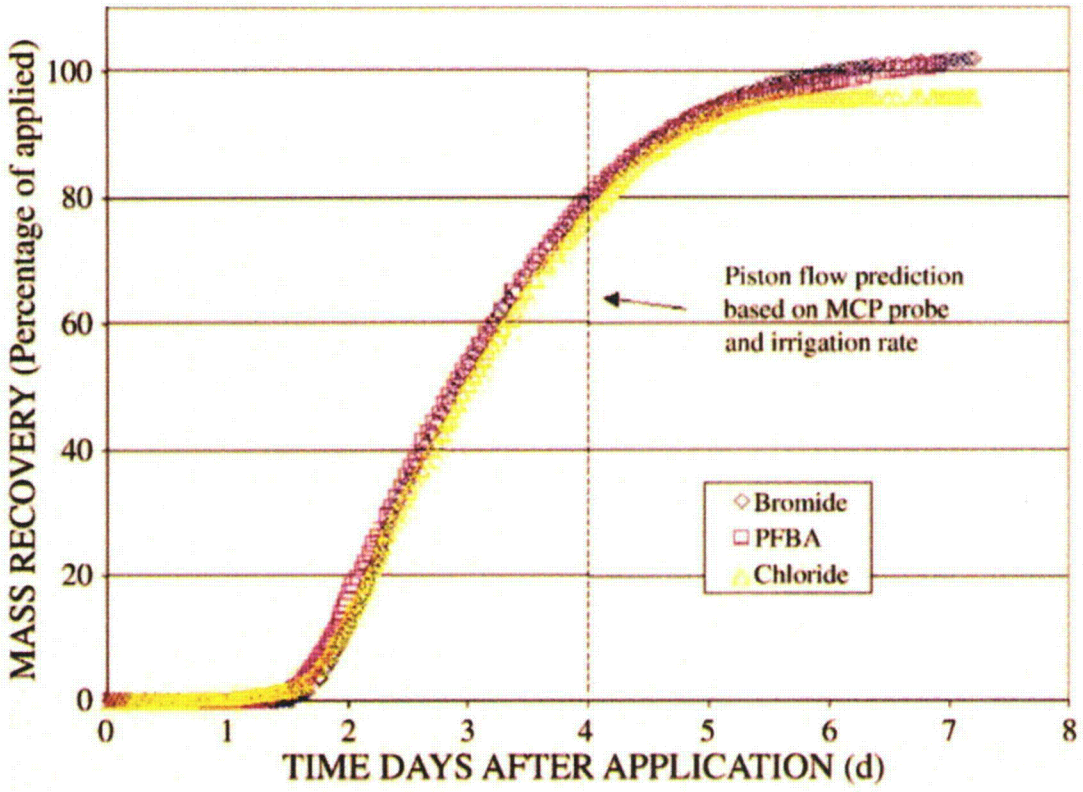

Figure 3-50. Tracer mass recovery (after Gish and Kung, 2007. Permission to use this copyrighted material is granted by Geoderma).

13x14 m study area. The sprinklers were connected to a water hose equipped with a DLJSJ50 water meter (Daniel L. Jerman Co., Hackensack, NJ) to measure the amount of applied water.

The observation wells at locations 1-12 were equipped with samplers to collect water from 3 different depths. The samplers consisted of a plastic 16-mm OD tubes containing 4 rubber packers installed into the wells. The packers separated three 30-cm long sections inside of the wells. A 2-mm ID plastic tubing connected the center of each section with the sampler outlet. Water samples were taken from each section with a 50-ml syringe. The sample volume typically ranged between 10 and 14 ml. The samplers were installed such that the samplings were taken at depths of 1.1 m at locations 1-4, and 1.05, 1.35 and 1.65 m at locations 5-12.

A total of 42 kg KCl was dissolved in two 2.1-ton tanks with 4050 L of tap water to provide a Cl^- concentration of 4940 ppm. The KCl solution was applied to the experimental site using the irrigation system. The application started at 10:30 am and ended at 5:05 pm on March 25, 2008. A total of 3861 liters was applied to the site within 6.6 hr. The irrigation system was reconnected to the tap water hose immediately after the application.

The irrigation was interrupted at 10:30 am on March 27 because of runoff at the site. Runoff losses were 39% of the irrigation water. The irrigation regime was adjusted to minimize runoff losses and to provide a nearly steady-state infiltration rate into the soil. Starting March 28, the site was irrigated twice a day, from 6 to 8 am and from 4 to 6 pm. Irrigation times were controlled by an irrigation timer and set such that well water could be sampled twice a day for Cl^-. Runoff amounts from the experimental site were recorded continuously. Irrigation was interrupted only after intensive rainfalls. The irrigation regime was corrected one more time on June 1 because of an increase in evapotranspiration that caused a decrease in the groundwater levels at locations 1-4. New times were set up for three irrigations each day: from 5 am to 7 am, from 1 pm to 3 pm, and from 9 pm to 11 pm. This schedule was followed until the end of experiment.

Water samples were taken from three depths at 12 locations one hour prior to the KCl application. Samples were taken twice a day within the first 40 days after application, and then once a day (at 5 pm) until the end of the experiment. Within 24 hours of their collection in the field, the samples were analyzed for Cl^- by ion chromatography as described in chapter 3.2.4.1. Irrigation and rainfall water was also periodically analyzed for Cl^-. Soil water contents and groundwater depths were monitored using MCPs and Cera-Divers at 12 locations as described in chapter 3.2.3.2. The study was terminated when the groundwater levels decreased below the water sampling depths at most locations.

Experimental results.

Cumulative irrigation, precipitation, evapotranspiration and runoff data are shown in Fig. 3-51. The daily irrigation rate was 9.5 cm d^{-1} during the first two days, 1.5 cm d^{-1} during the next 64 days, and 1.8 cm d^{-1} during the following 65 days. The first portions of runoff usually approached the flume 30-40 min after irrigation started. Runoff amounts were found to be in the range from 21 to 38% of the irrigation volumes. A total of 59 rainfall events were recorded during the 132-day experiment. The mean daily precipitation depth was 3.0 mm, which did not affect the soil water contents. Several events, however, did affect the water contents, the groundwater levels, as well as Cl^- concentrations in the wells. Rainfall events on April 22-23 (54.6 mm), on May 10-14 (159 mm), on June 5-6 (43.4 mm), and on July 25 (50.0 mm) exceeded the daily irrigation rates considerably, and as such affected the soil water regime as

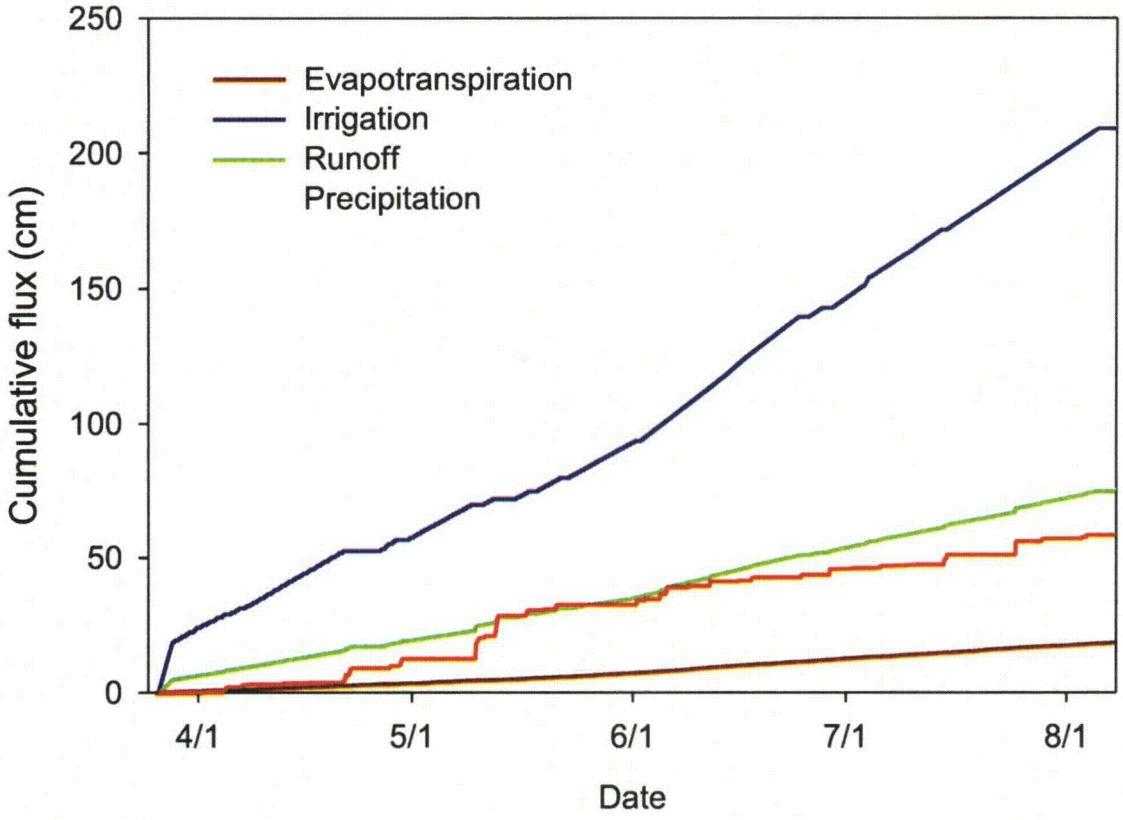

Figure 3-51. Cumulative water fluxes measured during the lateral flow experiment.

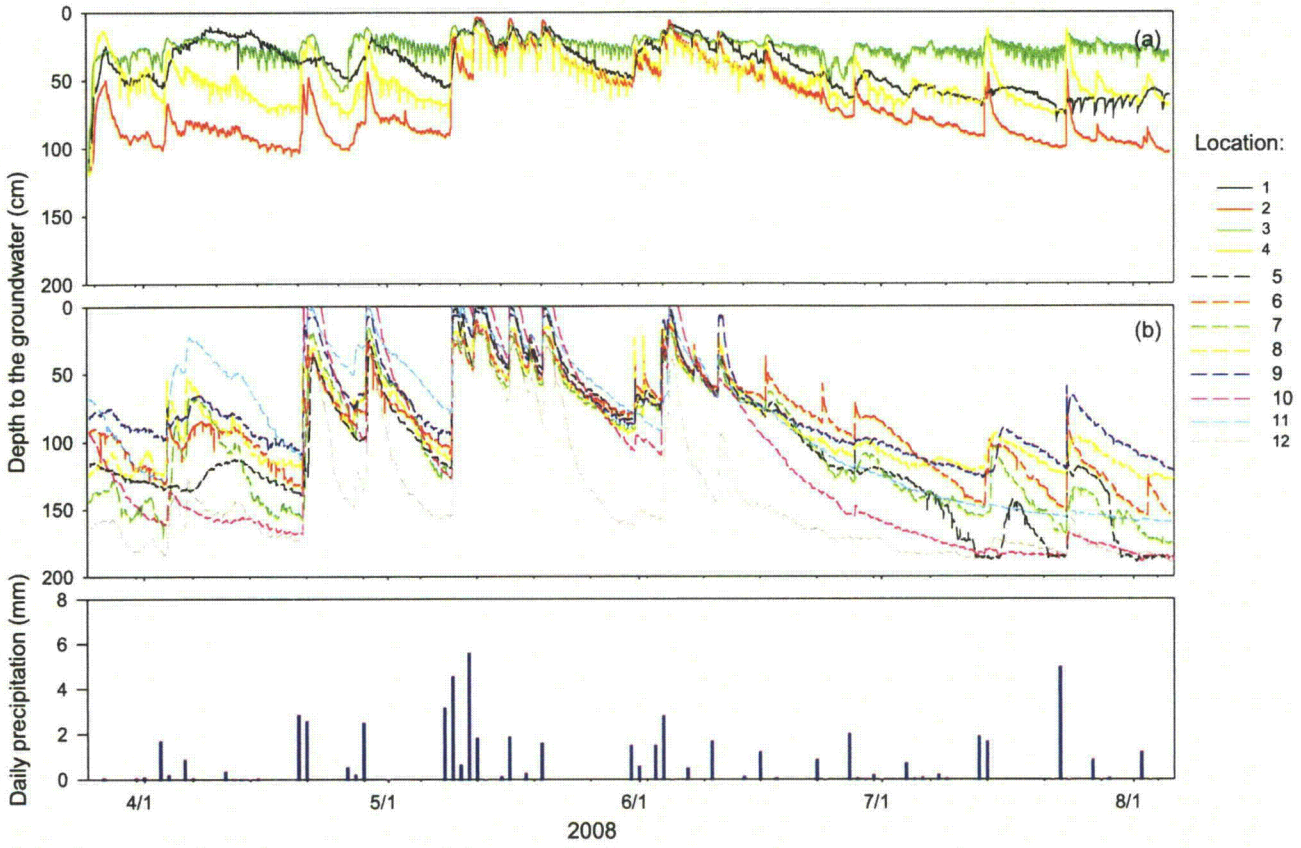

Figure 3-52. Groundwater depths measured during the lateral flow experiment.

will be shown below. The average ET values were 0.5, 0.8, 1.0 and 1.1 mm d^{-1} in April, May, June and July, respectively, which did not affect the soil water content dynamics.

Fig. 3-53 illustrates the water table dynamics. Groundwater levels remained relatively high at locations 1-4 during the lateral flow experiment (Fig 3-53a). Minimum groundwater depths (GWDs) were observed at location 3, and the maximum levels at location 2 where they exhibited severe oscillations. Severe oscillations were also observed at location 4, but the water table there was closer to the soil surface as compared to location 2. Peaks in the GWD at locations 2 and 4 generally corresponded to the more intensive rainfall events. The GWD at location 1 was less affected by rainfall as compared to locations 2 and 4. Observed differences in the water content and GWD dynamics at locations 1 through 4 implied different hydrological regimes in different parts of the irrigated site. The same is obviously true for locations 5 through 12. However, GWD differences between those locations remained between 5 cm after rainfalls and 119 cm after continuous soil drying. These differences were largest between the wells at adjacent locations 11 and 12. Considerable temporal variably in the GWD was also observed at locations 5 through 12. Average GWDs varied from 5 to 161 cm during the lateral flow experiment. Spatial and temporal variability in the GWD created unsteady subsurface flow from the irrigated plot toward locations 5-9 and locations 10-12.

A plot of the soil water dynamics during the experiment is shown in Fig 3-53. Soil water contents before the experiment were in the range from 0.148 to 0.403 cm^3 cm^{-3} and gradually decreased with depth. Three days after the experiment started, water content approached maximum values at practically all depths at locations 1 and 3, and below 25 cm depth at location 4, while remaining relatively constant until the end of the experiment. The water contents oscillated noticeably in the upper 20 cm at location 4 and at all depths at location 2.

Considerable water content oscillations were observed also at non-irrigated locations 5-12 in the upper 40-cm soil layer. Sharp increases and gradual decreases were observed in this soil layer immediately after the rainfall events (Fig. 3-53). Water contents at depths of 50 and 60 cm showed different behavior at these locations. Sharp increases were followed by sharp decreases at locations 7-9, whereas water contents at locations 11 and 12 did not change noticeably with time. Differences in the soil moisture dynamics were caused by different soil texture and changes in the groundwater depth at these locations. Soil texture at depths of 50-60 cm was sandy loam at locations 7-9, and loam at locations 11-12. Water contents in sandy loam soils near saturation tend to decrease faster with an increase in the absolute value of the pressure head, compared with loamy soils. Rapid changes in the GWD, as well as transitions from saturation to unsaturated conditions and vice-versa, likely caused abrupt water content changes at locations 7-9.

Differences in soil properties, hydraulic regimes and unsteady subsurface flow at the 12 locations affected Cl^- transport. Cl^- concentrations in groundwater prior to irrigation varied within the range from 6 to 24 ppm and did not differ significantly between the different depths and locations. Because of small spatial variability in the initial Cl^- concentration at the different locations, we did not expect any effect of the initial Cl^- distribution on the results of the lateral flow experiment. Cl^- concentrations in the irrigated water were 10.2±3.0 ppm, whereas rainfall Cl^- concentrations (0.6±0.6 ppm) were one order of magnitude less than the irrigation water and the groundwater concentrations. Hence, the effect of rainfall on the groundwater concentrations could be quite pronounced, especially after intensive rain events.

The Cl^- time series measured in 12 wells are shown in Fig. 3-54. We observed two distinctly different breakthrough curves at the irrigated site. A fast increase in Cl^- concentration was observed in wells 1 and 4 at the initial stage of the breakthrough curve soon after the tracer was

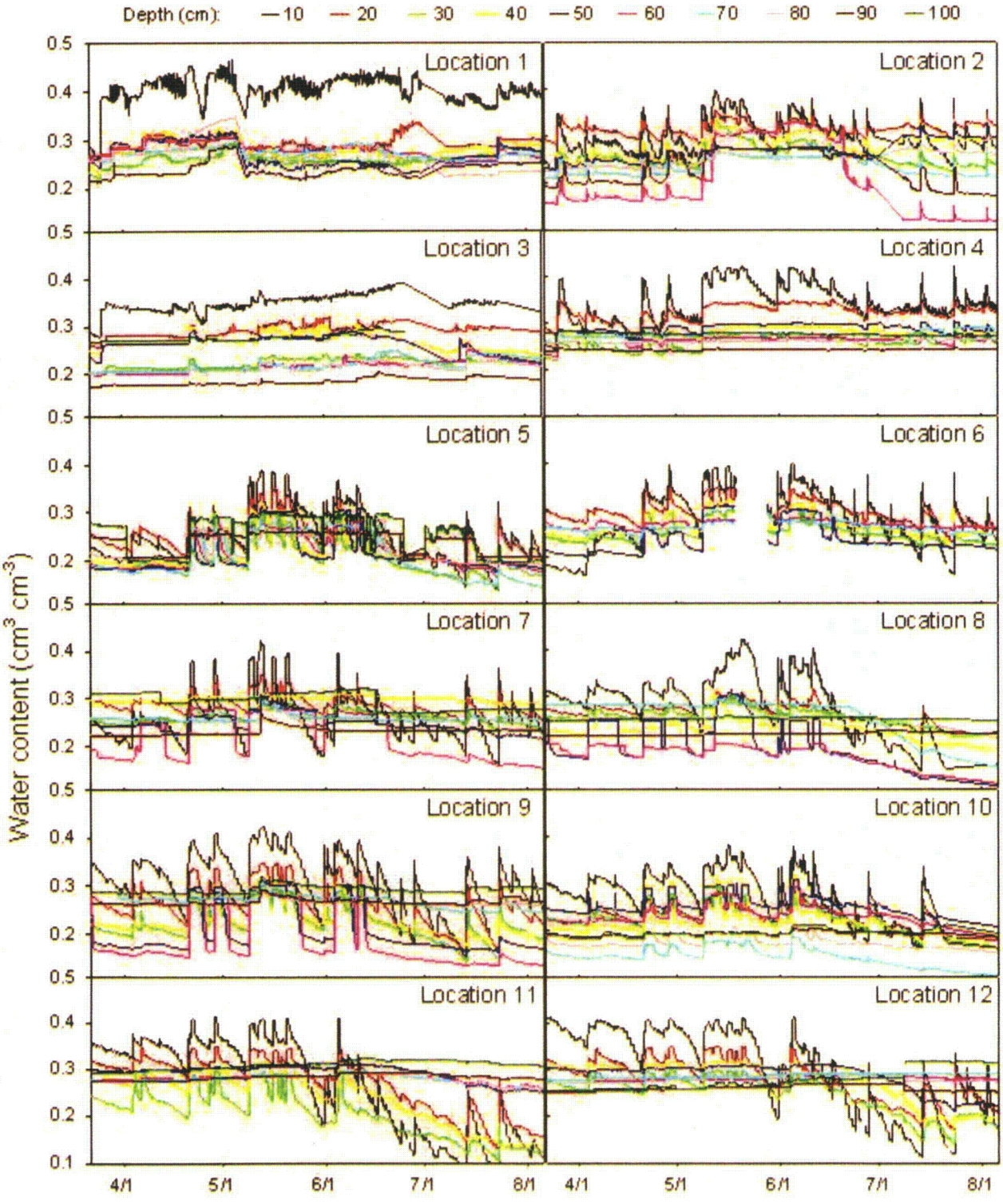

Figure 3-53. Soil water content measured at 12 locations during the lateral flow experiment.

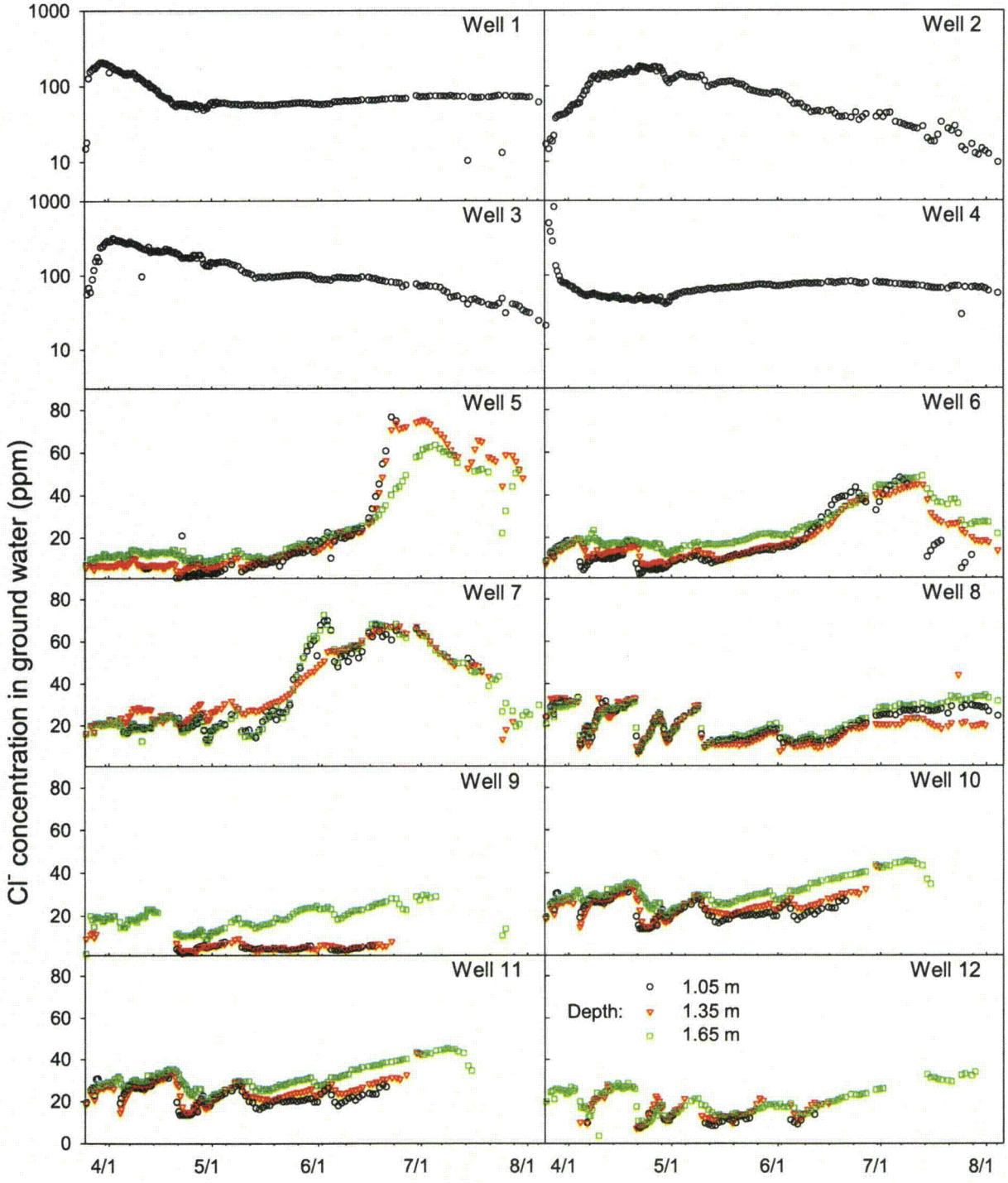

Figure 3-54. Chloride content in the groundwater measured in 12 wells during the lateral flow experiment.

applied. A gradual decrease and another increase in Cl^- concentration followed the initial stage. Contrary to wells 1 and 4, a relatively slow increase was followed by a gradual decrease in Cl^- in wells 2 and 3. These dramatic differences in the vertical transport rates of Cl^- at the irrigated site were likely caused by different transport conditions. The water contents were relatively constant and groundwater was closer to the soil surface at locations 1 and 3 compared to locations 2 and 4 where GWDs and the water content in the upper 0.50-m soil layer varied significantly during the later flow experiment. The water content and GWD data indicated that flow conditions were close to saturated at locations 1 and 3, but far from saturation in the topsoil layer at locations 2 and 4.

The tracer arrived at locations 5 through 9 at different times. It took approximately 60 days for the Cl^- to appear in noticeable amounts at three depths at location 7, and 80 days at locations 5 and 6. The distance between the irrigation site and locations 5 through 9 was 7 m, which means that the flow velocity should be within the range from 9 to 12 cm d^{-1}. The tracer arrived at locations 5 and 7 at higher concentrations than at location 6. Surprisingly, we did not observe Cl^- breakthrough at locations 8 and 9, which were also located 7 m downgradient from the irrigation site. Locations 5 through7 were probably closer to location 4, where vertical Cl^- transport was faster than transport at location 3.

An increase in the Cl^- concentration was observed at a depth of 1.65 m at locations 10,11 and 12 at the end of the experiment. However, the increases were not so pronounced as those at locations 5, 6 and 7 where the concentrations remained within the range observed at locations 8 and 9.

The Cl^- concentration time series differed at three depths at locations 5 through 12. Cl^- concentrations were generally higher at depth of 1.6 m, than at the 0.5-m and 0.8-m depths, except at locations 8 and 12 where the Cl^- concentrations did not change with depth, and location 7 where the highest Cl^- concentrations were observed at a depth of 1.35 cm. Noticeable differences in the Cl^- breakthrough curves were observed at three depths at locations 5, 6 and7. The peak concentrations at location 6 did not differ among three depths. At location 5, larger values were observed at depths of 1.05 and 1.35 m, whereas at location 7 the peak Cl^- concentrations at a depth of 1.35 m were smaller than those at depths of 1.05 and 1.65 m. Differences in the arrival times and the Cl^- concentration at three depths and 12 locations implies that the tracer was transported preferentially in hydraulically active soil zones.

An interesting phenomenon we observed was the synchronous dilution of groundwater at different depths during rainfall. This follows from the oscillations in the Cl^- concentration time series at locations 7, 8, 10, 11 and 12. These oscillations corresponded to the GWD oscillations caused by fast decreases in the GWD after intensive rainfalls (Fig. 3-54). Smaller Cl^- concentrations were measured when the GWDs were smaller. An increase in the GWD always caused an increase in the Cl^- concentration. The decrease in Cl^- concentration can be explained as being the result of ground water dilution by infiltrated precipitation (C_{Cl}=0.6 ppm), while an increase could be caused partly by evaporation. However, it remains to be explained why Cl^- changes occurred synchronously at three different depths without changes in the concentration with depth.